In situ bioconjugation of laser-generated gold nanoparticles for the rapid design of nanomarkers

Von der Naturwissenschaftlichen Fakultät

der Gottfried Wilhelm Leibniz Universität Hannover

zur Erlangung des Grades

Doktorin der Naturwissenschaften

Dr. rer. nat.

genehmigte Dissertation

von

Svea Petersen (Master Sciences)

geboren am 23.07.1981 in Lübeck

2010

Referent

Prof. Dr. T. Scheper

Institut für Technische Chemie

Leibniz Universität Hannover

Korreferent

Prof. Dr. B. Hitzmann

Institut für Technische Chemie

Leibniz Universität Hannover

Tag der Promotion

21. Juli 2010

Die Neigung der Menschen,

kleine Dinge für wichtig zu halten,

hat sehr viel Großes hervorgebracht.

Georg Christoph Lichtenberg

(1742-1799)

Meinen Eltern

Danksagung

Nach der Promotion werde ich das LZH verlassen. Annette und László, ich bin froh, dass Ihr die Arbeit fortsetzen werdet und wünsche Euch viel Erfolg. Haltet mich auf dem Laufenden!

Ich danke allen meinen Freunden, die auf unterschiedlichste Weise zum Gelingen dieser Arbeit beigetragen haben, nicht nur meinen langjährigen Freunden, sondern auch all denen, die hier in Hannover dazugekommen sind!

Danke, Sebastian, dass Du immer für mich da bist!

Zuletzt möchte ich mich bei meinen Eltern für ihre großartige Unterstützung bedanken, mit der sie mich durch mein Leben begleiten, und ihnen als Dankeschön diese Arbeit widmen.

Contents

Preface

In July 2007, I joined the Junior Research Group (JRG) "Nanoparticles" at the Laser Zentrum Hannover e.V. within the Excellence Cluster REBIRTH. This group, headed by Dr. Stephan Barcikowski, is part of the Nanomaterials group, which mainly deals with the fundamental characterization of metal and ceramic nanoparticle synthesis by laser ablation in liquids. With the foundation of the JRG, the research field was planned to be expanded by the development of bioactive nanocomposites for reconstructive therapy and the design of functionalized nanoparticles for biomedical applications. I became in charge of the second topic. As the objectives were not further detailed in the research proposal, we quickly started to meet with other REBIRTH researchers to find out about biomedical applications of functionalized nanoparticles. After some meetings, the message was rather clear. Innumerous ideas for the application of functional nanoparticles were mentioned, including the tracking of siRNA for a better understanding of cancer therapy or marking of specific cells for cell sorting issues. While gold seemed to be a promising core material of the nanomarker, the conjugation of nucleic acids and/or peptides was mainly requested as surface functionalization. Biocompatibility and efficient cellular uptake of the nanoparticles were defined as additional requirements.

However, there was not much concordance about the required design. Questions concerning the optimal sterical and electrochemical conformation of functionalized gold nanoparticles were raised. Also after an intensive literature research no consensus could be concluded, evidencing that the structure-function-relationship of functionalized nanoparticles is often not predictable. These findings motivated us to refine the laser-based nanoparticle preparation in order to provide a simple and rapid approach to functionalized nanoparticles, facilitating the required experimental search of an adequate design for each biological purpose.

In this context, the thesis at hand focuses on four main aspects:

- Toxicity and cellular uptake of laser-generated gold nanoparticles

- Bioconjugation of gold nanoparticles with nucleic acids during laser ablation

- Bioconjugation of gold nanoparticles with peptides during laser ablation

- Up-scale of the laser-based synthesis of nanoparticle bioconjugates

Each of these aspects is represented by one to three research papers. In total, seven reviewed papers are included, while four of them have been written by me. Further in preface, my contribution to each of the papers will be assigned.

But foremost, I would like to thank Dr. Stephan Barcikowski for his helpful guidance, the fruitful discussions, and his ideas, which have been valuable contributions to each of the papers presented. Furthermore I acknowledge all my coauthors, particularly Dr. Ulrike Taylor, Dr. Johanna Walter, and Dr. Csaba László Sajti.

Biocompatibility and cellular uptake of laser-generated gold nanoparticles is addressed in chapter 3. The first research paper included, *Co-transfection of plasmid DNA and laser-generated gold nanoparticles does not disturb the bioactivity of GFP-HMGB1 fusion protein*, was written by myself and studies possible effects of laser-generated gold nanoparticles on the transfection of plasmids, their read-out, and function of the expressed proteins. My experimental contribution was the generation, size fractioning, and characterization of gold nanoparticles. For the performance of the biological assays, I kindly acknowledge the collaboration with Jan Thies Soller and Dr. Hugo Murua Escobar, Kleintierklinik, Stiftung Tierärztliche Hochschule Hannover.

The second paper in this assembly, *Nonendosomal cellular uptake of ligand-free, positively charged gold nanoparticles,* addresses the cytotoxicity and the cellular uptake of laser-generated gold nanoparticles. This research article is one outcome of a very fruitful and intensive collaboration with Dr. Ulrike Taylor, who did most of the manuscript preparation, Dr. Sabine Klein, and Prof. Dr. Detlef Rath, Friedrich Loeffler Institut Mariensee. My contribution was the nanoparticle generation and support in result interpretation and study design.

Chapter 4 presents the main set of consecutive investigations on establishment and characterization of the bioconjugation of gold nanoparticles during laser ablation with nucleic acids. The first two papers in this chapter, *In situ bioconjugation - Single step approach to tailored nanoparticle- bioconjugates by ultrashort-pulsed laser ablation* and *Conjugation efficiency of the laser-based bioconjugation of gold nanoparticles with nucleic acids,* were both written by me. I performed all investigation and interpretation of data. I especially acknowledge the discussion with Dr. Stephan Barcikowski during manuscript preparation and his encouragement to submit to excellent journals. The third paper, *Laser ablation-based generation of bio-targeting gold nanoparticles conjugated with aptamers,* demonstrates the functionality of laser-generated aptamer-conjugated gold nanoparticles in an agglomeration-based and solid phase assay. This study was conducted in collaboration with the Institut für Technische Chemie, Leibniz Universität Hannover, particularly Dr. Johanna Walter, who conducted the manuscript

writing and Prof. Dr. Thomas Scheper, who I also acknowledge for taking the supervision of this doctoral thesis. All TEM and surface coverage analysis and the conjugation of the PSMA aptamer with the gold colloid were conducted by me.

The third aspect presented in chapter 5 comprehends the bioconjugation of gold nanoparticles with the cell penetrating peptide penetratin. I fully conducted interpretation of data and manuscript preparation of the paper *Penetratin-conjugated gold nanoparticles – Design of cell penetrating nanomarkers by femtosecond laser ablation*. I acknowledge Annette Barchanski for the experimental support in nanoparticle conjugate characterization during her internship and her master's thesis under my supervision and Dr. Ulrike Taylor and Dr. Sabine Klein for the cellular penetration assays.

The last of the four aspects is dedicated to the scale-up of the established laser-based bioconjugation (chapter 6). A miniaturized process chamber for the generation of nanoparticle bioconjugates in a liquid flow was constructed and its applicability was tested by Dr. Csaba László Sajti. I conducted the stationary experiments for comparison and acknowledge Dr. Csaba László Sajti for the preparation of the resulting research paper *In situ bioconjugation in stationary liquid and in liquid flow*. Prior to publication the idea was implemented in a patent application, *Verfahren und Vorrichtung zur Herstellung metallhaltiger organischer Verbindungen, PCT/EP2009/059116 (July 15th 2009)*.

Abstract

Due to their interesting optical properties, bioconjugated gold nanoparticles show the potential for applications as nanomarkers especially suitable for *in vivo* and long-term studies. Three major requirements on these functional nanomarkers include the high affinity towards a target molecule, an efficient cellular internalization, and biocompatibility, which are all affected by sterical (surface coverage, size) and electrochemical (surface charge) properties. However, since the structure-function-relationship is often not predictable, an experimental search of an adequate design for each biological purpose is required. To facilitate and expedite this experimental research, the method of *in situ* bioconjugation during laser ablation was established and further developed for the conjugation of gold nanoparticles with model biomolecules as single stranded oligonucleotides, aptamers, and the cell penetrating peptide penetratin. Additionally, the suitability of laser-generated gold nanoparticles for biological applications was explored with regard to cellular uptake, cell viability, or interaction with biomolecules.

No adverse effects on the biofunctionality of expression plasmids and on cell viability at nanoparticle concentrations required for the marking of cellular features were observed during co-incubation experiments. Moreover, a non-endosomal cellular internalization, which might be especially interesting for biomedical applications based on the interaction with compartments in the cytoplasm, was detected.

The *in situ* bioconjugation during laser ablation allowed for a simultaneous nanoparticle fabrication and their bioconjugation via the addition of functional molecules to the ablation medium prior the laser process. In a batch process, up to 20-30 µg of bioconjugates, being sufficient for one or two biological testings, could be generated in one minute preserving the bioactivity of the conjugated agent. Exemplarily, unlimited functionality of aptamer-conjugated nanoparticles could be proved in three independent analytical methods. A nanoparticle size quenching effect was evidenced during all conjugations in dependence of the biomolecule concentration in the ablation media, while the peptide conjugation additionally induced the formation of aggregates at higher concentrations. In comparison to conventional nanoparticle bioconjugation techniques as the ligand exchange method, five times higher maximal surface coverage values were determined, being especially interesting for the conjugation of precious biomolecules. While nanoparticle productivity in this batch process was limited by biomolecule degradation at higher pulse energies, a developed flow chamber reduced this limitation, opening the avenue towards high-throughput fabrication of nanoparticle bioconjugates. In conclusion, *in situ* bioconjugation makes the rapid generation of variable bioconjugates accessible, which can facilitate and simplify the screening of an adequate nanoparticle design**.**

Keywords: gold nanoparticle, bioconjugation, laser ablation in liquids

Zusammenfassung

Auf Grund ihrer interessanten optischen Eigenschaften sind biokonjugierte Goldnano-partikel vielversprechende Nanomarker für *In vivo*- und Langzeitstudien. Die drei wich-tigsten Anforderungen an die Nanomarker beinhalten eine starke Affinität zu einem Zielmolekül, eine effiziente zelluläre Internalisierung und Biokompatibilität, welche stark durch sowohl sterische (Belegungsgrad, Größe) als auch elektrochemische (Oberflä-chenladung) Eigenschaften der Nanopartikel beeinflusst sind. Da sich jedoch die Struk-tur-Funktions-Beziehung oft nicht vorhersagen lässt, erfordert jede spezielle biologi-sche Anwendung ein experimentelles Nanopartikeldesign-Screening. Zur Erleichterung und Beschleunigung dieses Screening-Prozesses wurde die Methode der *In situ* Bio-konjugation während des Laserstrahlabtragens etabliert und am Modell der Biokonju-gation von Goldnanopartikeln mit Oligonukleotiden, Aptameren und dem zellpenetrie-renden Peptid Penetratin weiterentwickelt. Darüber hinaus wurde die Eignung der la-sergenerierten Goldnanopartikel für biologische Anwendungen mit Hinblick auf die zel-luläre Aufnahme, die Zellvitalität und die Interaktion mit Biomolekülen untersucht.

Nanopartikel-Koinkubationen mit für biologische Anwendungen relevanten Konzentra-tionen wiesen keine negativen Effekte auf. Weiterhin wurde eine nicht endosomale Internalisierung beobachtet, welche Anwendungen, die auf einer Interaktion der Nano-marker mit Zellkompartimenten im Zytoplasma beruhen, erst ermöglicht.

Durch die Zugabe von funktionellen Molekülen in das Ablationsmedium vor dem Laser-Prozess ermöglichte die *In situ* Biokonjugation eine gleichzeitige Herstellung von Na-nopartikeln und deren Biokonjugation. Im Batch-Verfahren konnte innerhalb einer Mi-nute eine für ein bis zwei biologische Tests ausreichende Menge von 20-30 µg der Biokonjugate hergestellt werden. Eine uneingeschränkte Funktionalität der Biomoleküle wurde experimentell am Beispiel von Aptamer-Konjugaten nachgewiesen. Ein Quenching des Nanopartikelwachstums wurde während aller Konjugationen in Abhän-gigkeit von der Biomolekülkonzentration beobachtet. Im Vergleich zu konventionellen Methoden der Biokonjugation (Ligandenaustausch) konnten fünffach höhere Bele-gungsgrade ermittelt werden. Dies zeichnet die Methode besonders für die Konjugation von wertvollen Biomolekülen aus. Während die Nanopartikel-Produktivität im Batch-Verfahren durch die Degradation der Biomoleküle bei höheren Pulsenergien limitiert ist, konnte diese Einschränkung mittels Entwicklung einer Durchflusskammer reduziert werden. Damit wurde ein Schritt in Richtung Herstellung von großen Mengen an Bio-konjugaten geleistet.

Zusammenfassend bietet die Methode der *In situ* Biokonjugation einen schnellen Zu-gang zu variablen Biokonjugaten. So wird das Screening nach einem passenden Konjugatdesign beschleunigt und vereinfacht.

Schlagwörter: Goldnanopartikel, Biokonjugation, Laserstrahlabtragen in Flüssigkeiten

1.   Introduction and aims of the study

Nanoparticles (NPs) are generally defined as discrete particles between 1 and 100 nm in size [1]. They can be dispersed in water or organic solvents depending on the preparation conditions and capping agents surrounding the particles. The number of potential applications of these colloidal particles is growing rapidly because of their unique electronic, optical, magnetic, and catalytic properties compared with the corresponding bulk material and molecules. Especially their size comparable to biomolecule size let nanoparticles provide a particularly useful platform, demonstrating outstanding characteristics with potentially wide-ranging biomedical applications.

The emerging research field of nanomedicine combines material science, biology, and medicine. One major research field comprehends the conjugation of NPs with special recognition motives as contained in nucleic acids (NAs) and peptides. The resulting specific interaction with corresponding biomolecules (like antigen-antibody, hormone-receptor complexes, complementary nucleic acids, aptamer-target molecule) leads to a localized accumulation of the functionalized NPs. Depending on the NP material and further surface functionalization, one could envisage four major implementations: biosensing, bioimaging, localized therapy, and drug delivery.

Gold nanoparticles (AuNPs), functionalized with recognition motifs, represent a material with the potential of covering a very broad range of biomedical applications. Many of these application prospects of AuNPs rely on their fascinating interaction with light. For example, a gold colloid comprises an intensive red color (Figure 1.1 A). This tagging feature is often used in solid phase assays for the detection of various biomolecules, recognized by the functional gold nanoparticles (Figure 1.1 B). Additional to light absorbance AuNPs provoke a photostable intensive light scattering. In combination with an accumulation due to the selective recognition of tissue, cells, or single molecules, promising applications as diagnosis, cell sorting, and tracking of biological functions are conceivable (Figure 1.1 C). A further application as therapeutic agent is based on the heat release into the environment of AuNPs upon light absorption. A local photothermal ablation of tissue, especially interesting for cancer therapy, might thus be enabled (Figure 1.1 D).
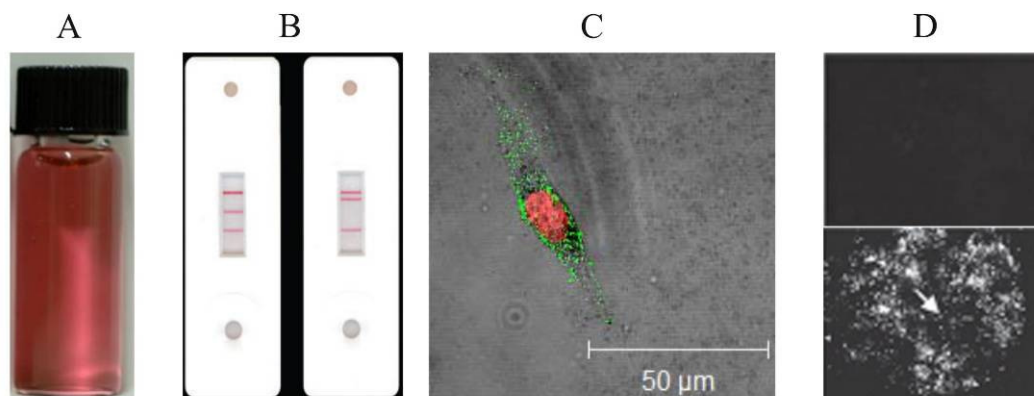
Figure 1.1.: (A) Gold colloid. (B) AuNP-based solid phase assay for the serial detection of up to six amplified nucleic acid targets; courtesy of BBInternational, Cardiff, UK. (C) Scattering-based detection of intracellular AuNPs [2]. (D) Photothermal ablation mediated by AuNPs. Cells irradiated in the absence of AuNPs maintain intact, as indicated by lack of intracellular fluorescein dextran uptake (top). Cells irradiated with AuNPs possess well-defined circular zones of cell membrane disruption (bottom) [3].

However, in order to become appropriate for biomedical applications, biocompatibility (e.g., for diagnosis) and efficient cellular internalization (e.g., for tracking and marking of intracellular targets) are two further requirements on functionalized AuNPs. It is nowadays consensus, that biocompatibility, cellular internalization, and also binding affinity of the NPs are affected by their sterical (e.g., surface coverage) and electrochemical (e.g., surface charge) properties. However, the structure-function-relationship is often not predictable. Furthermore, some properties might have opposite effects on each of the required functions. One could for example imagine, that a positive net charge on the NPs surface enhances cellular uptake on one hand, while it might reduce the affinity towards a special recognition motif on the other hand. Synthesis and testing of various different bioconjugates is thus required in order to find an adequate design for each biological purpose.

Conventionally, the generation of AuNPs is well established by chemical synthesis methods in the presence of stabilizing agents. The bioconjugation with required recognition motifs is commonly enabled in a successive substitution of the stabilizing agent by the functional molecule. This ligand exchange method is not trivial, as hindrance of incoming and outgoing agents makes it arduous to predict the extent of place exchange. Low functionalization degrees might be the consequence, which is not tolerable especially for precious biomolecules. Furthermore, the bioconjugation of AuNPs with more than one functional molecule remains a severe challenge.

Laser ablation in liquids (LAL) has become a reliable alternative to traditional chemical reduction methods for obtaining gold nanoparticles for researcg purposes to date. This

approach consists in the ablation of a gold foil in liquid media by intense laser radiation, leading to an ejection of its constituent and the formation of an AuNP colloid. Thereby, it allows the generation of stable AuNPs in water and organic liquids without stabilizing additives, providing great opportunities for a controlled particle *in situ* functionalization via the simple addition of functional molecules to the ablation medium. Moreover, LAL guarantees sustainability of the method due to negligible purification steps. Despite these excellent properties with regard to biological applications, there are rare reports on the application of laser-generated AuNPs in biology or medicine, while the *in situ* bioconjugation with NAs or peptides during LAL has not been investigated so far.

In this context, the thesis at hand explores the applicability and the further development of LAL for the rapid design of single stranded oligonucleotide (ssO) or peptide-conjugated AuNPs. Additionally, as this deals with AuNPs with novel surface chemistry, not reproducible by any other method, their biocompatibility and cellular internalization is investigated.

The thesis is organized as follows:

The first part of chapter 2 reviews literature on biomedically relevant properties of AuNPs and their dependence on structural features. A second and third part of this chapter deals with the state of the art of conventional AuNP synthesis and their bioconjugation, while the final part introduces LAL as an alternative method likewise for AuNP generation.

Chapter 3 to chapter 6 cover the presentation of the experimental results of this thesis. These chapters are always supported by own research articles, prepared during the study. Chapter 3 focuses on the biocompatibility and cellular uptake of laser-generated AuNPs, while chapter 4 presents the main set of investigations on the set-up and characterization of the bioconjugation of AuNPs during laser ablation with NAs. The expansion of this *in situ* conjugation method to the coupling of peptides is discussed using the example of the cell penetrating peptide penetratin in chapter 5. The 6th chapter is dedicated to the scale-up of the established laser-based bioconjugation. A summary and outlook is provided in chapter 7.

2. State of the art

2.1. Gold nanoparticles in biomedicine

Today's biomedical importance of AuNPs is mainly based on their outstanding optical properties. However, advancing the use of AuNPs in e.g., cellular imaging can only take place with a fundamental understanding of the cellular mechanisms involved in their uptake. For *in vivo* application the biocompatibility of the gold nanoparticle is a further important factor. Further in text, these three aspects are considered, while special attention is given to their structure dependency.

2.1.1. Optical properties

The use of gold in decorative artworks as a red colorant is as ancient as the Roman Lycurgus cup from the 4th century. The attribution of the intensive red color to colloidal gold has first been recognized by Faraday in 1857 [4], while the origins of the phenomenon have been intensively studied and explained by the Mie theory half a century later [5]. Mie discovered that for a spherical NP much smaller than the wavelength of light, an electromagnetic field induces a resonant, coherent oscillation of the metal free electrons across the NP (Figure 2.1 A). The oscillation, to date known as surface plasmon resonance (SPR), results in a strong enhancement of light absorption and scattering at a certain frequency. This frequency and the cross section of the SPR depend on metal composition, NP size and shape, dielectric properties of the surrounding medium, and the presence of inter-particle interactions [6]. The influence of these variables on the optical properties can be estimated by the Mie theory (Eqn. 2.1). Resolving this equation for AuNPs in water, one finds that the SPR is situated around 520 nm, evidencing a slight bathochromic shift with increasing particle diameter.

$$C_{ext} = \frac{24\pi^2 R^3 \epsilon_m^{3/2}}{\lambda} \frac{\epsilon''}{(\epsilon' + 2\epsilon_m)^2 + \epsilon''^2}$$

(Eqn. 2.1.)

C_{ext} : extinction cross section, R: particle radius (equation valid if 2R<<λ), ϵ_m: dielectric constant of the surrounding medium, and ε=ε'(λ)+iε''(λ): wavelength-dependent, complex dielectric function of the nanoparticle material

Additionally, the relative contribution of SPR scattering to the total extinction of small AuNPs is close to zero, while it increases for bigger AuNPs. Hence, 40-nanometer-sized nanoparticles essentially show SPR-enhanced absorption (Figure 2.1 B) with an estimated extinction coefficient of 7.7×10^9 M^{-1}cm^{-1} at 530 nm [7], being about five orders of magnitude higher than that of conventional fluorophore labels (e.g., malachite green: 1.5×10^5 M^{-1}cm^{-1} at 617 nm [8]). According to that, smaller AuNPs are interesting for the colorimetric bioanalytical sensing with extraordinary high sensitivity. By contrast, the extinction caused by 80-nanometer-sized AuNPs, is about 50 % due to scattering and 50 % due to absorption (Figure 2.1 C). These particles are therefore more promising for the use as contrast agents in cellular imaging, overcoming the problem of subtle differences between marked and unmarked cells. Due to the absence of photobleaching under light irradiation, long-term tracking of subcellular functions is also enabled by AuNPs. However, *in vitro* success of imaging can be extended to skin and surface-type cancers, while for deeper tissue near infrared excitation with penetration depth up to a few centimeters is required. One route to *in vitro* imaging can be achieved by the use of nanorods, which in addition to an SPR band around 520 nm, show a band at longer wavelength, arising from the plasmon oscillation of electrons along the longitudinal axis of the nanorods [9].
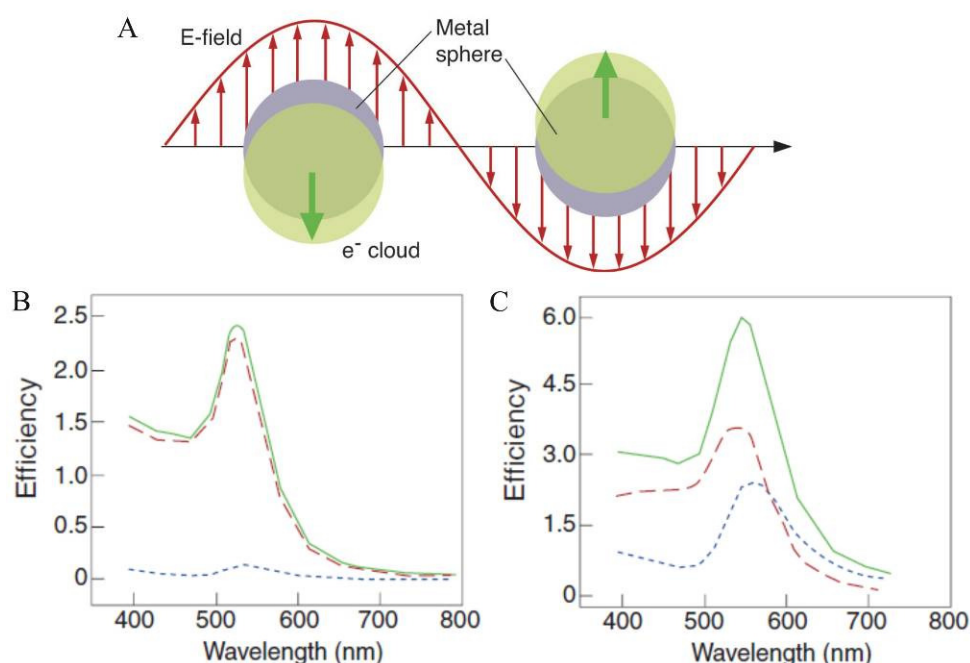
Figure 2.1.: (A) Schematic representation of the interaction of a metal nanosphere with light [10]. Mie theory absorption (red dashed curve), scattering (blue dotted curve) and extinction (green solid curve) spectra of Au nanospheres of diameter (B) 40 nm and (C) 80 nm [7].

Another interesting property of AuNPs for sensing is the SPR's sensitivity to the local refractive index/dielectric constant of the environment surrounding the NP surface. Thus adsorption and binding events as for example hybridization reactions at the surface might be monitored [11]. But also the self assembly and aggregation of gold nanoparticles results in a shift of SPR, which is used in the nowadays developed assays, based on the analyte-induced agglomeration of AuNPs [12].

2.1.2. Cellular internalization

Most of cellular internalization studies performed with AuNPs so far, revealed an active endocytic or phagocytic mechanism that is temperature and energy-dependent. An influence of the AuNP size on internalization has been observed by two independent groups and studies [13, 14, 15]. In a diameter range from 10 to 100 nm, 40 to 50-nanometer-sized chemically derived AuNPs seemed to be internalized most efficiently by endocytosis, while the time for internalization often occupies up to 48 h.

With regard to surface charge, positively charged NPs were generally internalized with a higher efficiency compared to negatively charged NPs. This is often dedicated to the higher affinity of positively charged species to phospholipids in the cell membrane. Endosomal escape was preferentially reported for smaller positively charged NPs [16], which might be important if further interaction of the NP with subcellular compartments is required.

Surface modification is a further means reported to provide AuNPs with the ability to specifically bypass intracellular obstacles (e.g., endosomes). Besides viral vectors [17] and dendrimers [18], which might provoke adverse effects on cells, peptides containing so-called protein transduction domains are more and more used as carriers to efficiently translocate across cell membranes [19, 20]. The internalization mechanism of these amphipathic peptide sequences is still controversially discussed; one even assumes that some peptides cross the cellular membrane by more than one mechanism in dependence on the cargo molecule and the peptide concentration [21]. Among these cell penetrating peptides (CPP), the most popular is the Tat peptide, derived from the human immunodeficiency virus type-1 (HIV-1) Tat (transactivator of transcription), which has already been described to efficiently deliver AuNPs, conjugated via BSA [22] or tiopronin [23], into cells and even the nucleus.
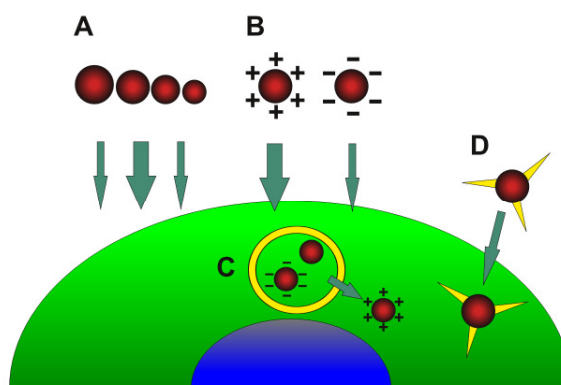
Figure 2.2.: Schematical representation of the (A) NP size and (B) surface charge dependent nanoparticle uptake and (C) endosomal escape. (D) Endosome bypassing can be additionally achieved by surface modification [16].

Figure 2.2 schematically summarizes the key variables (size, surface charge, and functionalization) appearing to be most critical for the efficiency and mechanism of NP uptake into cells. These should hence be systematically studied and adapted for each biological application in order to avoid the need of invasive methods (e.g., microinjection) or use of transfection agents affecting membrane functionality for efficient cellular internalization.

2.1.3. Biocompatibility

Bulk gold is known as a bioinert and hence biocompatible metal due to the absence of interactions between orbitals of adsorbates like hydrogen and oxygen and occupied d-orbitals of the gold [24]. However, materials non toxic at macroscale are reported to become harmful to cells at nanoscale [25], and as AuNPs for biological applications are intentionally engineered to interact with cells, it is important to ensure that these enhancements are not causing any adverse effects.

In recent literature, AuNPs are variously described as nontoxic or toxic. Nevertheless in comparison to other nanoscale material as for example quantum dots and carbon nanotubes, indications for significant toxicity at low concentrations are rather rare [26, 27]. However, the issue with apparently conflicting data regarding toxicity of AuNPs can be resolved by focusing on the various factors, which might influence the cytotoxic effect of the colloid. First of all, there is no accepted reference NP system available; hence every toxicity study employed differently generated AuNPs with varying size and surface modification. A further aspect is that each cell line acts differently under exposition to NPs and last but not least the used biological testing also has a significant influence

on obtained results. A norm, similar to the ISO 10993-1 for the biological evaluation of medical devices, would hence be required for reliable biocompatibility testing of NPs.

However, some factors possibly leading to an enhancement of cytotoxicity have already been determined to date. Non-surprisingly, a higher degree of cellular internalization of AuNPs seems to go along with a decrease in cell viability. As cellular uptake efficiency is mainly dictated by surface modification and nanoparticle size (chapter 2.1.2), these properties are suspected to affect nanoparticle toxicity as well.

In this context, Thomas *et al.* discovered a decrease of cell viability to 70 % after 6 hours of dodecylpolyethylenimine-(PEI-)conjugated AuNP exposure [28]. These PEI-modified AuNPs could transfect monkey kidney cells six times better than PEI alone. Studies by Tkachenko *et al.* observed the same tendency for peptide-BSA gold complexes [22]. With higher uptake in the cytoplasm and the nuclei, a higher level of cytotoxicity was determined. These findings were stressed by Goodman *et al.*, who showed that cationic (ammonium-functionalized) AuNPs, showing high electrostatic attraction to plasma membranes and therefore higher internalization potentials, were clearly more cytotoxic than anionic (carboxylate-functionalized) AuNPs [29].

Concerning the size-dependent cytotoxicity of AuNPs, Jiang *et al.* reported a direct correlation with cellular uptake efficiency in the range of 2 to 100 nm [13]. Accordingly, they stated a high degree of cytotoxicity for medium-sized AuNPs (40-50 nm as denoted in chapter 2.1.2). Pan *et al.* studied the size-dependent cytotoxicity for lower particle diameters down to 0.8 nm [30]. Interestingly, they found that triphenylphosphine-monosulfonate-capped Au_{55} clusters of 1.4 nm diameter are much more cytotoxic than 15-nanometer-sized AuNPs of similar chemical composition. They assumed that this effect is associated with oxidative stress and mitochondrial damage [31].

Although most reported biological effects of AuNPs seem to involve interactions with cellular components such as the plasma membrane, these results show that nanoparticles might also provoke sublethal effects by inducing oxidative stress, lipid peroxidation, inflammation, and up and downregulation of genes. Pernodet *et al.* for example observed morphological changes of cells due to AuNP exposition [32], while a downregulation of a number of DNA repair genes has been reported without any indices of loss in cell viability by Singh *et al.* [33].

Besides the biocompatibility of AuNPs themselves, the purity of the colloid should be one important concern, as the commonly used gold precursor ($HAuCl_4$) was found to be over 90 % toxic after 3 days of exposure [34]. This either requires good washing procedures applied nowadays or synthesis methods omitting the use of a toxic precursor.

2.2.   Chemical preparation of gold nanoparticles

NP synthesis methods are typically grouped into two categories: "top-down" and "bottom-up". The first involves division of a massive solid into smaller portions. This approach may involve milling, chemical methods, and volatilization of a solid followed by condensation of the volatilized components as for example NP generation by LAL. The mechanism and the application of this laser-based method for the synthesis of AuNPs are basically discussed in chapter 2.4. The "bottom-up" approach, often referred to as chemical reduction methods (CRM), is far more popular in the synthesis of metal and metal oxide NPs to date. The proposed mechanism involves stepwise formation of nanoclusters based on nucleation, growth and agglomeration of atoms or molecular entities in solution [35]. Generally, metal salts are reduced to zerovalent metal atoms, forming irreversible "seed" nuclei due to collisions of metal ions, metal atoms, or clusters. The diameter can be well below 1 nm depending on the strength of the metal-metal bonds and the difference between the redox potentials of the metal salt and the reducing agent applied (Figure 2.3). In order to control subsequent agglomeration of nuclei, protective agents are added to the reaction solution. Common protective agents are either charged, providing the NPs with an electrical double layer, or sterically bulky, shielding the metallic surfaces from each other. These two basic modes of stabilization are described by the termini electrostatic and steric stabilization. Several CRMs were reported and reviewed for the preparation of AuNPs throughout the 20th century and particularly in the past decade [36]. The following section focuses on main breakthroughs in the chemical preparation of AuNPs.
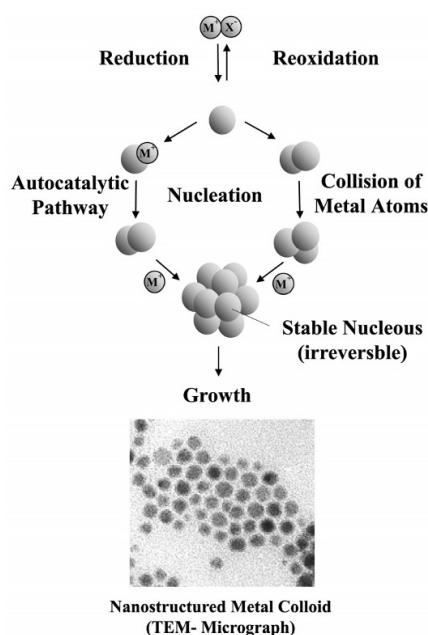
Figure 2.3.: Formation of metal colloids by CRM [37].

2.2.1. Citrate reduction

The simplest and by far the most commonly used CRM for AuNP preparation is the aqueous reduction of gold salts (mainly tetrachloroauric acid $HAuCl_4$) by sodium citrate at reflux, introduced by Turkevitch *et al*. in 1951 [38]. The following mechanism of particle formation and growth is proposed: Au^{3+} is reduced in solution by citrate to Au^+, which forms multimolecular complexes with dicarboxy acetone, as oxidation product of citrate (Figure 2.4). The complexes subsequently disproportionate, and gold atoms are formed. These atoms adsorb Au^+ and, by complexation with dicarboxy acetone, form aggregates.
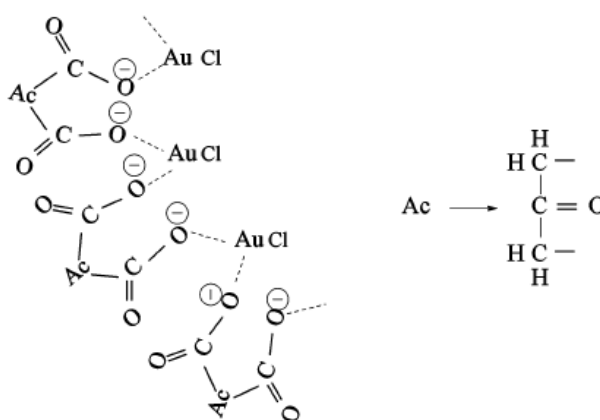
Figure 2.4.: Illustration of complex of aurous species and dicarboxy acetone [39].

Citrate simultaneously occupies the role of the reducing agent and provides the NPs with a negative charge and thus an electrostatic stabilization. Generally, this method leads to AuNPs of around 20 nm, but in an early effort, reported in 1973 by Frens, AuNPs of predetermined size (16 to 147 nm) were obtained via the variation of the citrate-to-gold ratio [40]. However, citrate is rather loosely bound to the gold surface, reducing long-term stability of such gold colloids. For storage these colloids need to be hermetically sealed in pre-scored glass ampoules in order to avoid oxidation [41]. Moreover, commercially available citrate-stabilized gold colloids sometimes contain rather toxic preservatives as sodium azide, rendering biomedical applications of these colloids impossible [42].

2.2.2. Gold cluster

The first breakthrough towards stable nanoclusters with narrow size dispersity was heralded in 1981 by the foundation of "Schmid's cluster" [Au$_{55}$(PPh$_3$)$_{12}$Cl$_6$] [43]. This metal cluster, obtained by the reduction of the phosphine gold halide (C$_6$H$_5$)$_3$PAuCl with B$_2$H$_6$ in benzol, was the first in which the number of metal atoms significantly exceeded the number of ligands. This CRM results in a very well defined arrangement of 55 metal atoms and 12 monodentate ligands with an average size of 1.4 nm ± 0.4 nm (Figure 2.5).
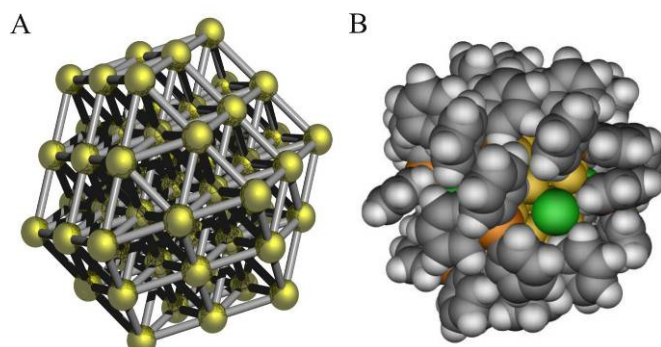
Figure 2.5.: (A) Metal core and (B) computer model of "Schmid's cluster" [Au$_{55}$(PPh$_3$)$_{12}$Cl$_6$] (Color legend: yellow: gold atoms, grey: triphenylphosphane, and green: chlorine atoms) [44].

2.2.3. Two phase synthesis and stabilization by thiol ligands

The so-called Brust-Schiffrin method has had a considerable impact directly after its publication in 1994, because it allows the facile synthesis of thermally and air-stable AuNPs of reduced dispersity and size ranging between 1.5 and 5.2 nm in diameter [45]. It even allowed the repeated isolation and re-dissolution of AuNPs in organic solvents without irreversible aggregation or decomposition. The method behind is inspired by Faraday's two phase system [4] and uses thiol (SH) ligands that strongly bind to gold due to the soft Lewis character of both gold and sulfur. Briefly, aqueous AuCl$_4^-$ is transferred to toluene using tetraoctylammoniumbromide as phase transfer reagent (Eqn. 2.2) and reduced by NaBH$_4$ in the presence of dodecanethiol (Eqn. 2.3).

$$AuCl_{4(aq)}^- + N(C_8H_{17})_4^+(C_6H_5Me) \rightarrow N(C_8H_{17})_4^+AuCl_4^-(C_6H_5Me)$$

(Eqn. 2.2.)

$$mAuCl_4^-(C_6H_5Me) + nC_{12}H_{25}SH(C_6H_5Me) + 3me^- \xrightarrow{NaBH_4} 4mCl_{(aq)}^- + (Au_m)(C_{12}H_{25}SH)_n(C_6H_5Me)$$

(Eqn. 2.3.)
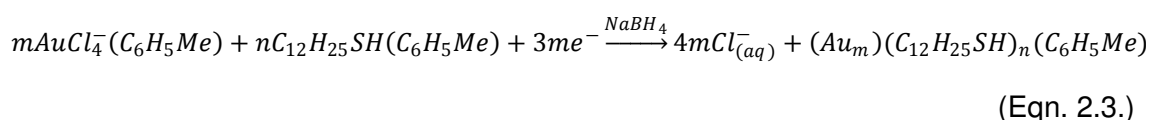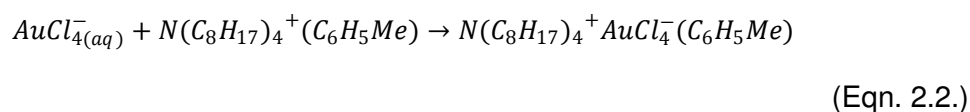
One limitation of this CRM is the indispensable purification of the colloid by a Soxhlet extraction in order to minor tetraoctylammonium impurities [46].
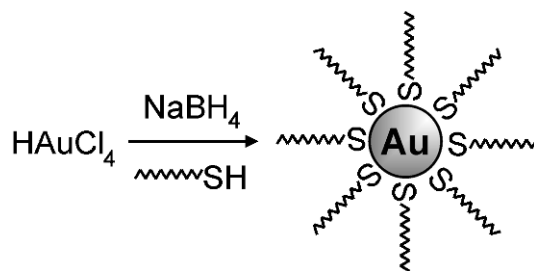
Figure 2.6.: The Brust-Schiffrin method yields the formation of RSH-stabilized AuNP by reduction of Au^{3+} [47].

But it is advantageous that resulting AuNPs are sterically stabilized with alkanethiols (RSH) in a well defined and ordered manner (Figure 2.6), referring to the self-assembled monolayers (SAM) of RSH on planar gold surfaces, discovered by Nuzzo and Allara in 1983 [48]. Two distinct adsorption kinetics are described to date [49]. The first is governed by the anchoring group (SH, disulfide etc.) and results in a monolayer, reaching a thickness of about 80-90 % of its maximum after a few minutes. The second step, where spacers (alkyl, ethyleneglycols etc.) get out of the disordered state, can last up to several hours and is mostly determined by the different components of chain-chain interaction (van der Waals, dipole-dipole, electrostatic). The reaction mechanism is formally considered as an oxidative addition of SH to the gold surface, followed by a combination of formed hydrogen atoms to yield H_2 molecules (Eqn. 2.4).

$$RSH + Au_n^0 \rightarrow RS^- Au^+ \cdot Au_{n-1}^0 + 1/2\, H_2$$
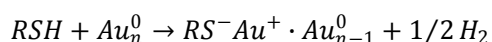
(Eqn. 2.4.)

It is nowadays well known that certain factors including head-group functionality, chain length and terminal group type control the structure of SAMs on both planar and particle surfaces [49]. However, the packaging on NP surfaces is additionally influenced by the particle diameter and surface curvature, thus less ordered SAMs with higher molecular packing are observed on smaller NPs [50].

2.3.   Bioconjugation of chemically derived gold nanoparticles

The immobilization of biomolecules (proteins, enzymes, and NAs) on polymers and anorganic carriers for biosensing is well established by various methods, including physisorption, electrostatical interaction, specific recognition, and covalent coupling. In order to open the avenue to the field of functionalized NPs for diagnostic and therapeutic applications, some of these methods are recently applied for the coupling of NPs and biomolecules. The following section introduces, but also identifies limitations of the electrostatic adsorption (Figure 2.7 A) and the thiol-mediated ligand exchange reaction (Figure 2.7 B-D) for the bioconjugation of chemically derived AuNPs. Main focus is drawn to the bioconjugation with NAs or protein structures, as two major classes of biomolecules with main relevance for targeting of specific molecules and cellular structures.
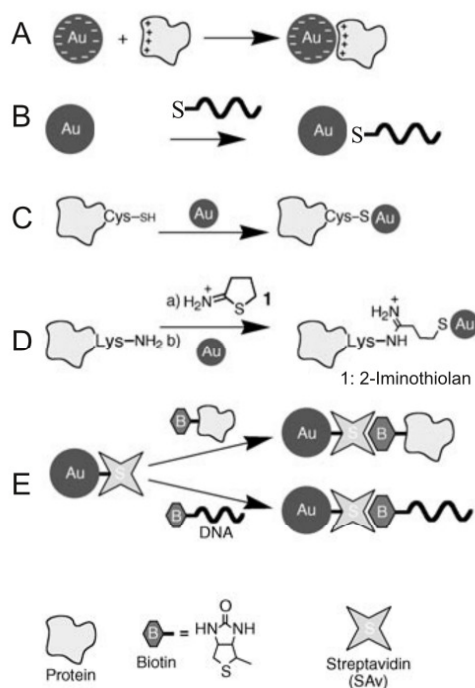
Figure 2.7.: Common bioconjugation techniques for chemically derived AuNPs [51]. (A) Electrostatic interaction of proteins and negatively charged AuNPs and thiol-mediated ligand exchange for the bioconjugation of (B) thiolated ssO, (C) cystein-rich proteins, and (D) proteins with incorporated thiol groups. (E) Bioaffinity interaction via streptavidine-biotin-complexes.

2.3.1. Electrostatic adsorption

The electrostatic adsorption of biomolecules on AuNPs presents a simple modification and is mostly applied to the coupling of big proteins [51]. One example is the adsorption of immunoglobulines to negatively charged AuNPs obtained by citrate reduction [52]. The reaction is carried out at a pH slightly above the isoelectric point of the citrate ligand to ensure electrostatic interaction with the positively charged amine residues of the aminoacids. The electrostatic adsorption has been furthermore applied for the formation of multilayers. Positively charged proteins, adsorbed to citrate-stabilized AuNPs, might act as platform for further adsorption of charged polyelectrolytes. Thus, functional layers of high density can be grown up to several 100 nm [53]. However, this conjugation method might provoke problems of instability and inactivation of the protein due to the unoriented immobilization. This inactivation might be even more fatal for ssO, which have been shown to form a DNA shell on AuNPs via citrate substitution [54].

2.3.2. Thiol-mediated ligand exchange

The formation of SAMs by RSH ligands, introduced in chapter 2.2.3 as a form of sterical NP stabilization, can be also employed for AuNP bioconjugation. However, the addition of thiolated biomolecules in the synthesis environment before the reduction of the metal salts, which is supposed to be the most intuitive way, is less common, due to compatibility problems between functional molecules and reaction conditions but also to the sensitivity of CRMs to the properties of stabilizers, e.g., solubility [55]. More usual to date is a subsequent ligand exchange reaction, which involves the substitution of the stabilizing agent (commonly RSH or citrate) with the functional molecule to be introduced (Figure 2.8). But this ligand exchange is not trivial, as hindrance of incoming and outgoing agents makes it arduous to predict the extent of place exchange [55]. No entire replacement is achievable and certain reaction precautions as heating and buffering to obtain satisfactory yields and surface coverages are often required. AuNPs, derived by citrate reduction, generally allow an easier replacement than thiol-stabilized NPs and are more appropriate for biological purpose due to their solubility in aqueous solutions. However, aggregation might occur and compared to bare metal surfaces, a lower degree of functionalization has been observed [56, 57].
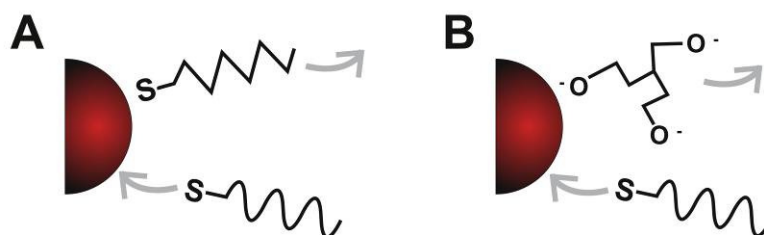
Figure 2.8.: Thiol-mediated ligand exchange on (A) thiol and (B) citrate-stabilized AuNPs.

Despite these concerns, the ligand exchange on citrate-stabilized AuNPs is still the method of choice for the conjugation of single stranded oligonucleotides (ssO), pioneered by the two research groups of Mirkin-Letsinger at Northwestern University and Alivisatos-Schultz at Berkeley University. As NAs do not naturally contain SH residues, this modification has to be introduced synthetically in order to provide a precise definition of the anchoring site and thus enabling the formation of a well controlled SAM.

With the establishment of a fluorescence-based method for the quantification of the surface coverage of ssO per NP, Letsinger *et al.* were able to define required reaction conditions [58]. Thus, a salt aging step seemed to be crucial in obtaining stable NPs with a high surface coverage of ssO, probably due to reduced interstrand repulsion in high ionic strength media. They observed furthermore that the footprint of the conjugates was primarily determined by the amount of added ssO. At low concentrations, the ssO are wrapped around the NP, while at high concentrations they are more likely bound in stretched shape pointing perpendicularly to the surface [59]. This at least holds for the inner part of approximately 30 bases, while the outer parts might adopt random coil configuration, promising for effective hybridization experiments (Figure 2.9). Besides concentration and chain length, nucleobase sequence seems to have an important impact on the conjugate footprint and surface coverage. Thymine for instance shows a low binding affinity to gold, favoring the stretching of ssO, resulting in higher surface coverages [60]. Moreover, different thiol anchor groups were investigated. Tridentate SH seemed to induce higher stability of conjugates than bidentante or monodentate SH ligands [61]. This fact was stressed by Dougan *et al.* They discovered that omitting the treatment with dithiothreitol (DTT) prior to conjugation, which is usually carried out to ensure that the SH-modified ssO is in a mono-thiol form rather than disulfide when applied to NPs, does not provoke a trade off in conjugate stability or surface coverage [62].
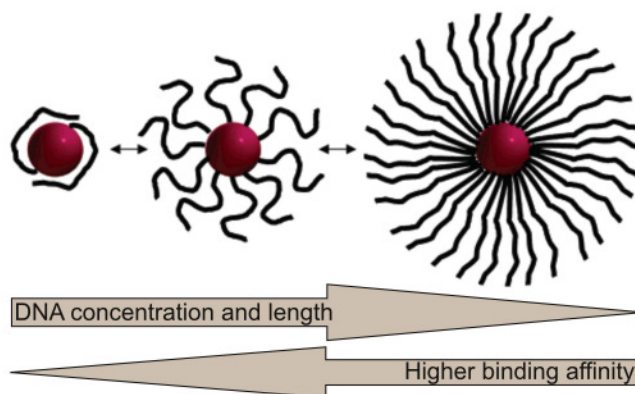
Figure 2.9.: Possible configurations of ssO attached to the surface of AuNPs in dependence of ssO concentration, spacer length and binding affinity of the nucleobase sequence.

Besides NAs, the thiol-mediated chemisorption has also been applied to protein-like structures, although the problem of inactivation during electrostatic adsorption is less dominant. There are two possible routes: either the amino acid sequence contains one or even more cysteines (Figure 2.7 C) [63], whose side chain comprises an SH residue, or the SH modification is incorporated chemically with exemplarily 2-Iminothiolan at primary amines (Figure 2.7 D) [64].

If there is no possibility of providing the biomolecule with a terminal SH group an intermediate spacer is required. For this, AuNPs can be modified with a bifunctional linker, comprising a SH anchoring group and a functional head group for further reaction with biomolecules. This could be for example an activated ester to interact with primary amines, contained in nearly every biomolecule, or a molecule with a specific recognition motif as streptavidin for biotinylated molecules (Figure 2.7 E).

2.3.3. Multifunctionalization

Multifunctional AuNPs are desired in order to enable a broad range of biological applications. For example, the combination of AuNP as imaging moiety with a recognition motif, an effector molecule (e.g., drug) and an agent supporting the cellular membrane translocation would enable a traceable drug delivery even at subcellular level. However, the bioconjugation of AuNPs with more than one functional molecule is still a severe challenge by CRM. For instance, as the ligand exchange does hardly allow for a predefinition of the surface coverage obtained with one functional molecule, the controlled conjugation of several functions by this method is even more complicated. Nevertheless, few approaches have been investigated lately. For example, Qian *et al.* re-

ported the double conjugation, beginning with an electrostatic adsorption of an organic dye followed by a thiol-mediated ligand exchange with a polyethylene glycol (PEG) (Figure 2.10 A) [65]. In the same context, Lee *et al.* described the synthesis of bifunctionalized AuNPs starting with the ligand exchange for the conjugation of NAs (siRNA) and a subsequent electrostatic adsorption of a cell penetrating agent (PBAE) to the previously conjugated siRNA (Figure 2.10 B) [66]. However, instability as consequence of an unpredictable substitution of electrostatically adsorbed molecules by examplariliy proteins contained in the serum leads to an undefined design of multifunctionalized NP during biological application. The establishment of an approach allowing an oriented immobilization of more than one molecule with predetermined surface coverage would hence considerably facilitate the design of multifunctional AuNPs.

1: ⭐ dye 2: PEG 1: HS siRNA 2: PBAE
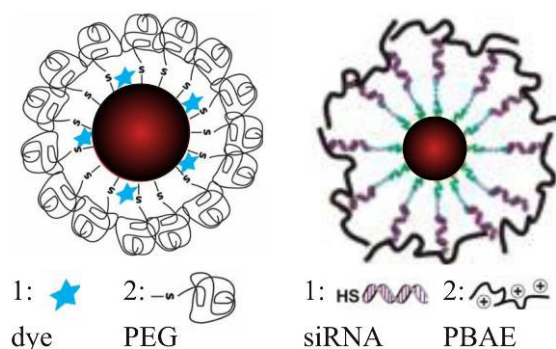
Figure 2.10.: Bifunctionalized AuNPs obtained by (A) electrostatic adsorption of a dye and ligand exchange with thiolated PEG [65] and (B) ligand exchange with thiolated siRNA and electrostatic absorption of the cell penetrating agent PBAE [66].

2.4.   Laser ablation in liquids

Laser ablation in liquids (LAL), which has been pioneered by Henglein *et al.* in 1993 [67], has become a reliable alternative to traditional CRM for obtaining noble metal NPs to date for research purposes. The basic experimental set up is mainly described, as consisting of a pulsed laser system, a set of beam guidance and focussing optical components and a vessel, containing a metal plate at the bottom, covered with a liquid layer of the desired ablation media (Figure 2.11). The formation of a nanoparticle colloid is then achieved by ablation of the metal target with intense laser radiation. The application of lasers with fs, ps and ns pulses at visible or near infrared wavelength has been described for mainly gold, silver, platinum and copper nanoparticle synthesis, while femtosecond lasers represent the gentlest method with regard to thermal impact to both the ablated material (which releases the NPs) and the surrounding liquid [36]. However, this simple method, adaptive to many materials, shows two limitations with regard to CRM, which are the deficient size control of NPs and comparably low produc-

tivity. To address the first constraint, chemical-free laser treatments are nowadays developed for size manipulation after nanoparticle synthesis. The following chapter reviews the mechanism of NP formation by LAL, characteristics of laser-generated AuNP, their bioconjugation, and size control.
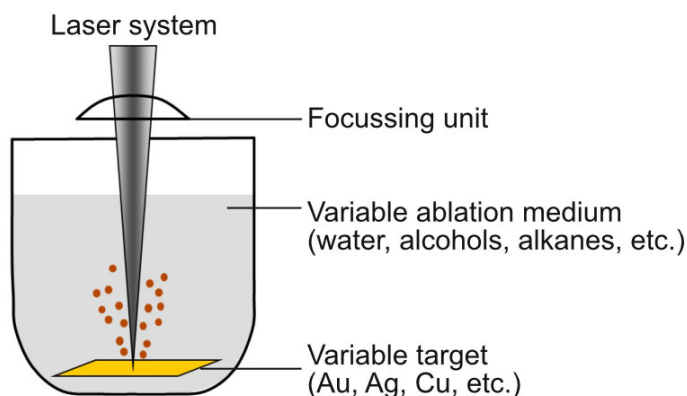
Figure 2.11.: Schematic representation of the laser ablation in liquids.

2.4.1. Mechanism of nanoparticle formation

NP formation by laser ablation has been intensively studied, but, probably due to the complexity of involved physical processes, a comprehensive understanding is still lacking. In general, laser ablation of a target starts with an energy absorption, which can produce heating and photoionization of the irradiated area. Consequently, material is ejected either as vapors, liquid droplets, solid fragments, or as an expanding plasma plume, which is to date assumed being the prevailing cause of NP generation. This plasma adiabatically expands and creates a shock wave under the confinement of the liquid, inducing an extra pressure and temperature increase in the plasma plume [68, 69]. Both plasma pressure and temperature are shown to vary with the laser wavelength [69], the thickness of the liquid layer [70], and with the focussing conditions [71]. Due to the confinement the highly excited ejected species forming the plasma stay in close proximity of the target surface [72], leading to an extremely high density, typically in the order of 10^{19}-10^{21} cm^{-3} for pulse durations of 20 to 150 ns [73]. The energy transfer is hence strongly enhanced and should lead to a secondary plasma-related ablation. With subsequent expansion of the plasma plume, the ejected species are experiencing a fast decrease of their temperature, so that after recombination of electrons and ions a cavitation bubble of vaporized solvent and condensing species remains. Thus, nucleation has started, which is directly followed by a diffusion-limited growth process, where free metal ions condense on nuclei or nuclei coalesce with each other.

Depending on the ablation medium, this growth process can continue even after the collapse of the cavitation bubble. In the case of high affinity of the metal ions with the ablation medium (e.g., Ag in water), the growth process might even last for several days [74]. The collapse of the cavitation bubble has been reported to be that violent that a generated second shock wave will expel the NPs from the target surface and cause a third round of material ejection by pressure etching [75].

Although the prevailing mechanism of NP formation during LAL consists in nucleation during plasma plume cooling followed by nuclei growth and coalescence, some authors assume the existence of additional mechanisms particularly for ns laser ablation, including the ejection of melted droplets or solid fragments from the target resulting in the formation of larger NPs [76].

2.4.2. Effect of laser parameters on nanoparticle size

According to the above described formation mechanism, the nucleation time and growth time of nuclei, influenced by temperature, pressure, and density of metal ions, determine the final size of laser-generated NPs. The applied fluence [76], wavelength, and pulse length [77] thus affect the resulting NP size. However, as temperature atomic density etc. are not homogeneous throughout the plasma plume, broad NP size distributions are characteristic of laser-generated NPs [77, 73] if no stabilizing additives are present in the ablation medium (chapter 2.4.4). Additionally, further laser interaction with already formed particles, in particular those showing an SPR-enhanced light absorption at the applied laser wavelength, induces significant changes in the NP size. In dependence of again laser fluence, pulse duration, and laser wavelength, either Coulomb explosion or heating-melting-evaporation processes are initiated. For instance, the use of high radiation intensities and short wavelength favors the NP fragmentation through the Coulomb explosion [78, 79, 80, 81], while a milder laser irradiation contributes to photothermal pathways, provoking a particle melting and their subsequent coalescence [82]. As formation of NPs by laser ablation in a batch sytem cannot be separated from these fragmentation or melting processes, it is ardous to predetermine NP size and size distribution by laser parameters in a simple and controlled way. However, these processes can be applied in a laser treatment after NP formation allowing the controlled size reduction or increase. The latter can also be triggered by the addition of variable amounts of salts, inducing particle agglomeration before mild laser irradiation [78].

2.4.3. Gold nanoparticles by laser ablation

Although reports on laser-generated AuNPs are probably dominating in literature, the formation of NPs by LAL has been studied for a broad range of materials. Some structural features were thus identified to be valid for all laser-generated metal NPs and probably implied by the above described formation mechanisms. For example, laser-generated metal NPs generally have a spherical or roughly spherical shape, while deviations are frequently observed in a minor fraction of particles, probably as a result of coalescence of nuclei soon after the nucleation process [83]. Another frequently observed feature of laser-generated metal NPs is their polycrystallinity (Figure 2.12 A), suggesting particle agglomeration due to coalescence in solution or a consequence of their deposition onto the grid for transmission electron microscopy (TEM) [84, 85].

Furthermore there are other features as size, surface characteristics, and stability, which seem to depend on the combination of ablated material and the surrounding ablation medium. AuNPs have so far been obtained by LAL in a series of pure solvents, as indicated in Table 2.1, without pretending to be exhaustive. One observes that the size distribution of AuNPs obtained by laser ablation in water is generally broader and shifted to larger average diameters compared to AuNPs generated in organic solvents. This trend is mostly referred to a strong interaction of the solvent with the surface, being competitive with particle growth. However, this does not implicitly lead to better NP stabilization in organic solvents than in water. Contrarily, AuNPs obtained by laser ablation in e.g., n-alkanes [83], dimethyl sulfoxide, acetonitrile and tetrahydrofuran [86] without any stabilizing agent are often subject to aggregation on a time scale of days or weeks, while they are stable in water over years. The mechanism behind nanoparticle stabilization in organic liquids, if observed, has not been resolved in detail so far. Also, the contribution of possible pyrolysis products of the solvent, as result of intensive laser radiation, is not clear. In this context, it has for example been reported that AuNPs, obtained by laser ablation in toluene, are embedded in a graphitic carbon matrix [87]. This fact might significantly influence stability.

Table 2.1.: AuNP size obtained by laser ablation in pure solvents.

Solvent	Diameter	Laser parameter*	Reference
n-Hexane	8 nm	5 ns, 532 nm	[83]
Dimethylsulfoxide	4.8 nm	9 ns, 1064 nm	[86]
Tetrahydrofuran	8.2 nm	9 ns, 1064 nm	[86]
Acetonitrile	3.6 nm	9 ns, 1064 nm	[86]
Toluene	1.8 nm	9 ns, 1064 nm	[87]
N-Propylamine	5-8 nm	120 fs, 800 nm	[88]
Water	120 nm	120 fs, 800 nm, $F>400$ J/cm^2	[76]
Water	4 nm	120 fs, 800 nm, $F< 100$ J/cm^2	[76]
Water	11 nm	5 ns, 1064 nm	[89]

*pulse duration, wavelength, Fluence (F)

In comparison, the stabilization of AuNPs obtained by laser ablation in water, is rather well defined by electrostatic repulsion of negatively charged species at the AuNP surface. These charged species are assigned to AuO^- by FTIR and secondary ion mass spectrometry experiments [88]. X-ray photoelectron spectroscopy, by the groups of Mafuné and Meunier, supportingly revealed the presence of Au^{1+} and Au^{3+} at the NP's surface [88, 89]. A further indication was delivered by zetapotential measurements, which showed a significantly lowered negative value with decreasing pH of the surrounding medium probably due to the equilibrium between AuOH and AuO^- species (Figure 2.12 B and C) [88]. Muto *et al.* estimated by titration with the cationic surfactant cethyltrimetyl ammonium bromide that 3.3 - 6.6 % of surface gold atoms own this negative charge at neutral pH [89]. To summarize, the laser-generated AuNPs are partially oxidized during the laser process in water, probably as consequence of the highly reactive plasma environment.
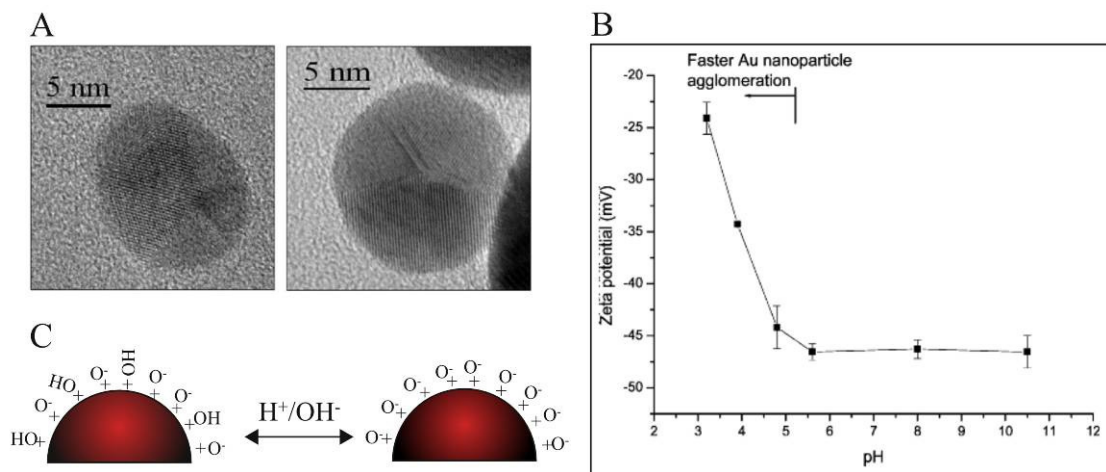
Figure 2.12.: (A) TEM images, evidencing the polycrystallinity of laser-generated AgNPs (right) and AuNPs [85]. (B) Zetapotential of laser-generated AuNPs increases in value with increasing pH of the surrounding medium [88], probably due to the (C) equilibrium between AuOH and AuO⁻ species at the NP surface.

2.4.4. Functionalization of laser-generated gold nanoparticles

Functionalization of laser-generated AuNPs can be achieved *in situ* or *ex situ* with regard to NP synthesis. This means that the functionalization agent is either directly added to the ablation medium prior to the laser process, thus enabling a simultaneous NP generation and functionalization, or it is mixed with the NPs in a second synthesis step. Due to its simplicity, the *in situ* approach is highly attractive and has thus been intensively studied. However, instead of functionalization, the main objective was predominantly the control of particles size and size distribution or the improvement of particles stability with the consequent reduction of aggregation. A wide range of surfactants have been investigated for this issue so far (Table 2.2). Exemplarily, it could be shown that the addition of dodecanthiol to decane leads to the formation of stable gold clusters with sizes smaller than those obtained in the corresponding pure liquid [84]. Obviously the added thiol, which is able to have strong dative bonds with gold, competes with growth processes like nuclei coalescence and atomic diffusion by covering the NPs surface. This observation is commonly termed size quenching effect.

Table 2.2.: AuNP size obtained by laser ablation in the presence of stabilizing agents.

Solvent	Stabilization agent	Diameter	Laserparameter*	References
n-Decane	Dodecanethiol	2-5 nm	5 ns, 532 nm	[84]
Water	SDS	14.4 nm	5 ns, 1064 nm	[90]
Water	Cyclodextrins	2-2.4 nm	110 fs, 800 nm	[91]
Water	Dextrane	1-15 nm	110 fs, 800 nm	[82]
Water	PAMAM G5	3 nm	20 ps, 532 nm	[92]
Water	PAMAM G5	7 nm	25 ps, 1064 nm	[92]

*pulse duration, wavelength, Fluence (F)

A second example is sodium dodecyl sulfate (SDS), which revealed as an excellent ligand for the size control and long time stabilization of AuNPs, obtained by laser ablation in water [90]. Mafuné *et al.* assumed that the electrostatic adsorption of the anionic surfactant is mediated by Na^+ ions. In contrast, cationic surfactants seemed to be inappropriate for AuNP stabilization, screening negative AuO^- charges with consequent particle aggregation [89].

Besides the *in situ* stabilization of AuNPs, their functionalization for further application in life science plays a minor role in literature so far [93]. Just very recently in 2009, laser-generated dextrane-coated AuNPs were proposed for biosensing of lectins [82] and another study addressed the cellular internalization of laser-generated AuNPs, conjugated to a thermosensitive polymer in an *ex situ* process [94]. This low number of reports is remarkable because authors in the field of NP formation often claim the high purity of resulting colloids as especially promising for applications in life sciences. One could hence assume that the unexplored laser pyrolysis, which could virtually affect biocompatibility and activity, is still a major limit for further application of *in situ* functionalized gold nanoparticles. It is furthermore remarkable that the *in situ* functionalization of laser-generated AuNPs has never been applied for the bioconjugation of NAs or proteins so far, although high conjugation efficiencies due to the uncoated nanoparticle surface might be estimated.

References

[1] ASTM International, E 2456-06 Terminology for Nanotechnology. 2006. Doi: 10.1520/E2456-06.

[2] S. W. Tsai, Y. Y. Chen and J. W. Liaw. Compound cellular imaging of laser scanning confocal microscopy by using gold nanoparticles and dyes. *Sensors*, 8:2306–2316, 2008.

[3] L. R. Hirsch, R. J. Stafford, J. A. Bankson, S. R. Sershen, B. Rivera, R. E. Price, J. D. Hazle, N. J. Halas and J. L. West. Nanoshell-mediated near-infrared thermal therapy of tumors under magnetic resonance guidance. *Proceedings of the National Academy of Science*, 100:13549–13554, 2003.

[4] M. Faraday. Experimental relations of gold (and other metals) by light. *Philosophical Transactions*, 147:145–181, 1857.

[5] G. Mie. Beiträge zur Optik trüber Medien, speziell kolloidaler Metallösungen. *Annalen der Physik*, 25:377–445, 1908.

[6] P. K. Jain, I. H. El-Sayed and M. A. El-Sayed. Au nanoparticles target cancer. *Nanotoday*, 2:18–29, 2007.

[7] P. K. Jain, K. S. Lee, I. H. El-Sayed and M. A. El-Sayed. Calculated absorption and scattering properties of gold nanoparticles of different size, shape, and composition: Applications in biological imaging and biomedicine. *Journal of Physical Chemistry B*, 110:7238–7248, 2006.

[8] H. Du, R.-C. A. Fuh, J. Li, L. A. Corkan and J. S. Lindsey. PhotochemCADDagger: A computer-aided design and research tool in photochemistry. *Photochemistry and Photobiology*, 68:141–142, 1998.

[9] S. Link, M. B. Mohamed and M. A. El-Sayed. Simulation of the optical absorption spectra of gold nanorods as a function of their aspect ratio and the effect of the medium dielectric constant. *Journal of Physical Chemistry B*, 103:3070–3077, 1999.

[10] K. L. Kelly, E. Coronado, L. L. Zhao and G. C. Schatz. The optical properties of metal nanoparticles: the influence of size, shape and dielectric environment. *Journal of Physical Chemistry B*, 107:668–677, 2003.

[11] G. Raschke, S. Kowarik, T. Franzl, C. Sonnichsen, T. A. Klar and J. Feldmann. Biomolecular recognition based on single gold nanoparticle light scattering. *Nano Letters*, 3:935–938, 2003.

[12] R. Wilson. The use of gold nanoparticles in diagnostics and detection. *Chemical Society Reviews*, 37:2028–2045, 2008.

[13] W. Jiang, B. Y. S. Kim, J. T. Rutka and W. C. W. Chan. Nanoparticle-mediated cellular response is size-dependent. *Nature Nanotechnology*, 3:145–150, 2008.

[14] B. D. Chithrani and W. C. W. Chan. Elucidating the mechanism of cellular uptake and removal of protein-coated gold nanoparticles of different sizes and shapes. *Nano Letters*, 7:1542–1550, 2007.

[15] D. B. Chithrani, A. A. Ghazani and W. C. W. C. Chan. Determining the size and shape dependence of gold nanoparticle uptake into mammalian cells. *Nano Letters*, 6:662–668, 2006.

[16]   K. T. Thurn, E. M. B. Brown, A. Wu, S. Vogt, B. Lai, J. Maser, T. Paunesko and G. E. Woloschak. Nanoparticles for applications in cellular imaging. *Nanoscale Research Letters*, 2:430–441, 2007.

[17]   M. Everts, V. Saini, J. L. Leddon, R. J. Kok, M. Stoo-Khalili, M. A. Preuss, C. L. Millican, G. Perkins, J. M. Brown, H. Bagaria, D. E. Nikles, D. T. Johnson, V. P. Zharov and D. T. Curiel. Covalently linked Au nanoparticles to a viral vetcor: Potential for combined photothermal and gene cancer therapy. *Nano Letters*, 6:587–591, 2006.

[18]   X. Shi, S. Wang, S. Meshinchi, M. E. Van Antwerp, X. Bi, I. Lee and J. R. Baker. Dendrimer-entrapped gold nanoparticles as a platform for cancer-cell targeting and imaging. *Small*, 3:1245–1252, 2007.

[19]   M. Green and P. M. Loewenstein. Autonomous functional domains of chemically synthesized human immunodeficiency virus at tat trans-activator protein. *Cell*, 55:1179–1188, 1988.

[20]   D. Derossi, A. H. Joliot, G. Chassaing and A. Prochiantz. The third helix of the antennapedia homeodomain translocates through biological membranes. *Journal of Biological Chemistry*, 269:1044–10450, 1994.

[21]   K. M. Stewart, K. L. Horton and S. O. Kelley. Cell-penetrating peptides as delivery vehicles for biology and medicine. *Organic and Biomoelcular Chemistry*, 6:2242–2255, 2008.

[22]   A. G. Tkachenko, H. Xie, Y. Liu, D. Coleman, J. Ryan, W. R. Glomm, M. K. Shipton, S. Franzen and D. L. Feldheim. Cellular trajectories of peptide-modified gold particle complexes: Comparison of nuclear localization signals and peptide transduction domains. *Bioconjugate Chemistry*, 15:482–490, 2004.

[23]   J. M. de la Fuente and C. C. Berry. Tat peptide as an efficient molecule to translocate gold nanoparticles into the cell cucleus. *Bioconjugate Chemistry*, 16:1176–1180, 2005.

[24]   T. Inasaki and S. Kobayashi. Particle size effects of gold on the kinetics of the oxygen reduction at chemically prepared Au/C catalysts. *Electrochimica Acta*, 54:4893–4897, 2009.

[25]   Y.-S. Chen, Y.-C. Hung, I. Liau and G. S. Huang. Assessment of the in vivo toxicity of gold nanoparticles. *Nanoscale Research Letters*, 4:858–864, 2009.

[26]   N. Lewinski, V. Colvin and R. Drezek. Cytotoxicity of nanoparticles. *Small*, 4:26–49, 2008.

[27]   K. B. Male, B. Lachance, S. Hraopovic, G. Sunaharam and J. H. T. Luong. Assessment of cytotoxicity of quantum dots and gold nanoparticles using cell-baed impedance spectroscopy. *Analytical Chemistry*, 80:5487–5493, 2008.

[28]   M. Thomas and A. M. Klibanov. Conjugation to gold nanoparticles enhances polyethylenimine's transfer of plasmid DNA into mammalian cells. *Proceedings of the National Academy of Science*, 100:9138–9143, 2003.

[29]   C. M. Goodman, C. D. McCuster, T. Yilmaz and V. M. Rotello. Toxicity of gold nanoparticles functionalized with cationic and anionic side chains. *Bioconjugate Chemistry*, 15:897–900, 2004.

[30]   Y. Pan, S. Neuss, A. Leifert, M. Fischler, F. Wen, U. Simon, G. Schmid, W. Brandau and W. Jahnen-Dechent. Size-dependent cytotoxicity of gold nanoparticles. *Small*, 3:1941–1949, 2007.

[31]   Y. Pan, A. Leifert, D. Ruau, S. Neuss, J. Bornemann, G. Schmid, W. Brandau, U. Simon and W. Jahnen-Dechent. Gold nanoparticles of diameter 1.4 nm trigger necrosis by oxidative stress and mitochondrial damage. *Small*, 5:2067–2076, 2009.

[32]   N. Pernodet, X. Fang, Y. Sun, A. Bakhtina, A. Ramakrishnan, J. Sokolov, A. Ulman and M. Rafailovich. Adverse effects of citrate/gold nanoparticles on human dermal fibroblasts. *Small*, 2:766–773, 2006.

[33]   N. Singh, B. Manshian, J. G. J.S., S. M. Griffiths, P. M. Williams, T. G. Maffeis, C. J. Wright and S. H. Doak. NanoGenotoxicology: The DNA damaging potential of engineered nanomaterials. *Biomaterials*, 30:3891–3914, 2009.

[34]   E. E. Connor, J. Mwamuka, A. Gole, Murphy, C. J. and M. D. Wyatt. Gold nanoparticles are taken up by human cells but do not cause acute cytotoxicity. *Small*, 1:325 –327, 2005.

[35]   M. A. Watzky and R. G. Finke. Transition metal nanocluster formation kinetic and mechanistic studies. A new mechanism when hydrogen is the reductant: Slow, continuous nucleation and fast autocatalytic surface growth. *Journal of the American Chemical Society*, 119:10382–10400, 1997.

[36]   M.-C. Daniel and D. Astruc. Gold nanoparticles: Assembly, supramolecular chemistry, quantum-size-related properties, and applications toward biology, catalysis, and nanotechnology. *Chemical Reviews*, 104:293–346, 2004.

[37]   H. Bönnemann, W. Brijoux, R. Brinkmann, M. Feyer, W. Hofstadt, G. Khelashvili, N. Matoussevitsch and K. S. Nagabhushana. Nanostructured transition metals. *The Strem Chemiker*, 21:1–18, 2004.

[38]   J. Turkevich, P. C. Stevenson and J. Hillier. A study of nucleation and growth processes in the synthesis of colloidal gold. *Discussions of the Faraday Society*, 11:55–75, 1951.

[39]   S. Kumar, K. S. Gandhi and R. Kumar. Modeling of formation of gold nanoparticles by citrate method. *Industrial & Engineering Chemistry Research*, 46:3128–3136, 2007.

[40]   G. Frens. Controlled nucleation for the regulation of the particle size in monodisperse gold suspensions. *Nature Physical Science*, 241:20–21, 1973.

[41]   National Institute of Standards & Technology, Report of investigation on reference material 8011 - gold nanoparticles, nominal 10 nm diameter. 2007.

[42]   Sigma-Aldrich. G1652 Gold Colloids. Technical report.

[43]   G. Schmid, R. Pfeil, R. Boese, F. Bandermann, S. Meyer, G. H. M. Calis and J. W. A. van der Velden. $Au_{55}[P(C_6H_5)_3]_{12}Cl_6$ - ein Goldcluster ungewöhnlicher Größe. *Chemische Berichte*, 114:3634– 3642, 1981.

[44]   W. M. Pankau. *Thermostabile und monokonjugierbare Goldcluster-Komplexe*. Ph.D. thesis, Bochum, 2002.

[45]   M. Brust, M. Walker, D. Bethell, D. J. Schiffrin and R. Whyman. Synthesis of thiol-derivatised gold nanoparticles in a two-phase liquid-liquid system. *Journal of the Chemical Society, Chemical Communications*, 7:801–802, 1994.

[46]   C. A. Waters, A. J. Mills, K. A. Johnson and D. J. Schiffrin. Purification of dodecanethiol derivatized gold nanoparticles. *Chemical Communications*, 7:540–541, 2003.

[47]   L. S. Sun, R. M. Crooks and V. Chechik. Preparation of polycyclodextrin hollow spheres by templating gold nanoparticles. *Chemical Communications*, pages 359–360, 2001.

[48] R. G. Nuzzo and D. L. Allara. Adsorption of bifunctional organic disulfides on gold surfaces. *Journal of the American Chemical Society*, 105:4481–4483, 1983.

[49] A. Ulman. Formation and structure of self-assembled monolayers. *Chemical Reviews*, 96:1533–1554, 1996.

[50] A. Badia, R. B. Lennox and L. Reven. A dynamic view of self-assembled monolayers. *Accounts of Chemical Research*, 33:475–481, 2000.

[51] E. Katz and I. Willner. Integrierte Hybridsysteme aus Nanopartikeln und Biomolekülen: Synthese, Eigenschaften und Anwendungen. *Angewandte Chemie*, 116:6166–6235, 2004.

[52] W. Shenton, S. A. Davis and S. Mann. Directed self-assembly of nanoparticles into macroscopic materials using antibody-antigen recognition. *Advanced Materials*, 11:499–502, 1999.

[53] W. Yang, D. Trau, R. Renneberg, N. T. Tu and F. Caruso. Layer-by-layer construction of novel biofunctional fluorescent microparticles for immunoassay applications. *Journal of Colloid and Interface Science*, 234:356–362, 2001.

[54] L. A. Gearheart, H. J. Ploehn and C. J. Murphy. Oligonucleotide adsorption to gold nanoparticles: A surface-enhanced Raman spectroscopy study of intrinsically bent DNA. *Journal of Physical Chemistry B*, 105:12609–12615, 2001.

[55] A. Caragheorgheopol and V. Chechik. Mechanistics aspects of ligand exchange in Au nanoparticles. *Physical Chemistry Chemical Physics*, 10:5029–5041, 2008.

[56] M. G. Bellino, E. J. Calvo and G. Gordillo. Adsorption kinetics of charged thiols on gold nanoparticles. *Physical Chemistry Chemical Physics*, 6:1425–1436, 2004.

[57] S. H. Brewer, W. R. Glomm, M. C. Johnson, M. K. Knag and S. Franzen. Probing BSA binding to citrate-coated gold nanoparticles and surfaces. *Langmuir*, 21:9303–9307, 2005.

[58] L. M. Demers, C. A. Mirkin, R. C. Mucic, R. A. Reynolds, R. L. Letsinger, R. Elghanian and G. Viswanadham. A fluorescence-based method for determining the surface coverage and hybridization efficiency of thiol-capped oligonucleotides bound to gold thin films and nanoparticles. *Analytical Chemistry*, 72:5535–5541, 2000.

[59] W. J. Parak, T. Pellegrino, C. M. Micheel, D. Gerion, S. C. Williams and A. P. Alivisatos. Conformation of oligonucleotides attached to gold nanocrystals probed by gel electrophoresis. *Nano Letters*, 3:33–36, 2003.

[60] J. J. Storhoff, R. Elghanian, C. A. Mirkin and R. L. Letsinger. Sequence-dependent stability of DNA-modified gold nanoparticles. *Langmuir*, 18:6666–6670, 2002.

[61] Z. Li, R. Jin, C. A. Mirkin and R. L. Letsinger. Multiple thiol-anchor capped DNA-gold nanoparticle conjugates. *Nucleic Acids Research*, 30:1558–1562, 2002.

[62] J. A. Dougan, C. Karlsson, W. E. Smith and D. Graham. Enhanced oligonucleotide nanoparticle conjugate stability using thioctic acid modified oligonucleotides. *Nucleic Acids Research*, 35:3668–3675, 2007.

[63] M. A. Hayat. *Colloidal Gold: Principles, Methods and Applications*. Academic Press, New York, 1989.

[64]   S. S. Ghosh, P. M. Kao, A. W. McCue and H. L. Chapelle. Use of maleimide-thiol coupling chemistry for efficient syntheses of oligonucleotide-enzyme conjugate hybridization probes. *Bioconjugate Chemistry*, 1:71–76, 1990.

[65]   X. Qian, X.-H. Peng, D. O. Ansari, Q. Yin-Goen, G. Z. Chen, D. Z. Shin, L. Yang, A. N. Young, M. D. Wang and S. Nie. In vivo tumor targeting and spectroscopic detection with surface-enhanced Raman nanoparticle tags. *Nature Biotechnology*, 26:83–90, 2008.

[66]   J.-S. Lee, J. J. Green, K. T. Love, J. Sunshine, R. Langer and D. G. Anderson. Gold, Poly (beta-amino ester) nanoparticles for small interfering RNA delivery. *Nano Letters*, 9:2402–2406, 2009.

[67]   A. Fojtik and A. Henglein. Laser ablation of films and suspended particles in a solvent - formation of cluster and colloid solutions. *Berichte der Bunsen-Gesellschaft für Physikalische Chemie*, 97:252–254, 1993.

[68]   L. Berthe, R. Fabbra, P. Peyre and E. Bartnicki. Wavelength dependent of laser shock-wave generation in the water-confinement regime. *Journal of Applied Physics*, 85:7552–7555, 1999.

[69]   L. Berthe, A. Sollier, P. Peyre, R. Fabbro and E. Bartnicki. The generation of laser shock waves in a water-confinement regime with 50 ns and 150 ns XeCl excimer laser pulses. *Journal of Physics D: Applied Physics*, 33:2142–2145, 2000.

[70]   S. Zhu, Y. F. Lu and M. H. Hong. Laser ablation of solid substrates in a water-confined environment. *Applied Physics Letters*, 79:1396–1398, 2001.

[71]   J. P. Sylvestre, A. V. Kabashin, E. Scaher and M. Meunier. Femtosecond laser ablation of gold in water: influence of the laser-produced plasma on the nanoparticle size distribution. *Applied Physics A*, 80:753–758, 2005.

[72]   H. Oguchi, T. Sakka and Y. H. Ogata. Effects of pulse duration upon the plume formation by the laser ablation of Cu in water. *Journal of Applied Physics*, 102:023306, 2007.

[73]   T. Sakka, S. Iwanaga, Y. H. Ogata, A. Matsunawa and T. Takemoto. Laser ablation at solid-liquid interfaces: An approach from optical emission spectra. *The Journal of Chemical Physics*, 112:8645–8653, 2000.

[74]   F. Mafuné, J. Kohno, Y. Takeda, T. Kondow and H. Sawabe. Formation and size control of silver nanoparticles by laser ablation in aqueous solution. *Journal of Physical Chemistry B*, 104:9111–9117, 2000.

[75]   W. T. Nichols, T. Sasaki and N. Kashizakia. Laser ablation of a platinum target in water. I. Ablation mechanisms. *Journal of Applied Physics*, 100:114911, 2006.

[76]   A. V. Kabashin and M. Meunier. Synthesis of colloidal nanoparticles during femtosecond laser ablation of gold in water. *Journal of Applied Physics*, 94:7941–7943, 2003.

[77]   G. Yang. Laser ablation in liquids: Applications in the synthesis of nanocrystals. *Progress in Materials Science*, 52:648–698, 2007.

[78]   V. Amendola and M. Meneghetti. Controlled size manipulation of free gold nanoparticles by laser irradiation and their facile bioconjugation. *Journal of Materials Chemistry*, 17:4705–4710, 2007.

[79]   K. Yamada, Y. Tokumoto, T. Nagata and F. Mafuné. Mechanism of laser-induced size-reduction of gold nanoparticles as studied by nanosecond transient absorption spectroscopy. *Journal of Physical Chemistry B*, 110:11751–11756, 2006.

[80] H. Muto, K. Miyajima and F. Mafuné. Mechanism of laser-induced size reduction of gold nanoparticles as studied by single and double laser pulse excitation. *Journal of Physical Chemistry C*, 112:5810–5815, 2008.

[81] A. Besner, A. Kabashin and M. Meunier. Two-step femtosecond laser ablation-based method for the synthesis of stable and ultra-pure gold nanoparticles in water. *Applied Physics A*, 88:269–272, 2007.

[82] S. Besner, A. Kabashin, F. Winnik and M. Meunier. Synthesis of size-tunable polymer protected gold nanoparticles by femtosecond laser-based ablation and seed growth. *Journal of Physical Chemistry B*, 113:9526–9531, 2009.

[83] G. Compagnini, A. A. Scalisi and O. Puglisi. Production of gold nanoparticles by laser ablation in liquid alkanes. *Journal of Applied Physics*, 94:7874–7877, 2003.

[84] G. Compagnini, A. A. Scalisi, O. Puglisi and C. Spinella. Synthesis of gold colloids by laser ablation in thiol-alkane solutions. *Journal of Materials Research*, 19:2795–2798, 2004.

[85] V. Amendola and M. Meneghetti. Laser ablation synthesis in solution and size manipulation of noble metal nanoparticles. *Physical Chemistry Chemical Physics*, 11:3805–3821, 2009.

[86] V. Amendola, S. Polizzi and M. Meneghetti. Laser ablation synthesis of gold nanoparticles in organic solvents. *Journal of Physical Chemistry B*, 110:7232–7237, 2006.

[87] V. Amendola, G. A. Rizzi, S. Polizzi and M. Meneghetti. Synthesis of gold nanoparticles by laser ablation in toluene: quenching and recovery of surface plasmon absorption. *Journal of Physical Chemistry B*, 109:23125–23128, 2005.

[88] J. P. Sylvestre, S. Poulin, A. V. Kabashin, E. Sacher, M. Meunier and J. H. T. Luong. Surface chemistry of gold nanoparticles produced by laser ablation in aqueous media. *Journal of Physical Chemistry B*, 108:16864–16869, 2004.

[89] H. Muto, K. Yamada, K. Miyajima and F. Mafuné. Estimation of surface oxide on surfactant-free gold nanoparticles laser-ablated in water. *Journal of Physical Chemistry C*, 111:17221–17226, 2007.

[90] F. Mafuné, J. Kohno, Y. Takeda and T. Kondow. Dissociation and aggregation of gold nanoparticles under laser irradiation. *Journal of Physical Chemistry B*, 105:9050–9056, 2001.

[91] A. V. K. Kabashin, M. Meunier, C. Kingston and J. H. T. Luong. Fabrication and characterization of gold nanoparticles by femtosecond laser ablation in an aqueous solution of cyclodextrins. *Journal of Physical Chemistry B*, 107:4527–4531, 2003.

[92] E. Giorgetti, A. Giusti, S. C. Laza, P. Marsili and F. Giammanco. Production of colloidal gold nanoparticles by picosecond laser ablation in liquids. *Physica status solidi (a)*, 204:1693–1698, 2007.

[93] S. Barcikowski, F. Devesa and K. Moldenhauer. Impact and structure of literature on nanoparticle generation by laser ablation in liquids. *Journal of Nanoparticle Research*, 11:1883–1893, 2009.

[94] S. Salmaso, P. Caliceti, V. Amendola, M. Moreno, J. P. Magnusson, G. Pasparakisc and C. Alexander. Cell up-take control of gold nanoparticles functionalized with a thermoresponsive polymer. *Journal of Materials Chemistry*, 19:1608–1615, 2009.

3. Toxicity and cellular uptake of laser-generated gold nanoparticles

The comprehensive understanding of toxicity and cellular uptake of AuNPs is crucial for their successful biological application. Many studies, performed with chemically derived AuNPs, evidence that both properties are significantly influenced by the NP size, shape and surface. As AuNPs, obtained by laser ablation in water, are characterized by a unique surface chemistry not reproducible by any other method, they might also have unique characteristics with regard to biocompatibility and cellular uptake. One main structural difference of laser-generated AuNPs is their ligand-free, positively charged surface, which is partly associated with hydroxyl and deprotonated hydroxyl groups in dependence of the pH of the surrounding medium (chapter 2.4.3). Molecules with electron donor moieties are hence significantly attracted to the positively charged AuNPs surface. For example, unmodified ssO were found to adsorb easily onto laser-generated NPs, while the adsorption onto AuNP derived by the Turkevich method, was less dominant, although the zetapotential of the bare NPs was comparable (Figure 3.1).
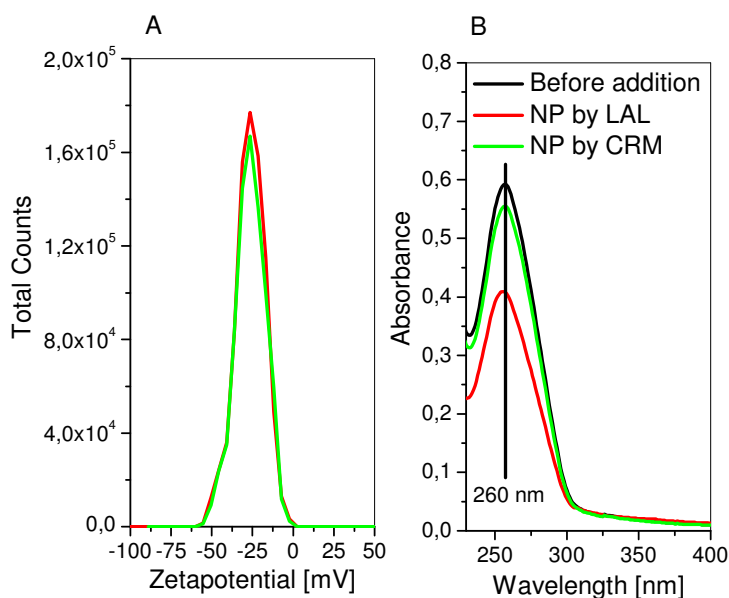

Figure 3.1.: (A) Zetapotential of laser-generated and chemically derived AuNPs (Strem Chemicals, Inc). (B) UV-spectra of remaining ssO after 1 hour of AuNP co-incubation and sedimentation of NPs by centrifugation. The difference at 260 nm compared to the value before NP addition is due to the binding of ssO to NPs and their resulting co-sedimentation.

These findings raised the concern that such a binding to AuNPs might occur unintentionally during each biological application, possibly provoking a strong effect on the biofunctionality of involved biomolecules. In this context, the first comprehended paper (chapter 3.1) deals with the co-incubation of laser-generated AuNPs with a DNA plasmid, encoding the recombinant eGFP-HMGB1 fusion protein, prior to cellular transfection. This sensitive model was chosen, as successful functional transfection events require non-hindered cellular transfection, plasmid functionality and protein synthesis. Additionally, the HMGB1 protein is a transcription factor, which strongly binds to nuclear DNA; thus any effect on the bioactivity of the synthesized protein can be also detected. We observed no adverse effect due to NP co-incubation, but nearly a sixfold enhanced transfection efficiency, when applying AuNPs of hydrodynamic diameter between 24 and 59 nm, became obvious.

The second article (chapter 3.2) deals with the cellular internalization, the intracellular fate and the cytotoxicity of laser-generated AuNPs on bovine endothelial cells. Cellular uptake was followed by laser scanning confocal microscopy (LSCM), revealing a time-dependent uptake up to 48 h of co-incubation, as it has been observed for chemically derived NPs before (chapter 2.1.2). But interestingly, no co-localization of AuNPs with endosome or lysosome marker was detected. Additionally co-incubation at 4 °C did not inhibit AuNP uptake. These results make it highly unlikely that the AuNPs entered the cells via the endocytic pathway. A more probable explanation is a translocation across cellular membranes via diffusion. Regarding cell viability, several aspects have been examined, including microscopic assessment of cell morphology, flow cytometric measurement of membrane integrity, and immunohistochemical evaluation of DNA strand breaks. No detrimental effect after a co-incubation period of up to 96 h on the overall cell population was detected. However, a cell proliferation trial, working with a ten times lower cell number, picked up cytotoxic effects of the laser-generated AuNPs at the same concentration of 50 µM gold. At this concentration, 6×10^6 AuNPs are theoretically available for each cell. It has to be mentioned, that this number more than exceeds the amount needed for the marking of cellular features, as LSCM was shown to enable the detection of 60 - 80 nanometer-sized AuNPs down to single particle level (Figure 3.2, own paper not included in the thesis [1]). Hence, aggregates of 16 AuNPs with a size of 15 nm should also be visualizable. We assume, that this defined size-dependent optical detection limit of spherical AuNPs could be used for a status-dependent visualization of AuNPs with important implications for bioanalytical applications.
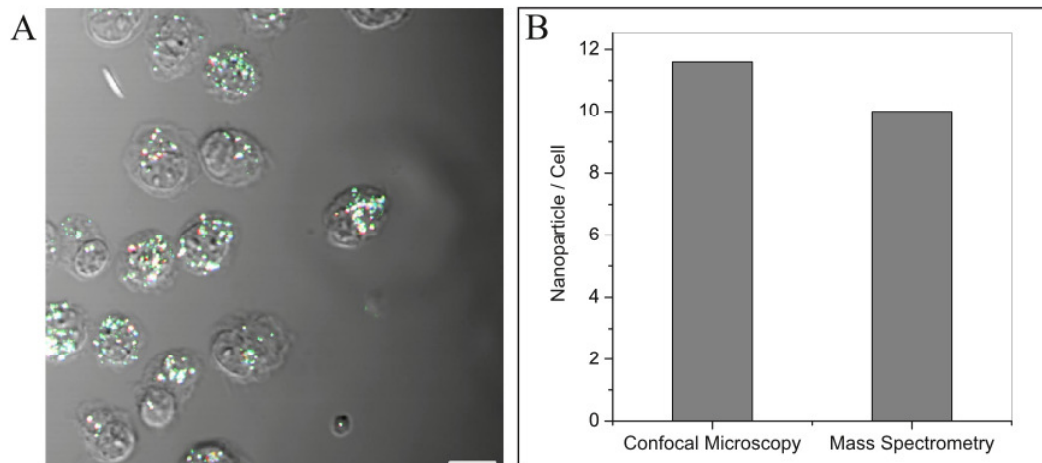
Figure 3.2.: (A) Representative LSCM image of bovine endothelial cells after 48 h incubation with 50 μM 60-80 nanometer-sized AuNPs (image size 115.2 x 115.2 x 10.4 μm). AuNPs are visualized as overlay of reflection after 543 nm excitation and luminescence after 543 nm and 633 nm excitation. (B) The number of AuNPs per cell, counted under the confocal microscope, correlates well with the number, calculated via gold quantification by inductive coupled plasma mass spectrometry. Single nanoparticles down to a size of 60 nm are quantitatively visualizable by confocal microscopy. (Own paper not included in the thesis [1])

In conclusion, despite their highly reactive surface, laser-generated AuNPs show no adverse effects on the biofunctionality of eGFP-C1-HMGB1 expression plasmid and the synthesized fusion protein and on cell viability of bovine endothelial cells at concentrations of 250 ng Au/μg plasmid and 3×10^6 NPs/cell respectively. Although a generalization is not possible, we assume these findings as representative and conclude that ligand-free laser-generated AuNPs are non-toxic at given concentrations. Moreover, the ligand-free surface seems to induce a non-endosomal cellular internalization, which might be especially interesting for biomedical applications, based on the interaction with compartments in the cytoplasm.

3.1. Co-transfection of plasmid DNA and laser-generated gold nanoparticles does not disturb the bioactivity of GFP-HMGB1 fusion protein

Svea Petersen, Jan Thies Soller, Siegfried Wagner, Andreas Richter, Jörn Bullerdiek, Ingo Nolte, Stephan Barcikowski, and Hugo Murua Escobar

Co-transfection of plasmid DNA and laser-generated gold nanoparticles does not disturb the bioactivity of GFP-HMGB1 fusion protein

Svea Petersen[†1], Jan T Soller[†2,3], Siegfried Wagner[2,3], Andreas Richter[3], Jörn Bullerdiek[2,3], Ingo Nolte[2], Stephan Barcikowski[1], and Hugo Murua Escobar[2]

[1]Laser Zentrum Hannover e.V., Hannover, Germany
[2] Small Animal Clinic, University of Veterinary Medicine, Hannover, Germany
[3] Centre for Human Genetics, University of Bremen, Bremen, Germany
[†] Equal contributors

Abstract

Ultrashort-pulsed laser ablation in liquids represents a powerful tool for the generation of pure gold nanoparticles (Au-NPs) avoiding chemical precursors and thereby making them especially interesting for biomedical applications. However, because of their electron accepting properties, laser-generated Au-NPs might affect biochemical properties of biomolecules, which often adsorb onto the nanoparticles. We investigated possible effects of such laser-generated Au-NPs on biological functionality of DNA molecules. We tested four differently sized positively charged Au-NPs by incubating them with recombinant eGFP-C1-HMGB1 DNA expression plasmids that code for eGFP fusion proteins and contain the canine architectural transcription factor HMGB1. We were able to show that successfully transfected mammalian cells are still able to synthesize and process the fusion proteins. Our observations revealed that incubation of Au-NP with the plasmid DNA encoding the recombinant canine HMGB1 neither prevented the mediated uptake of the vector through the plasma membrane in presence of a transfection reagent nor had any effect on the transport of the synthesized fusion proteins to the nuclei. Biological activity of the recombinant GFP-HMGB1 fusion protein appears to have not been affected either, as a strong characteristic protein accumulation in the nucleus could be observed. We also discovered that transfection efficiencies depend on the size of Au-NP. In conclusion, our data indicate that laser-generated Au-NPs present a good alternative to chemically synthesized nanoparticles for use in biomedical applications.

Findings

Gold nanoparticles (Au-NPs) are used widely for various biomedical applications including cell imaging [1], diagnostics [2], targeted drug delivery [3], and sensing [4]. Various methods have been established for Au-NP generation. Many of these rely on several chemical reactions or gas pyrolysis, showing the risk of impurities or agglomeration [5]. Laser ablation in liquids showed to be a powerful tool with many advantages, having almost no restriction in the choice of source material and the ability of yielding highly pure colloidal particles [6-11]. These pure Au-NPs are characterized by their unique surface chemistry free of surfactants, a feature unattainable by other methods [12-14]. X-ray photoelectron spectroscopy of such Au-NPs revealed the presence of the oxidation states Au^+ and Au^{3+} at the Au-NP surface [13]. In previous studies we demonstrated that unmodified DNA oligonucleotides adsorb easily onto these positively charged nanoparticles [15,16], probably via amino- and keto-groups, which interact with the electron accepting surface of the generated Au-NPs. However, these findings raised the possibility that more complex biomolecules could also be attracted and bound to such nanoparticles' surfaces, if incubated intentionally or unintentionally with colloidal laser-generated gold nanoparticles, even if no additional conjugation is envisaged. Such binding could have a strong effect on the properties of biomolecules and should be cha-racterized with a view of their potential toxicity [17]. We therefore decided to analyze the possible effects of laser-generated Au-NPs on DNA functionality. For this reason we incubated the charged particles with recombinant eGFP-C1-HMGB1 expression plasmids and subsequently transfected them into mammalian cells. As the HMGB1 protein is normally highly abundant in the cell nuclei, we were able to show that the treated expression plasmids are still functional and suitable for use as transcription matrix, because the transfected cells were still able to synthesize the fusion proteins, to process them, and to transport them to their biofunctional destination. The effect of four differently sized nanoparticles on the activity of the eGFP-C1-HMGB1 plasmid was investigated by fluorescence microscopy. We additionally performed a binding assay to investigate structural effects on the plasmid due to Au-NP co-incubation.
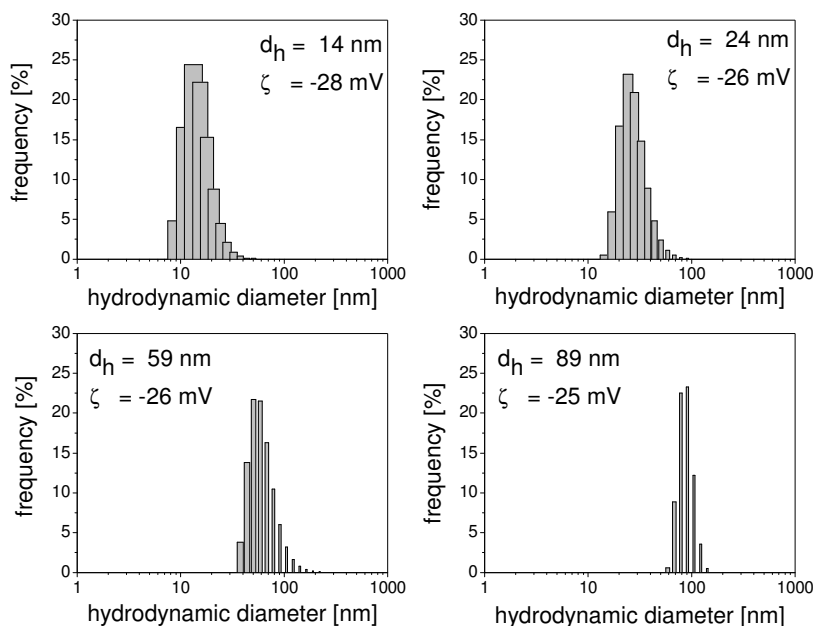
Figure 1.: Size distribution and surface charge of laser-generated gold nanoparticles. Gold nanoparticles were generated by laser ablation in water using a femtosecond laser system (Spitfire Pro, Spectra-Physics) delivering 120 fs laser pulses at a wavelength of 800 nm (working pulse energy: 200 µJ per pulse, beam diameter: 4 mm). In order to generate four suspensions containing differently sized nanoparticles, the focal position was lowered from one generation experiment to the other (0 mm, -2 mm, -4 mm relative to the focus in air) resulting in the colloidal suspensions containing nanoparticles with mean hydrodynamic diameters of d_h = 89 nm, d_h = 5 nm and d_h = 24 nm. For the generation of 14 nanometer-sized nanoparticles, laser ablation was carried out at a focal position of -4 mm and then reirradiated for 5 min at 1 mJ with an Nd-YLF laser system (pulse length: 27 ns, 1047 nm, 5 kHz). The hydrodynamic size distribution was analyzed by dynamic light scattering.

Nanoparticle generation

Au-NPs were generated by laser ablation in water, as recently reported in detail [16]. Briefly, the beam of a femtosecond laser system (Spitfire Pro, Spectra-Physics), delivering 120 fs laser pulses at a wavelength of 800 nm, was focused with a 40 mm lens on a 99.99 % pure gold target placed at the bottom of a Petri dish filled with 2 mL of ddH2O. A pulse energy of 200 µJ at 5 kHz repetition rate was employed for 12 min. According to observations of Kabashin *et al.* [9] the focal position was lowered from one generation experiment to the other (0 mm, -2 mm, -4 mm relative to the focus in air) in order to obtain colloidal suspensions containing Au-NPs with mean hydrodynamic diameters of d_h= 89 nm, d_h= 59 nm, and d_h= 24 nm. The remaining small particles were removed by centrifugation at 15000 rpm for 10 min. To generate 14 nm Au-NPs, laser ablation was carried out at a focal position of -4 mm, followed by a second irradiation for 5 min at 1 mJ with an Nd-YLF laser system (pulse length: 27 ns, 1047 nm, 5 kHz), as was described recently [7, 18]. Characterization of nanoparticle suspensions was performed by dynamic light scattering using a Malvern Zetasizer and by UV-Vis spectroscopy using a Shimadzu 1650. The hydrodynamic number distributions and the average zeta potential of the colloids are shown in Figure 1.

The zeta potential seems to be independent of the nanoparticle size, which might be explained by a similar surface charge density. The particle mass concentration in the suspensions was determined by weighing the sediment after water evaporation.

Au-NP and eGFP-C1-HMGB1 vector in vitro transfection assay

The synthesized Au-NP suspensions were sterilized by filtration through a 0.2 µm filter device (Millex-GV Sterilizing Filter Unit, Millipore, Billerica, USA). Subsequently, 250 ng of each differently sized Au-NPs were incubated for 24 h at room temperature with 1 µg of recombinant plasmid eGFP-C1-HMGB1 in a total volume of 47 µl of ddH2O. The time of co-incubation was intentionally kept that long as we aimed to investigate possible effects on the vector due to nanoparticle interferences. This was only possible as the circular double-stranded plasmid is not susceptible to rapid degenerative processes. The recombinant plasmid encodes an eGFP-HMGB1 fusion protein. The HMGB1 coding sequence was derived from canine cDNA using PCR amplification (primer pair EcoR1_B15'CGGAATTCACCATGGGCAAAGG AGA3'/.KpnI_B1(5'GCGGTACCTTATTCATCAT CATC3').
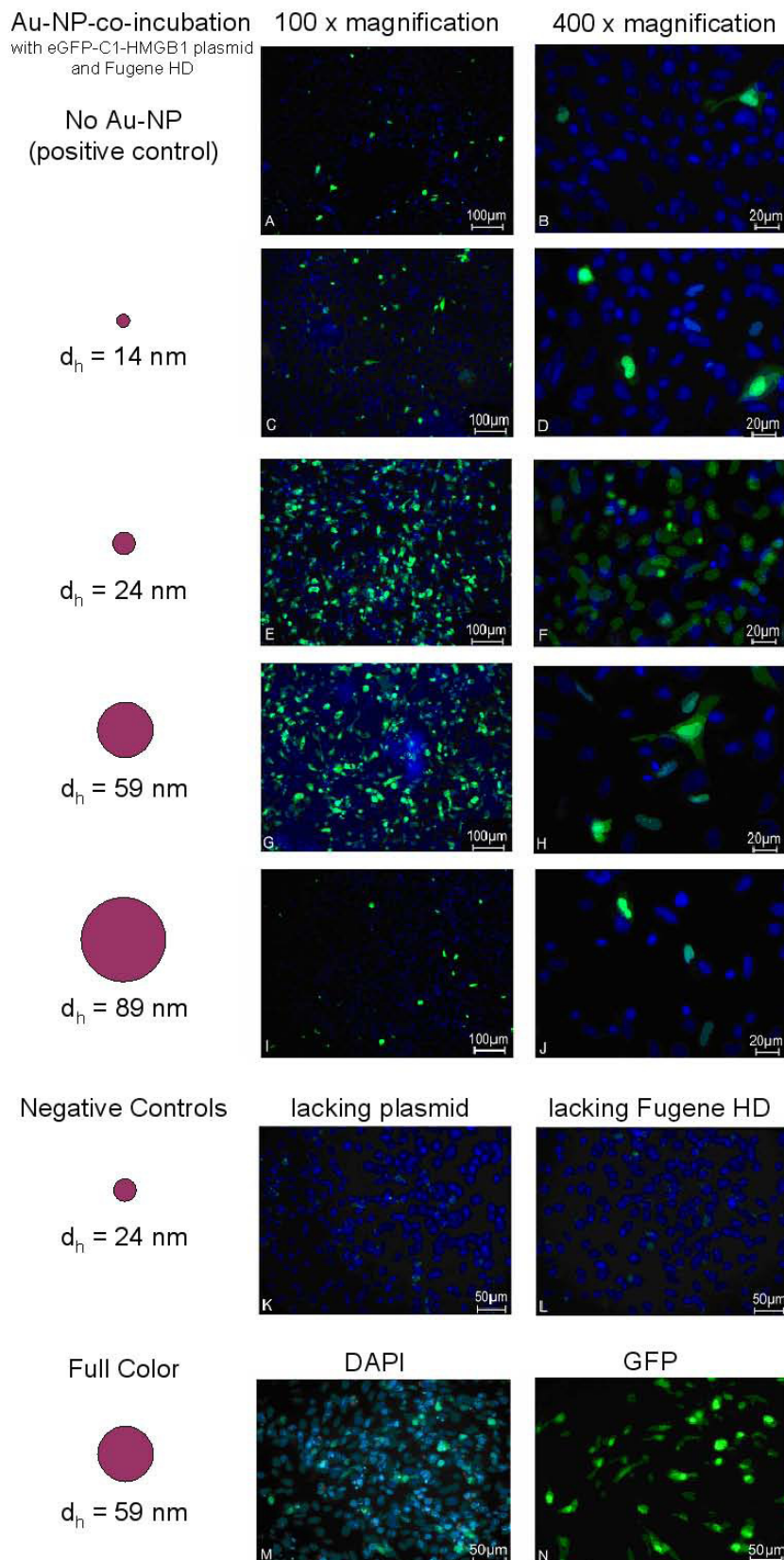
Figure 2.: The effect of co-transfecting plasmid DNA and laser generated gold nanoparticles on the bioactivity of GFP-HMGB1 fusion protein. Images A to I (vertical) show a 100 fold magnification and B to J (vertical) a 400 fold magnification. Images A and B represent the positive control I: a transient transfection of MTH53a cells by Fugene HD reagent with the eGFP-C1-HMGB1 plasmid without Au-NP incubation. Cells in images C to J are treated like control I but include incubation of the plasmid with 14 nanometer-sized Au-NP (C and D), 24 -nanometer-sized Au-NP (E and F), 59 -nanometer-sized nanoparticles (G and H) and 89 -nanometer-sized Au-NP (I and J), respectively. Image K and L represent the negative controls II and III. M and N are full color images of DAPI and GFP fluorescence.

The obtained PCR products were separated on a 1.5 % agarose gel, recovered with QIAquick Gel Extraction Kit (QIAGEN, Hilden, Germany), cloned into the pEGFP-C1 vector plasmid (BD Bioscience Clontech), and sequenced. Twelve hours prior to transfection, 3×10^5 cells from canine mammary cell line MTH53a were seeded into 12 multi well plates. The cells were grown at 37 °C and 5 % CO_2 in medium 199 (Invitrogen, Karlsruhe, Germany) supplemented with 20 % FCS, penicillin, and streptomycin. For transfection, 3 µl aliquots of Fugene HD (FHD) reagent (Roche, Mannheim, Germany) were added to 47 µl of different Au-NP/eGFP-C1-HMGB1 plasmid suspensions in a total volume of 50 µl and incubated for 15 min. The three control sample sets were: (i) 1 µg of eGFP-C1-HMGB1 DNA without nanoparticles, (ii) 250 ng of Au-NPs without any plasmid DNA, and (iii) a set of Au-NPs with DNA, but without the FHD. Following 15 min incubation at 23 °C, the respective 50 µl transfection mixtures were added to cell cultures. The cells were incubated for 48 h in medium 199 (20 % FCS) at 37 °C and 5 % CO_2. The uptake of plasmid DNA and expression of the eGFP-C1-HMGB1 fusion protein were verified by fluorescence microscopy. All experiments were performed in quadruples.

Fluorescence microscopy
Transfected cells were washed with PBS, fixed in a 4 % paraformaldehyde/PBS solution (pH 7.5) for 30 min at room temperature and washed again with PBS. Afterwards, the cells were incubated with 10 µl of mounting medium containing DAPI (4',6-diamidino-2-phenylindole) for fluorescent visualization of nucleic DNA (Vecta Laboratories, Burlingame, USA). Fluorescence microscopy was performed using the Carl Zeiss Axioskop 2 and images were recorded with the Axiovision Software. eGFP fluorescence was measured employing wavelength filter set 10 (Carl Zeiss MicroImaging, Göttingen, Germany), while DAPI fluorescence was measured employing wavelength filter set 2 (Figures 2 A to 2 M). Both fluorescence images were taken with a Zeiss 2-channel Axiocam MRm camera. Both images were then merged in a single image. Full color images were taken with a Zeiss Axiocam HRc (Figures 2 M and 2 N). The uptake of plasmid DNA (efficiency of transfection) was estimated taking into account the quantity of cells within an ocular's visual field. Thus the estimation was done comparing the number of cells showing green fluorescence protein expression (green staining) and cells showing blue DAPI fluorescence dye staining.

Co-transfection of plasmid DNA and laser-generated gold nanoparticles
As the HMGB1 protein is a transcription factor, it binds strongly to nuclear DNA. We therefore may assume that cell nuclei containing strong eGFP fluorescence represent successful functional transfection events. All cells transfected with Au-NP-incubated plasmid DNA showed strong colocalized eGFP and DAPI staining (Figure 2), whilst the negative controls, cells treated with Au-NP and FHD (Au-NP of $d_h = 24$ nm), showed no eGFP fluorescence (Figure 2 K). We therefore conclude that co-incubation of Au-NP with the plasmid DNA encoding the recombinant canine HMGB1 neither prevents the mediated uptake of the vector in presence of a transfection reagent nor has any visible effect on the transport and biological functionality of the synthesized fusion proteins. By comparing fluorescence images of the cells co-incubated with the Au-NPs of different sizes and to cells incubated without Au-NPs, we were able to compare transfection efficiencies in each case. We estimate that the achieved efficiency of DNA transfection for the sample containing 14 nm Au-NPs was approximately 15 ± 5 % (Figures 2 C and 2D). The highest observed transfection efficiencies were achieved using 24 nm and 59 nm Au-NPs (50 ± 5 % and 50 ± 10 % respectively, see Figures 2 E to 2 H). Thus, the observed GFP fluorescence of the respective fusion proteins was so intense that it even leaked into the DAPI channel (Figures 2M and 2N respectively for Au-NP of $d_h = 59$ nm). Hence, Au-NPs show size-dependent effects concerning the observed transfection efficiencies (see Table 1). Further negative control samples containing DNA-co-incubated Au-NPs missing FHD, showed no recombinant protein expression, proving that our Au-NPs did not act as transfection reagent themselves. (Figure 2 L). The cell population seems to go along with transfection efficiency, as the observed seeding density was in all wells similar prior to transfection.

Table 1.: Summary of estimated transfection efficiencies. Differently sized Au-NPs were incubated with plasmid DNA and transfected into the canine MTH53a celline.

Size Au-NP (d_h)	Estimated Transfection Efficiency (%)	Figure 2
Positive controls	10 ± 2	A and B
14 nm	15 ± 5	C and D
24 nm	50 ± 5	E and F
59 nm	50 ± 10	G and H
89 nm	8 ± 3	I and J
Negative controls	-	K and L

Shift assay
We performed binding experiments with plasmid DNA (eGFP-C1-HMGB1) and respective Au-NPs of different sizes and with various concentrations. We digested the co-incubated batches with a *NcoI* restriction enzyme (Fermentas, St Leon Rot, Germany) and separated the resulting DNA fragments in a 1.5 % agarose gel. No significant shift alterations could be observed in the DNA mobility pattern. To ensure that this phenomenon is also valid in presence of proteins we added purified HMGB1 protein (Centre for Human Genetics, Bremen, Germany) to the batches. Akin to the DNA mobility pattern of

digested Plasmid DNA and HMGB1 without Au-NPs (lane 2, Figure 3) we could not detect any significant change in the shift pattern (see lanes 3 to 12, Figure 3). Consequently the DNA/Au-NPs complexes serve as substrates for the DNA-bindig protein HMGB1.
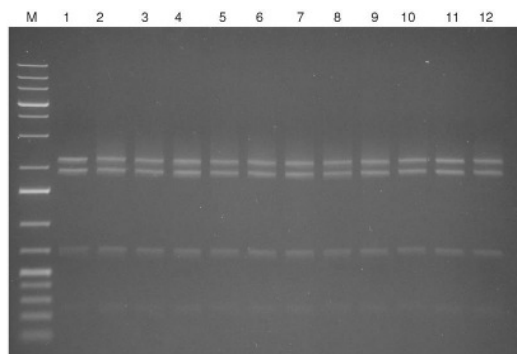

Figure 3.: Au-NPs/DNA and HMGB1 protein mobility shift assay. M: GeneRuler 1 kb Plus (Fermentas), lane 1: 170 ng plasmid (NcoI digested); lane 2: 170 ng plasmid (NcoI digested) and 1.5 µg HMGB1; lanes 3-6: 170 ng plasmid (NcoI digested) and 1.5 µg HMGB1 in 0.1 nM, 0.5 nM, 1.0 nM and 2.5 nM Au-NPs suspensions, size d_h 24 nm; lane 7: 170 ng plasmid (NcoI) digested and 1.5 µg HMGB1 and 90 ng pure Au suspension, size d_h 24 nm; lanes 8-11: 170 ng plasmid (NcoI digested) and 1.5 µg HMGB1 in 0.1 nM, 0.5 nM, 1.0 nM and 2.5 nM Au-NPs suspensions, size d_h 59 nm; lane 12: 170 ng plasmid (NcoI) digested and 1.5 µg HMGB1 and 50 ng pure Au suspension, size d_h 59 nm.

Conclusion

In conclusion, incubation of uncoated, positively charged Au-NPs with a DNA plasmid that encodes recombinant eGFP-C1-HMGB1 fusion protein for 24 hours before cellular transfection does not seem to alter the protein expression and the protein functionality (DNA binding), while the presence of Au-NPs seems to have a significantly positive effect on the transfection efficiencies. The observed effect was size-dependent: medium sized Au-NPs enhanced transfection efficiency nearly 6 fold. These results support the hypothesis that laser-generated Au-NPs present a good alternative to chemically synthesized nanoparticles and are especially suitable for biomedical applications.

Competing interests

The authors declare that they have no competing interests.

Authors' contributions

SP carried out the nanoparticle generation and partial drafting of the manuskript, JTS carried out the transfections, fluorescence microscopy analysis and partial drafting of the manuscript, SW performed cell culture and DNA preparation, AR generated the recombinant eGFPC1- HMB1 plasmid, SB principal study design, manuscript drafting and supervision of nanoparticle work, HME principal design, partial manuscript drafting and supervision of molecular and cell biologic work. IN and JB participated in the conception

design of the study. All authors read and approved the final manuscript.

References

[1] J. Chen, F. Saeki, B.J. Wiley, H. Chang, M.J. Cobb, Z.Y. Li, L. Au, H. Zhang, M.B. Kimmey, X. Li, and Y. Xia. *Nano Letters.* 5:473-477, 2005.

[2] J. Chen, B.J. Wiley, D. Campbell, F. Saeki, L. Cahng, L. Au, J. Lee, X. Li, and Y. Xia Y. *Advanced Materials.* 17:2255-2261, 2005.

[3] P.H. Yang, X. Sun, J.F. Chiu, H. Sun, and H. Qing-Yu. *Bioconjugate Chemistry.* 16:494-496, 2005

[4] G.L. Liu, Y. Yin, S. Kunchakarra, B. Mukherjee, D. Gerion, S.D. Jett, D.G. Bear, J.W. Gray, A.P. Alivisatos, L.P. Lee, and F.F. Chen. *Nature Nanotechnology.* 1:47-52, 2006.

[5] J.A. Dahl, B.L.S. Maddux, and J.E. Hutchison. *Chemical Reviews.* 107:2228-2269, 2007.

[6] F. Mafuné, J. Kohno, Y. Takeda, T. Kondow, and H. Sawabe. *Journal of Physical Chemistry B.* 104:9111-9117, 2000.

[7] F. Mafuné, J. Kohno, Y. Takeda, and T. Kondow. *Journal of Physical Chemistry B.* 105:9050-9056, 2001.

[8] S.I. Dolgaev, A.V. Simakin, V.V. Voronov, G.A. Shafeev, and F. Bozon-Verduraz. *Applied Surface Science.* 186:546-551, 2002.

[9] A.V. Kabashin, and M. Meunier. *Journal of Applied Physics.* 94:7941-7943, 2003.

[10] S. Barcikowski, A. Hahn, A.V. Kabashin, and B.N. Chichkov. *Journal of Applied Physics A.* 87:47-5, 2007.

[11] S. Barcikowski, A. Menéndez-Manjón, B.N. Chichkov, M. Brikas, and G. Raèiukaitis. *Applied Physics Letters.* 91:083113, 2007.

[12] J.P. Sylvestre, A.V. Kabashin, E. Sacher, M. Meunier, and J.H.T. Luong. *Journal of the American Chemical Society.* 126:7176-7177, 2004.

[13] J.P. Sylvestre, S. Poulin, A.V. Kabashin, E. Sacher, M. Meunier, and J.H.T. Luong. *Journal of Physical Chemistry B.* 108:16864-16869, 2004.

[14] A.V. Kabashin, M. Meunier, C. Kingston, and J.H.T. Luong. *Journal of Physical Chemistry B.* 107:4527-4531, 2003.

[15] S. Petersen, J. Jakobi, and S. Barcikowski. *Applied Surface Science.* 255:5435-5438, 2009.

[16] S. Petersen and S. Barcikowski. *Advanced Functional Materials.* 19:1167-1172, 2009.

[17] W. de Jong, and P.J.A. Borm. *Journal of Nanomedicine.* 3:133-149, 2008.

[18] V. Amendola, and M. Meneghetti. *Physical Chemistry Chemical Physics.* 11:3805-3821, 2009.

3.2. Nonendosomal cellular uptake of ligand-free, positively charged gold nanoparticles

Ulrike Taylor, Sabine Klein, Svea Petersen, Wilfried Kues, Stephan Barcikowski, and Detlef Rath

Nonendosomal cellular uptake of ligand-free, positively charged gold nanoparticles

Ulrike Taylor[1†], Sabine Klein[1†], Svea Petersen[2], Wilfried Kues[1], Stephan Barcikowski[2], and Detlef Rath[1]

[1]Institute of Farm Animal Genetics, Friedrich-Loeffler-Institute, Mariensee, Germany
[2] Laser Zentrum Hannover e.V., Hannover, Germany
[†]Equal contributors

Abstract

Gold nanoparticles (GNPs) have interesting optical properties, such as exceptionally high quantum yields and virtually limitless photostability. Therefore, they show the potential for applications as biomarkers especially suitable for *in vivo* and long-term studies. The generation of GNPs using pulsed laser light rather than chemical means provides nanoparticles, which are remarkably stable in a variety of media without the need of stabilizing agents or ligands. This stabilization is achieved by partial oxidation of the gold surface resulting in positively charged GNPs. However, little is known about cellular uptake of such ligand-free nanoparticles, their intracellular fate, or cell viability after nanoparticle contact. The current work is aimed to explore the response of a bovine cell line to GNP exposure mainly using laser scanning confocal microscopy (LSCM) supported by other techniques. Cultured bovine immortalized cells (GM7373) were co-incubated with GNP (average diameter 15 nm, 50 µM Au) for 2, 24, and 48 h. The detection of GNP-associated light scattering by the LSCM facilitated a clear distinction between GNP-containing cells and the negative controls. After 48 h, 75 % of cells had visibly incorporated nanoparticles. No colocalization was detected with either Rab5a or Lamp1-positive structures, i.e., endosomes or lysosomes, respectivley. However, transmission electron microscope analysis of GNP-co-incubated cells indicated that the nanoparticles to be positioned within electron-dense structures. Co-incubation at 4 °C did not inhibit nanoparticle uptake, suggesting diffusion as possible entrance mechanism. Although the assessment of cell morphology, membrane integrity, and apoptosis revealed no GNP-related loss of cell viability, a cytotoxic effect was observed in a proliferation assay after exposing low cell numbers to 50 µM Au and above. In conclusion, this study confirmed the cellular uptake of ligand-free gold nanoparticles during co-incubation apparently without using endocytic pathways.

Introduction

The visualization and quantification of functional and structural cellular aspects using fluorochromes as biomarkers in conjunction with fluorescence microscopy and flow cytometry has become an indispensable asset for all life sciences. Despite tremendous developments in the field of fluorescent dyes, certain disadvantages such as photobleaching have yet not been overcome. In the last decade, a new generation of biomarkers has emerged in the form of quantum dots [1,2] and metal, especially gold nanoparticles (GNPs) [3,4]. Neither is limited by photobleaching anymore, offers a significantly higher quantum yield than conventional fluorochromes and is easily conjugated with functional molecules. Although quantum dots are detected using their photoluminescence, which produces red-shifted emission, the situation is different for metal nanoparticles. Their emitted light is not red-shifted, but has the same wavelength as the light used for excitation, because it is merely scattered by the nanoparticles. The light scattering is caused by the surface plasmon resonance (SPR) of the nanoparticles, whereat a cloud of free electrons on the surface of spherical nanoparticles oscillates in response to an electromagnetic field, which is created around them upon light exposition [5]. In case of gold, the maximum oscillation and, hence, the maximum scattering can be achieved using a wavelength of 520 nm. The light scattering illuminates the particles so brightly that they become visible to light microscopic detection systems, whose resolution would usually be insufficient to pick up particles that small. However, the SPR-caused light scattering maximum is accompanied by an absorption maximum at the same or a very similar wavelength [6]. Whether scattering or absorption prevails depends mainly on nanoparticle size and shape [7]. This leads to the phenomenon that single GNP with a diameter below 20 nm cannot be picked up anymore by light microscopical means, because their SPR enhances only the absorption of light, but not the scattering. The described optical properties of metal nanoparticles make their application as biomarkers a challenge, but also offer the opportunity of tuning the GNP exactly according to the required needs. To perform *in vivo* labeling of intracellular structures using nanoparticles, it is necessary to understand their cellular uptake and intracellular fate. Previous studies have reported the internalization of chemically derived gold nanoparticles into several cell lines within 48 h or less, presuming or proving an endosomatic localization for the incorporated particles [8–11]. The latter raises the problem of transporting the particles into the cytosol to gain access to the location of interest. Another point of considerable interest is the impact of GNPs on cell viability. This is especially important concerning long-term and *in vivo* studies, for which they are particularly suitable due to their resis-

tance to photobleaching and their very high photon efficiency and therefore low excitation power. Although the potential of quantum dots to be harmful has been rather controversially discussed [12,13], the effect of metal nanoparticles differs greatly depending on the metal used for their generation. In case of gold, evidence for toxicity is so far comparatively low [14]. A severe increase in cell death has only been observed in particles of a diameter of 1.4 and 1.2 nm, which can be regarded as gold atom clusters rather than nanoparticles [15]. However, a low-level toxicity was reported in several cell lines after using nanoparticles of various sizes and in different concentrations [9,10,16]. Most toxicity studies as yet have used chemically generated GNPs, which need a surface coating to avoid aggregation or are conjugated to ligands like residual reduction agents and additives. Therefore, it remains unclear whether the noted toxicity, if any, is due to remnants of the chemical agent used for their generation or to the surface coating or indeed to the nanoparticles. The study at hand was designed to investigate the suitability of gold nanoparticles produced by laser ablation [17] as biomarkers because they show several advantages. Compared with chemically produced GNP, laser ablation creates particles, which remain stable in solution without the need for surface coating [18]. Their potential to be harmful might thus be significantly lower. Furthermore, laser ablation in liquids allows via one-step process the design of pure nanomarkers consisting only of the nanoparticle and the functional molecular groups [19].
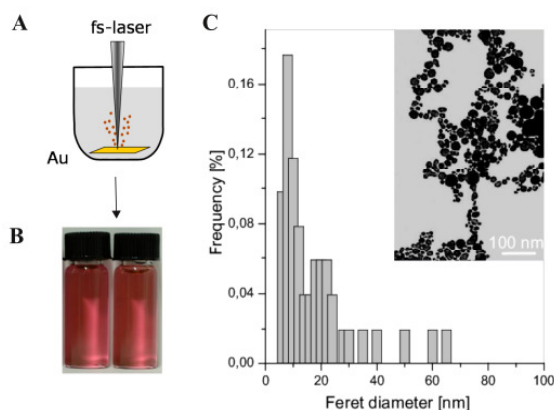

Figure 1.: (A) Laser-based nanoparticle production; (B) colloidal gold nanoparticle dispersions; (C) size distribution of gold nanoparticles derived from laser ablation in water, calculated from 500 nanoparticles observed in TEM micrographs as depicted in the insert.

At first, GNPs were visualized by LSCM outside a cellular system ("bare" GNPs) to facilitate the development of appropriate detection parameters. Subsequently, GNPs were co-incubated with the cells of a bovine-immortalized cell line to study the optical behavior of the laser-generated GNPs once they are cell-associated and to examine their cellular uptake, intracellular fate, and

impact on cell viability. TEM, fluorescence activated cell sorting (FACS) analyses as well as immunohistochemical and colorimetric assays were used to corroborate the results obtained by the LSCM-studies.

Materials and methods
Generation and characterization of gold nanoparticles
The applied laser-based approach to nanoparticles consists in the ablation of a target in liquid media by intense laser radiation, leading to an ejection of its constituent and the formation of a colloidal nanoparticle solution [20,21]. In the study at hand, GNP were generated using a femtosecond laser system (Spitfire Pro, Spectra-Physics) delivering 120 fs laser pulses at a wavelength of 800 nm (maximum energy: 400 µJ per pulse, beam diameter: 4 mm), as recently reported in detail [19]. The pulse energy was fixed to 200 µJ at a repetition rate of 5 kHz. The principle set-up is as follows: The laser beam was focused on a 5x5 mm gold foil (99.99 % purity), thoroughly cleaned and placed at the bottom of a Petri dish filled with 4 ml bi-distilled water (Figure 1 A). The plate was placed on an axis-system that moved at a constant speed of 1 mm/s in a spiral with outer radius of 2 mm and inner radius of 0.4 mm. Time of irradiation was fixed to 12 min corresponding to three spirals. The resulting colloid (Figure 1B) was characterized by UV-Vis spectroscopy (Shimadzu 1650, Shimadzu Europe GmbH, Duisburg, Germany) and TEM (EM 10 C electron microscope, Zeiss, Oberkochen, Germany). Five hundred nanoparticles were counted for the determination of the average Feret diameter (Figure 1 C). The GNP concentration was estimated by weighing (Sartorius M3P-000V001, Sartorius AG, Göttingen, Germany) the gold foil three times before and after laser ablation with an accuracy of 1 µg.

Preparation of GNP dispersions for LSCM-analysis
For the analysis of laser-generated gold nanoparticles outside a cellular system 0.5 µl of the GNP dispersion were pipetted onto a cushion of 5 µl silicon oil (Serva Electrophoresis GmbH, Heidelberg, Germany) resting within a paper reinforcement ring on a microscopic slide. A cover slip was placed on top and sealed with transparent nail varnish.

Cell culture and preparation
Cell culture. Cells used in the co-incubation studies were derived from a bovine-immortalized endothelial cell line (GM7373 [22], obtained from the Cell Culture Collection, Institute of Infectology, FLI, Insel Riems, Germany). To determine the intracellular localization of the internalized GNPs, colocalization trials were performed using GM7373 cells transduced according to manufacturers instructions with Organelle Lights[TM] Reagent (Invitrogen, Karlsruhe, Germany) for endosomes (Rab5a/enhanced green fluorescent

Protein [eGFP]-construct) and lysosomes (LAMP1/eGFP-construct). Thereby endosomes and lysosomes were detected due to eGFP-fluorescence without the need of further staining [23,24]. Cells were generally grown in Dulbecco's modified Eagle's medium (PAA Laboratories GmbH, Pasching, Austria) supplemented with 10 % heat-inactivated fetal bovine serum (Invitrogen, Karlsruhe, Germany) and 1 % penicillin/streptomycin (PAA Laboratories GmbH, Pasching, Austria). Except for the trials testing for nanoparticle diffusion, which were carried out at 4 °C, incubation took place at 37 °C in a humidified 5 % CO_2 atmosphere. Most experiments were carried out in 6-well-dishes (TPP AG, Trasadingen, Switzerland). In experiments concerning apoptosis and cell proliferation, 24-well (Nunc A/S, Roskilde, Danmark) and 96-well-dishes (Greiner bio-one GmbH, Frickenhausen, Germany) were used, respectively. Cells were seeded at a density 5×10^5 cell/ml. Only for proliferation studies, seeding density was lowered to 5×10^4 cells/ml as requested by manufacturers instructions. For LSCM and FACS studies, cells were detached after treatment using a trypsin-EDTA solution (PAA Laboratories GmbH, Pasching, Austria) and collected together with their supernatants. Following trypsinization cells intended for flow cytometry were used immediately as described below or fixed for LSCM as outlined in the following paragraphs. For TEM studies as well as the apoptosis and cell proliferation assay, cells remained in the dishes and were treated as described below.

Cell preparation for LSCM-analysis. Cells determined for evaluation at the LSCM were resuspended after trypsinization in ice-cold Dulbecco's Phosphate-buffered Saline (PBS; Sigma-Aldrich Chemie GmbH, Steinheim, Germany) containing 0.5 % paraformaldehyde (Merck KGaA, Darmstadt, Germany) and fixed for 1 h at 4 °C, then incubated in 0.5 % Tween 20 (Karl Roth GmbH&Co. KG, Karlsruhe, Germany) in PBS for 15 min at 37 °C and after a final wash resuspended in 1 ml of PBS. Thus, the prepared cells were mixed with 1:4 Vectashield (Vector Laboratories Inc., Burlingame, USA) and mounted on a slide within a paper reinforcement ring, in order not to flatten the cells by the subsequently placed cover slip, which was fixed onto the slide with nail varnish.

Cell preparation for TEM analysis. For TEM examinations, cultured cells were fixed to the bottom of six-well-dishes by 2 ml of 2 % glutaraldehyde in PBS in which they remained at 4 °C until further processing. Thus, the fixed cells were prepared for electron microscopy essentially as previously described [25] with slight modifications. Briefly, the cell culture was rinsed in 0.1 M cacodylate buffer (pH 7.4), then post-fixed in 1 % (v/v) osmium tetroxide, rinsed again in cacodylate buffer, dehydrated with increasing concentrations of ethanol, and subsequently embedded in Epon. The prepared cell layer was trimmed and processed for standard transmission ultrastructural examination.

GNP co-incubation assays. Co-incubation assays to determine nanoparticle penetration were performed using GNPs in a final concentration of 50 µM Au. After seeding, cells were allowed to attach and then exposed to the nanoparticles for 2, 24, and 48 h. Cells incubated in medium alone for 48 h were used as controls. For trials concerning GNP diffusion, exposure time was chosen to be 6 h in order not to exceed the length of time cells remain viable at 4 °C in a non- CO_2-enriched atmosphere. All experiments were carried out in duplicates and repeated five times. To calculate the percentage of cells with incorporated GNP, 100 cells/treatment group were counted on LSCM-images taken as described later.

Viability tests
All GNP co-incubation trials performed in order to test for cell viability were repeated at least three times.

Assessment of cellular morphology. Morphology of the attached cells was judged subjectively under an inverted cell culture microscope (Leica DMIRB; Leica, Wetzlar, Germany) equipped with a camera (Canon Powershot G5). Assessment was carried out directly before and after nanoparticle exposure (50 µM Au) for 2, 24, 48, and 96 h using a 200x magnification.

Flow cytometric determination of membrane integrity. Treated cells (50 µM Au; 2, 24, 48, and 96 h) and controls were collected immediately after trypsinization as described earlier. After diluting the cells in PBS to 0.5×10^6/ml, propidium iodide (Invitrogen, Karlsruhe, Germany) was added to a final concentration of 22.5 µM. Flow cytometric analysis was performed using a FACScan (BD Bioscience, Heidelberg, Germany) equipped with an argon laser (488 nm, 15 mW). Samples were always analyzed in duplicates acquiring 10,000 cells per measurement.

Determination of membrane integrity using a LSCM. To relate cell viability to their nanoparticle content, membrane integrity was additionally studied after 48 h GNP exposure (50 µM Au) using the LSCM. For that purpose, the LIVE/DEAD Fixable Far Red Dead Cell Stain Kit (Invitrogen, Karlsruhe, Germany) was chosen because it provided a fixable staining of membrane-compromised cells to be visualized in a spectrum easy to distinguish from the GNP light scattering. The dye was used according to manufacturer's instructions. After staining cell preparation for the LSCM proceeded as described above.

Table 1.: Configuration for surface plasmon resonance detection of GNPs as well as eGFP and far red fluorescence (LSM510; Carl Zeiss MicroImaging GmbH, Jena, Germany)

Laserwavelengths	Main beam splitter	Detection band pass	Detection channel	Excited Labels
488	488/543/633	505–530	3	eGFP
543	80/20	530–570	2	GNP
633	488/543/633	>650	1	LIVE/DEAD1 Fixable Far Red Dead Cell Stain
633	488/543/633	488/543/633	Transmission	Differential interference contrast (DIC)

Immunohistochemical determination of apoptosis. For the detection of apoptosis, the TUNEL (terminal deoxynucleotidyl transferase mediated dUTP nick end-labeling) technique, which focuses on visualizing the cleavage of DNA typical for apoptotic cells, was applied using the *In Situ* Cell Death Detection Kit, POD (Roche, Penzberg, Germany). The test was performed according to manufacturer's instruction.

Additionally, to a treatment group (50 µM Au, 96 h) and a mediumalone control group, a negative and positive control group were run, where DNA strand breaks were artificially introduced by pretreatment with DNase I (50 U/ml; Epicentre Biotechnologies, Madison, USA) for 10 min at room temperature. After DNase incubation, positive controls were exposed to the complete TUNEL reaction mixture, while negative controls were incubated in labeling solution in the absence of the enzyme terminal transferase. For evaluation, cells were observed at 400x magnification using the same equipment as described earlier for the assessment of cell morphology.

Colorimetric determination of cell proliferation. Cell proliferation after treatment with gold nanoparticles was investigated using the PromoKine Cell Viability Kit III, XTT (PromoCell GmbH, Heidelberg, Germany), which assesses the conversion of the tetrazolium salt XTT into colored formazan compounds by viable cells, i.e., indirectly measures cell numbers. The tests were carried out as recommended by the manufacturer. After 24 h of co-incubation with varying amounts of nanoparticles (1.25, 2.5, 5, 10, 25, 50, and 100 µM), cells were subsequently incubated for another 4 h with the reaction solution. Afterwards, the absorbance of the samples was measured with a spectrophotometer (Tecan Spectra II; Tecan Group Ltd., Maennedorf, Switzerland) at 450 nm.

Imaging
Laser scanning confocal microscopy. Light microscopical visualization had been performed using an Axioplan 200 and a confocal imaging system LSM510 (Carl Zeiss MicroImaging GmbH, Jena, Germany) within the spectrum of visible light. A Helium-Neon-Green laser of 543 nm was used to excite the surface plasmon

resonance of the gold nanoparticles in dispersion and in cultured bovine cells. Fluorescence of eGFP was excited with an Argon laser at 488 nm, and the Fixable Far Red Stain was visualized after excitation at 633 nm with a Helium-Neon-Red laser. Visualization of the light scattering for each of the excitation wavelengths was recorded in multitracking mode using separate detection channels. Complete configurations are summarized in Table 1.

Transmission electron microscopy. Ultrathin sections were stained with uranylacetate and lead citrate and examined with an EM 10 C electron microscope (Carl Zeiss AG, Oberkochen, Germany).

Statistics
All statistical analyses were carried out with the program SigmaStat (Version 3.0, StatCon, Witzenhausen, Germany). The proportion of GNP positive cells after 2, 24, and 48 h of incubation were tested by ANOVA and Holm-Sidak all pairwise significance test ($P<0.05$). The results of the flow cytometric studies for the determination of toxic effects were analyzed using ANOVA and the Bonferroni test.

Results
Visualization of ''bare'' gold nanoparticles by LSCM
Before the characterization of the GNPs in cellular environment, gold nanoparticles were investigated in dispersion. Figure 2 shows representative laser scanning microscope images taken of a volume of about 10 pl (31.3 x 31.3 x 10.21 µm) containing colloidal GNPs (250 µM Au) dispersed in deionized water using the configurations as described in Table 1. The SPR was excited at a wavelength of 543 nm. Repeated examination of single slides even after long-term exposure to light did not detect any sign of photobleaching.

Cellular uptake and subcellular localization of gold nanoparticles as visualized by LSCM
The configurations of LSCM as determined using the ''bare'' gold nanoparticles facilitated a clear distinction between GNP-containing co-incubated cells and the negative controls (Figures 3 A–D).
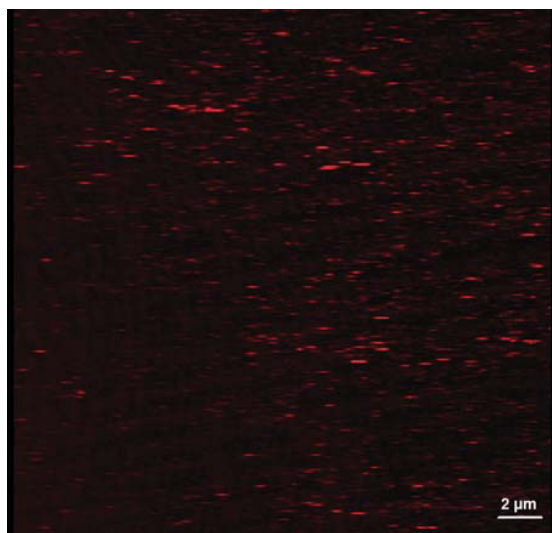
Figure 2.: Representative laser scanning microscope image (3D projection of the optical stack) of colloidal GNPs (250 µM Au, particles size as described in Figure 1) dispersed in deionized water. GNPs appear in red (channel 2, Table 1).

It also confirmed that the GNPs were positioned intracellular and not cell membrane-associated. Cells incorporated the GNPs in a time dependent manner (Figure 3 E). After an incubation period of 2, 24, and 48 h $44.1 \pm 6.4\%$, $59.9 \pm 5.6\%$ and 77.4 ± 3.9 of cells proved to be GNP positive, respectively. Colocalization studies using cells transduced with endosome and lysosome eGFP-protein-marker constructs revealed that signals derived from GNP did colocalize neither with Rab5a-positive endosomes nor LAMP1-positive lysosomes (Figures 4 A and B). Co-incubation trials of GM7373 cells with GNPs at $4\,°C$, where active uptake processes by endocytotic pathways are diminished nevertheless showed a considerable amount of nanoparticles inside the cells (Figure 4 B).

Cellular gold nanoparticle uptake and subcellular localization as visualized by TEM
Gold nanoparticles were located in the cytosol surrounded by lysosomal-like structures (Figure 5). The particles were observed singly (Figure 5 A) or in small cluster (Figure 5 B). In terms of size, the observed nanoparticles varied between 5 and 70 nm (Figure 5 B), corresponding to the initial GNP size (Figure 1).

Viability of cells after gold nanoparticle uptake
Assessment of cellular morphology. Microscopic examination of treated cells did not indicate any decrease in viability. Cell morphology was not altered, compared with controls after up to 96 h of nanoparticle exposure (Figure 6 A).
Flowcytometric determination of membrane integrity. Loss of membrane integrity, an indicator for cell death by necrosis, was determined after exposing cells to GNP (50 µM Au) for 2, 24, 48, and 96 h. To quantify the percentage of cells with an impaired outer membrane, the intracellu-
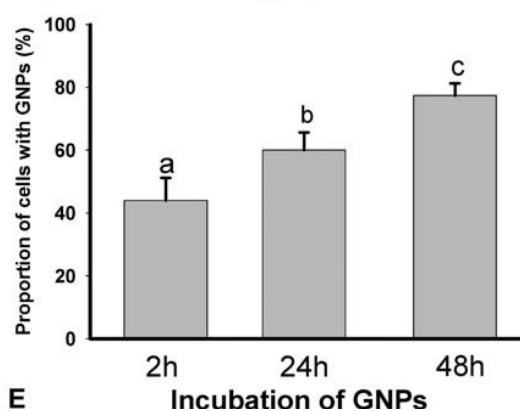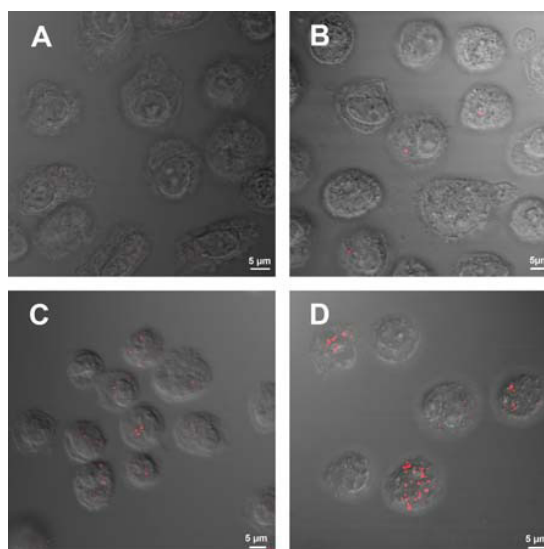

Figure 3.: Representative laser scanning microscope images of bovine endothelial cells (GM7373) (3D-projections of 10 optical sections (1 µm each)) after co-incubation with GNPs (50 µM Au): (A) negative controls, co-incubated for 48 h in medium; (B) 2 h; (C) 24 h; (D) 48 h of co-incubation with GNPs, respectively. GNPs appear in red. An overlay of the differential interference contrast (DIC) merged with the detection channel 2 is shown (Table 1). The diagram indicates the time-dependent uptake of GNPs. Values are means ± standard deviation (SD). Different letters represent significant differences between the treatment groups (P<0.05).

lar uptake of propidium iodide was measured. After 96 h of treatment, no significant increase of PI positive cells was detected compared with controls (Table 2).
Determination of membrane integrity using a LSCM. The staining of necrotic cells with the Far Red Fluorescent Reactive Dye provided the opportunity to image cellular GNP load in conjunction with the integrity of the outer membrane in one and the same cell (Figure 6 B). Confirming the results of the flow cytometric analysis, the vast majority of cells did not indicate any loss of membrane integrity, while the rare, membrane damaged cells did not show a particular accumulation of GNPs.
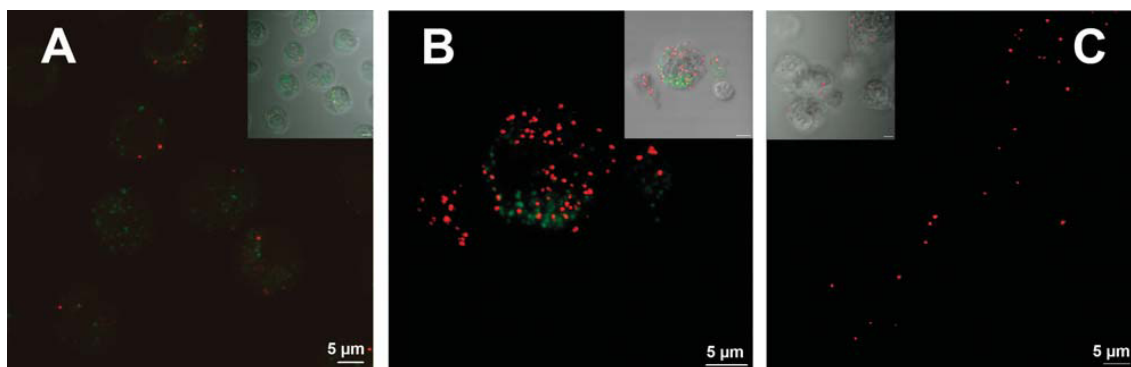
Figure 4.: Representative laser scanning microscope images of bovine endothelial cells (GM7373) transduced with endosome [Rab5a, (A)] and lysosome [LAMP1, (B)] eGFP-protein-marker constructs after co-incubation with GNPs (50 µM Au) for 2 h (endosomes) or 48 h (lysosomes). (C) Wild type cells after co-incubation with GNPs (50 µM Au) for 6 h at 4 °C. GNPs appear in red (channel 2), endosomes and lysosomes in green (channel 3; Table 1). The inserts include additionally the overlay of the DIC.

Immunohistochemical determination of apoptosis. Apoptosis is a cellular program for cell death, which may become activated under adverse or harmful conditions. A hallmark of apoptosis is massive fragmentation of nuclear DNA, which can be assessed by the TUNEL assay. Here, GM7373 cultures, exposed to GNP (50 µM) for 96 h as well as the medium-alone controls, showed rarely apoptotic cells (Figure 6 A), suggesting that the used GNP did not activate apoptotic signaling pathways.

Colorimetric determination of cell proliferation. For the assessment of proliferation, cells were seeded at low density and exposed to nanoparticles during the logarithmic growth phase. Both factors cause cells to be especially sensitive toward cytotoxic compounds. In this case, the cells showed a complete arrest in growth if exposed to GNP in a concentration of 100 µM Au (Figure 6 C). Half of that dose still led to a reduction of proliferation to 46 %. Microscopic examination revealed that at both concentrations cells were rounded and had lost cell-to-cell and cell-to-dish contact. However, a concentration of 25 µM Au and lower did not lead to a detectable drop in proliferation or to a nonphysiological cell morphology.
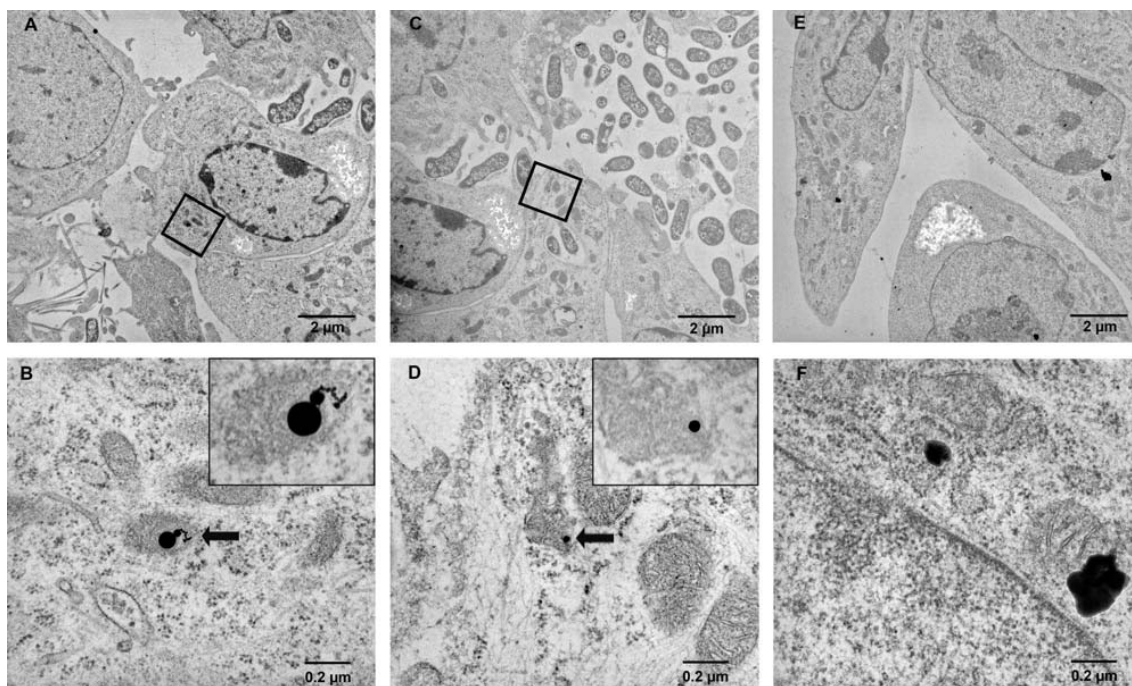
Figure 5.: Representative transmission electron microscope images of bovine endothelial cells (GM7373) co-incubated with GNPs (50 µM Au) for 48 h (A—D) and negative controls (E, F). A, C, and E: 36300 magnification, in A and C with squares pointing out the area depicted in B and D; B, D and F: 350,000 magnification, in case of B and D with arrows pointing to GNPs (B, group of approximately 10 GNPs varying between 5 and 65 nm in size; C, single GNP) and inserts depicting the area of interest in 3100,000 magnification. The pictures of negative controls (E, F) in two magnifications where included, to show that a clear distinction between nanoparticles and artefacts was only possible in a magnification of 350,000 and above.

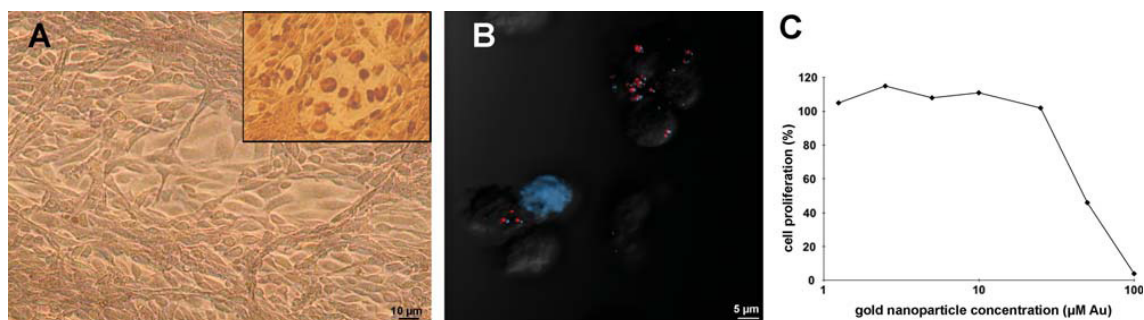**Figure 6.:** Representative inverted microscope image (3400 magnification) of bovine endothelial cells (GM7373) examined for apoptosis using the TUNEL assay after 96 h co-incubation with GNPs (50 µM Au). The nuclei show no detectable amounts of DNA strand breaks. The cells display normal cell morphology and physiological growth patterns. The insert depicts the positive control. B: Representative laser scanning microscope image of the cells depicted in A after staining with a fixable dye for cells with damaged cell membranes. GNPs appear in red (channel 2), the stain showing off the rare necrotic cells in blue (channel 1, Table 1). The DIC image was merged with the image from the detection channels 1 and 2. C: Diagram displaying the results of the XTT proliferation assay as a percentage of living cells (negative control= 100 %) against the GNP concentration on a logarithmic scale.

Discussion

The purpose of this study was to gain a better understanding of the behavior of charged and ligand-free, laser-generated gold nanoparticles within a cellular environment using mainly laser scanning confocal microscopy. This technique proofed to be a suitable tool for the detection of GNPs once the system had been adjusted to detect the SPR-related light scattering of the nanoparticles. The properties attributed to the nanoparticles regarding their very high quantum yield and utter resistance to photobleaching were found to be highly valuable for light microscopic imaging. The cellular uptake of nanoparticles as measured with the LSCM seemed to increase steadily over time. It has to be considered that this statement can only be made for nanoparticles larger 20 nm. According to literature, only these particles can be detected by light microscopy, as in particles smaller than 20 nm the surface plasmon resonance mostly enhances light absorption, instead of scattering [7]. However, analysis of internalized GNP by TEM, where detection does not depend on SPR-caused light scattering, (Figure 4 B) displayed the entire range of particles included in the co-incubation trials (Figure 1 C). Concerning the mechanisms of GNP uptake and their intracellular fate, previous studies varied in their findings. Authors, who observed nanoparticles placed in acidic organelles [10] or in vesicles [8] presumed an endocytic pathway. In this study, LSCM analysis of GNP co-incubation trials using cells transduced with constructs carrying Rab5a/eGFP and LAMP1/eGFP revealed that the intracellular nanoparticles did not colocalize with the fluorescent protein-tagged organelles (Figures 4 A and 4B). Rab5a is a protein typical for early endosomes, while LAMP1 has been reported to be one of the major components of the lysosomal membrane. The results make it therefore highly unlikely that the gold nanoparticles entered the cells via the endocytic pathway. These findings are supported by the results of the co-incubation studies performed at 4 °C. The fact, that even at such a low temperature

sufficient nanoparticles permeate into the cells within 6 h to be easily detected by LSCM (Figure 4 C) speaks strongly for simple diffusion as the main entering mechanism. Interestingly, the electron microscopic pictures indicated that the majority of GNPs was located in lysosomal-like structures (Figure 5). Possible explanations for this finding might be that once the nanoparticles have entered the cell, their property as electron donor causes an accumulation of molecules around them with electron acceptor moieties, such as proteins, thus forming a structure, which might appear like a lysosome.

Table 2.: Percentage of propidium iodide (PI) positive cells after different periods of GNP-co-incubation

Time of Co-incubation(h)	Percentage of PI positive cells ± SD
Negative control	6.3 ± 1.5
2	6.1 ± 1.8
24	6.7 ± 1.5
48	6.5 ± 0.8
96	5.6 ± 0.6

To investigate the impact of uncoated GNP on cell viability several aspects have been examined: (i) microscopic assessment of cell morphology, (ii) flow cytometric measurement of PI-uptake, and (iii) immunohistochemical evaluation of DNA strand breaks. These methods allowed the examination of large cell numbers and showed no detrimental effect after a co-incubation period of up to 96 h on the overall cell population (Figure 6 A, Table 2). However, the methods mentioned earlier did not permit to distinguish between GNP-carrying and "empty" cells. To correlate the nanoparticle load and cell necrosis, GNP-co-incubated cells were stained with a fixable viability dye and analyzed using the LSCM. Compared to controls, no increase of necrotic cells or an accumulation of GNPs in these few dead cells could be found. Furthermore, a trial studying cell proliferation was carried out. Interestingly, this test picked up cytotoxic effects of gold nanoparticles at a concentration of 50 µM Au, which showed no deleterious

effect in the other experiments concerning cell viability. The most possible reason for this finding might be the difference in cell numbers between the tests. Proliferation tests are conventionally performed with particularly low cell numbers, in this case only with a tenth of the cells used in the other trials. Apparently, in order for the GNPs to act cytotoxic either a very high nanoparticle-to-cell ratio is required or the cells need to be in a particularly vulnerable state, which is the case, if they are highly diluted and in a logarithmic growth phase. Interestingly, the fact, that nanoparticle toxicity seems to depend not only on the actual concentration of the compound, but at least partially, also on the ratio of particle number or, rather, active particle surface to cells, has also been noted for nanoparticles made from other materials [26]. This point should also be observed in further studies. However, no toxic effects were observed at a gold concentration of 25 µM and below, which means that a theoretical ratio (calculated for an average particle size of 15 nm with a weight of 34 ag) of 3×10^6 nanoparticles/cell did not show adverse effects. In conclusion, ligand-free nanoparticles produced by laser ablation seem promising candidates to become a new generation of biomarkers, which certainly seem superior to conventional fluorochromes for *in vivo* studies. They are readily detectable by light microscopy. Due to their high quantum yield, even minute amounts of GNP can be detected. The lack of photobleaching allows long-term studies and easy handling. They enter cells and cytoplasm readily and apparently not via endocytic pathways, but a passive mechanism. Bioconjugation simultaneously to laser ablation allows the easy design of nanomarkers for target detection [19]. Finally, cell viability only seems to be impaired at doses likely to more than exceed the amounts needed for the marking of cellular features. However, due to the complexity and importance of the matter, especially this last point warrants further research.

Acknowledgements

References

[1] D.R. Larson, W.R. Zipfel, R.M. Williams, S.W. Clark, M.P. Bruchez, F.W. Wise, and W.W. Webb. *Science.* 300:1434-1436, 2003.
[2] J.K. Jaiswal, H. Mattoussi, J.M. Mauro, and S.M. Simon. *Nature Biotechnology.* 21:47-51, 2003.
[3] S. Schultz, D.R. Smith, J.J. Mock, and D.A. Schultz. *Proceedings of the National Academy of Science.* 97: 996-1001, 2000.
[4] H.F. Wang, T.B. Huff, D.A. Zweifel, W. He, P.S. Low, A. Wei, and J.X. Cheng. *Proceedings of the National Academy of Science.* 102:15752-15756, 2005.
[5] U. Kreibig, and M. Vollmer. Berlin: Springer; 1995.
[6] S. Link, and M.A. El-Sayed. *Journal of Physical Chemistry B.* 103:4212-4217,1999.
[7] P.K. Jain, S. Eustis, and M.A. El-Sayed. *Journal of Physical Chemistry B.* 110:18243-18253, 2006.
[8] B.D. Chithrani, A.A. Ghazani, and W.C.W. Chan. *Nano Letters.* 6:662-668, 2006.
[9] H.K. Patra, S. Banerjee, U. Chaudhuri, P. Lahiri, and A.K. Dasgupta. *Nanomedicince: Nanotechnology Biology and Medicine.* 3:111-119, 2007.
[10] R. Shukla, V. Bansal, M. Chaudhary, A. Basu, R.R. Bhonde, and M. Sastry. *Langmuir.* 21:10644-10654, 2005.
[11] S.W. Tsai, J.W. Liaw, F.Y. Hsu, Y.Y. Chen, M.J. Lyu, and M.H. Yeh. *Sensors.* 8:6660-6673, 2008.
[12] R. Hardman. *Environmental Health Perspectives.* 114:165-172, 2004.
[13] A. Shiohara, A. Hoshino, K. Hanaki, K. Suzuki, and K. Yamamoto. *Microbiology and Immunology.* 48:669-675, 2004.
[14] N. Lewinski, V. Colvin, and R. Drezek. *Small.* 4:26-49, 2008.
[15] Y. Pan, S. Neuss, A. Leifert, M. Fischler, F. Wen, U. Simon, G. Schmid, W. Brandau, and W. Jahnen-Dechent. *Small.* 3: 1941-1949, 2007.
[16] A.G. Tkachenko, H. Xie, Y.L. Liu, D. Coleman, J. Ryan, W.R. Glomm, M.K. Shipton, S. Franzen, and D.L. Feldheim. *Bioconjugugate Chemistry.*15:482-490, 2004.
[17] S. Barcikowski, A. Menendez-Manjon, B.N. Chichkov, M. Brikas, and G. Raciukaitis. *Applied Physics Letters.* 91:083113, 2007.
[18] S. Barcikowski, A. Hahn, A.V. Kabashin, and B.N. Chichkov. *Applied Physics A.* 87: 47-55, 2007.
[19] S. Petersen, and S. Barcikowski. *Advanced Functional Materials.* 19:1167–1172, 2009.
[20] F. Mafuné, J. Kohno, Y. Takeda, T. Kondow, and H. Sawabe. *Journal of Physical Chemistry B.* 104: 9111-9117, 2000.
[21] A.V. Kabashin, and M. Meunier. *Journal of Applied Physics.* 94:7941-7943, 2003.
[22] J.B. Grinspan, S.N. Mueller, and E.M. Levine. *Journal of Cellular Physiology.* 114:328-338,1983.
[23] R.L. Roberts, M.A. Barbieri, K.M. Pryse, M. Chua, and P.D. Stahl. *Journal of Cell Science.* 112:3667-3675, 1999.
[24] J.M. Falcon-Perez, R. Nazarian, C. Sabatti, and E.C. Dell'Angelica. *Journal of Cell Science.* 118:5243-5255, 2005.
[25] G. Schares, J. Meyer, A. Barwald, F.J. Conraths, R. Riebe, W. Bohne, K. Rohn, and M. Peters. *International Journal of Parasitology* 33:229-234, 2003.
[26] G. Oberdorster. *International Archives of Occupational and Environmental Health.* 74:1-8, 2001.

4.   *In situ* bioconjugation of laser-generated gold nanoparticles with nucleic acids

The ligand-free surface of laser-generated AuNPs, whose influence on biocompatibility and cellular uptake has been investigated in the previous chapter, might provide great opportunities for a rapid and controlled particle functionalization, as detailed in chapter 2.4.4. Functional molecules can be added to the ablation medium prior to the laser process, allowing a simultaneous generation and conjugation of AuNPs. Ultrashort-pulsed lasers represent a promising tool for this *in situ* conjugation, since the thermal impact to both the ablated material (which releases the nanoparticles) and the liquid is minimized. In this context, the following part comprehends three papers dealing with the establishment and characterization of the *in situ* functionalization of AuNPs during femtosecond laser ablation in liquids (fs LAL) with NAs as one important class of bio-molecules. An aqueous solution of thiolated ssO (23 bases) was chosen as a first model ablation medium. However, it has to be noted, that laser-generated AuNPs are stable in aqueous solutions even in the absence of additives (chapter 2.4.3), while they would agglomerate in most unpolar solvents. As consequence, changes in size and optical properties as possible indicators for a successful conjugation are detected more sensitively in alkane solutions compared to water. In order to determine these indicators, we performed preliminary experiments of the *in situ* stabilization of AuNPs with dodecanethiol (DDT) in n-hexane. In this respect, dynamic light scattering (DLS) measurements were carried out to estimate differences in the size distribution of AuNPs generated in different concentrations of DDT. Results reveal that the size and also the dispersity of the distribution are significantly influenced, while especially the particle diameter shows a reciprocal dependency on the DDT concentration (Figure 4.1). We assume that this size quenching effect is one indicator of a successful NP functionalization.

Furthermore, the optical properties are influenced by conjugation. While stabilized (non-aggregated) AuNPs exhibit a sharp SPR around 520 nm, aggregated NPs show a broadened band often shifted to longer wavelengths. In our preliminary tests, we observed exactly this trend: with increasing DDT concentration the SPR maximum shifts towards smaller wavelengths until it reaches a minimum at 3 mM (Figure 4.2). Thus, a second indication of a successful conjugation was found.
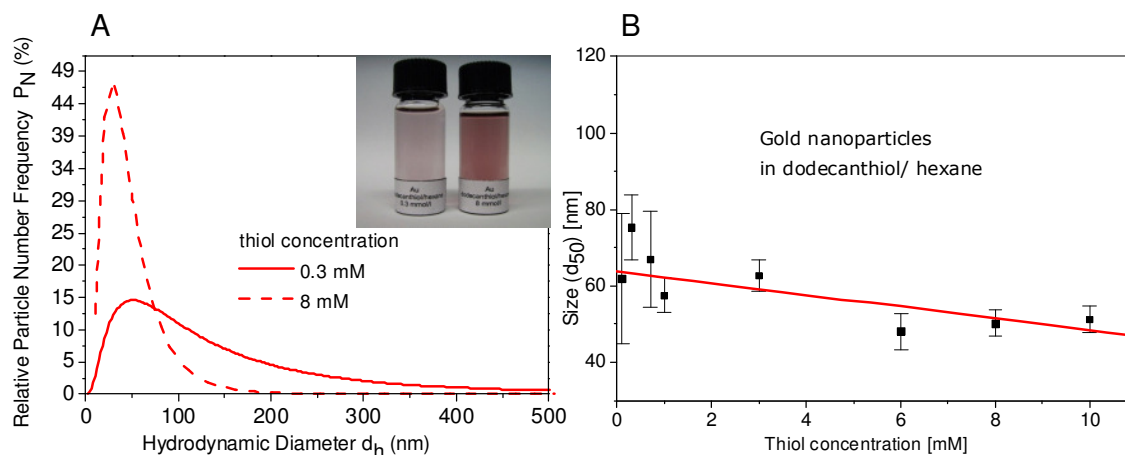
Figure 4.1.: (A) Hydrodynamic size distribution of AuNPs, obtained by laser ablation in 0.3 (Insert left colloid) and 8 mM (Insert right colloid) DDT in n-hexane. (B) Reciprocal dependency of the d_{50}* value on the DDT concentration in the ablation medium. *The d_{50} value, measured by DLS, describes the hydrodynamic diameter that is not exceeded by 50 % of the particles. (Conference proceedings [8])
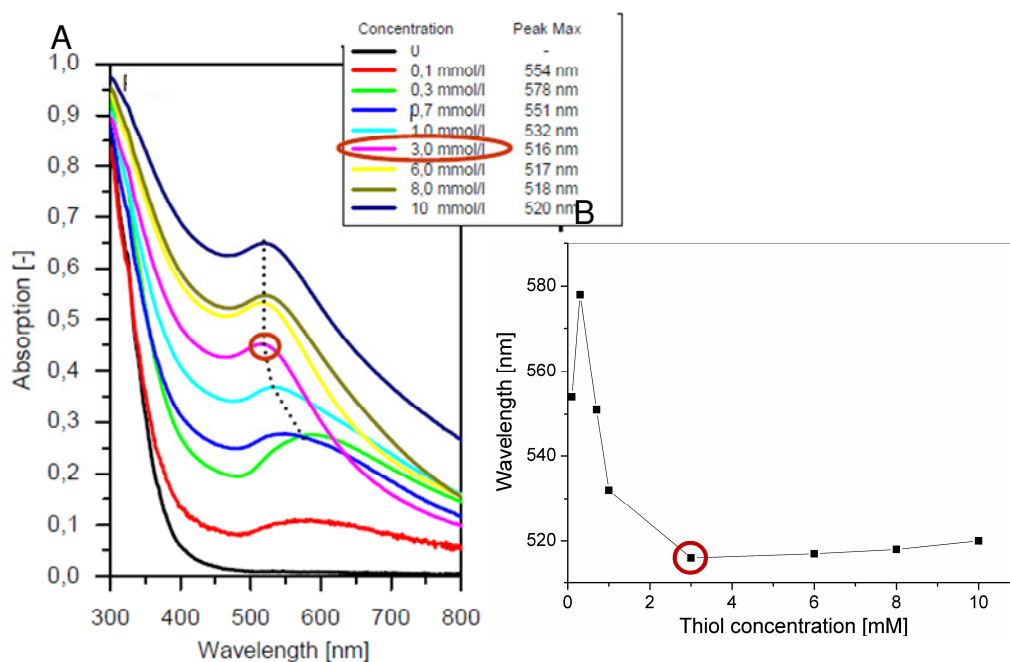

Figure 4.2.: (A) UV-Vis spectra of AuNPs, generated in increasing DDT concentrations. (B) The SPR of laser generated AuNPs is subject to a blue shift with increasing DDT concentrations in the ablation medium. Red circles mark the DDT threshold concentration for AuNP stabilization in hexane. (Conference proceedings [8])

The establishment of the *in situ* bioconjugation with ssO by fs LAL, presented in the first paper in this assembly (chapter 4.1), confirms these findings. However, particularly for the optical properties, the changes due to conjugation were less distinct probably due to the better stabilization in water compared to hexane. Furthermore, a process window with regard to the pyrolysis of ssO as result of interaction with the laser beam

and to NP productivity was determined. We were thus able to synthesize 20 µg of ssO-functionalized AuNPs in less than one minute without provoking degradation of the ssO. Interestingly, nanoparticle productivity seemed to increase with the addition of ssO in comparison to water and also to pure and DDT-containing n-hexane. Assuming that the difference in the optical properties between pure and stabilizing agents containing solutions is negligible, the ablation process itself should not be affected by the ablation media. Therefore, the same amount of gold is supposed to be ablated in both cases. Consequently, without ssO or DDT in solution, we assume that particles redeposit on the target's surface after ablation, when reaching a stabilization limit. This assumption is confirmed by SEM micrographs of a gold target after ablation (Figure 4.3).
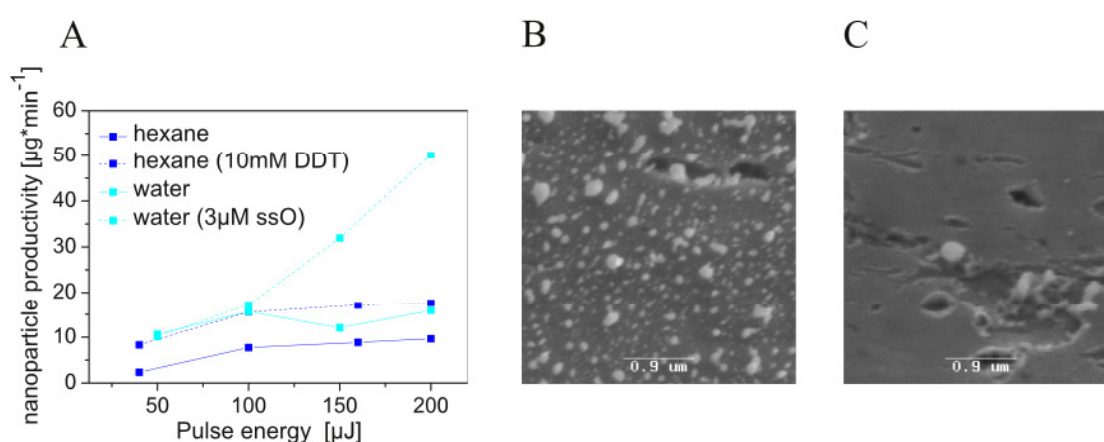

Figure 4.3.: (A) Dependence of nanoparticle productivity after 15 minutes of ablation on the pulse energy in different ablation media and SEM micrographs of redeposits on gold target after ablation at 200 µJ in aqueous media (B) without and (C) with ssO. (Own paper not included in the thesis [5])

Additionally, higher productivities were observed in water compared to n-hexane, irrespective of whether additives are contained or not. For additive-free solutions this might be explained by the electrostatic stabilization of AuNPs in water and for additive-containing solutions, this difference is probably due to the presence of two stabilization modes in water, resulting in electrosterically stabilized AuNPs. This double stabilization proved to be essential for biomedical assays, as it helped to prevent the laser-generated bioconjugates against aggregation in saline solutions, like physiological media.

The second paper (chapter 4.2) deals with the characterization of the conjugation efficiency and the surface coverage of ssO per AuNP, obtained by the laser-based synthesis of bioconjugates *in situ* and *ex situ*, which we assume as a determining parameter for the bioactivity of the bioconjugates. In comparison to conventional NP bioconjugation techniques as the ligand exchange method, five times higher maximal surface coverage values were determined for both laser-based synthesis methods. However,

the strength of the interaction of ssO with AuNPs seems to be higher during *in situ* conjugation, revealed by higher conjugation efficiencies in terms of the percentage of total ssO conjugated to AuNPs. Interestingly, the surface coverage seemed to be tunable by the ssO to AuNP ratio, allowing the fabrication of bioconjugates with varying degrees of bioactivity. To conclude, laser ablation in liquids presents a prospective and efficient preparation method, which we suppose as especially interesting for the conjugation of precious biomolecules like vectors or aptamers.

In this context, the third paper (chapter 4.3) addresses the conjugation of a DNA aptamer directed against streptavidin as a model system. A size quenching, as reported before for DDT and ssO addition to ablation medium, resulted in AuNPs with diameters of approximately 9 nm exhibiting a high surface density of aptamers (approximately 86 pmol/cm^2). While this seems to be nearly the half of the surface coverage obtained with ssO (Figure 4.4), which might be due to the longer or different base sequence of the aptamer, it is still more than the double generally reported in literature.
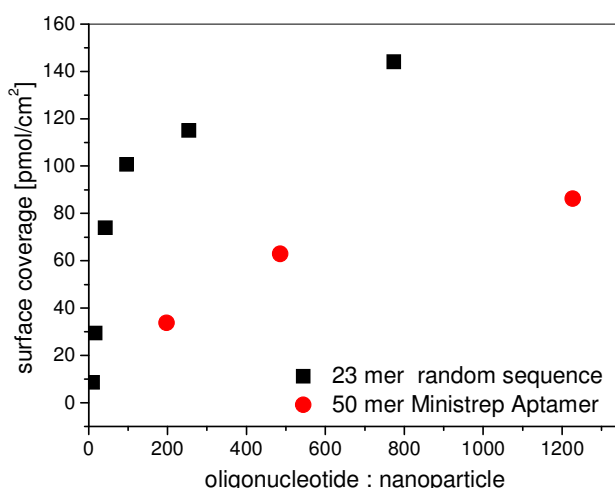

Figure 4.4.: Surface coverage of ssO and aptamer on AuNPs, obtained by *in situ* bioconjugation during laser ablation.

Moreover, an unlimited activity (approximately 100 %) of the immobilized aptamers was demonstrated by three independent methods, including agglomeration-based assays and solid-phase assays. To examine the general applicability of the *in situ* conjugation of AuNPs with aptamers, the approach was transferred to an RNA aptamer directed against prostate specific membrane antigen (PSMA). Successful detection of PSMA in human prostate cancer tissue, utilizing tissue microarrays, evidences the activity of the immobilized aptamer and confirms the universality of the laser-based bioconjugation of AuNPs with NAs.

4.1. *In situ* bioconjugation - Single step approach to tailored nanoparticle bioconjugates by ultrashort-pulsed laser ablation

Svea Petersen and Stephan Barcikowski

4.2.   Conjugation efficiency of the laser-based bioconjugation of gold nanoparticles with nucleic acids

Svea Petersen and Stephan Barcikowski

Journal of Physical Chemistry C. 113:19830-19835, 2009

Conjugation efficiency of laser-based bioconjugation of gold nanoparticles with nucleic acids

Svea Petersen and Stephan Barcikowski

Laser Zentrum Hannover e.V., Hannover, Germany

Abstract

Ultrashort-pulsed laser ablation represents a powerful tool for the generation of pure gold nanoparticles avoiding chemical precursors, reducing agents, and stabilizing ligands. The bare surface of the charged nanoparticles makes them highly available for functionalization and as a result especially interesting for biomedical applications. The functionalization with oligonucleotides is achievable simultaneously (*in situ*) or after (*ex situ*) nanoparticle generation by adding the conjugative agents to the ablation media prior or after laser ablation, respectively. In order to obtain information on the conjugation efficiency and resulting surface coverages, we applied two approaches modified from an established fluorescence-based method for the quantification of oligonucleotides after displacement from the surfaces of the gold nanoparticles. Surface saturation values up to 165 pmolcm^{-2} were observed for the *in situ* and *ex situ* laser-based conjugation. The observed conjugation efficiency in terms of the percentage of total oligonucleotides conjugated to the gold nanoparticles is about four times higher for the *in situ* conjugation. Nanoparticles with well-defined diameters were already obtained performing an *in situ* conjugation with an oligonucleotide to nanoparticle ratio of 20. At this minimum required concentration, more than 90 % of added oligonucleotides are conjugated to the surfaces of the nanoparticles, and a surface coverage of 29 pmolcm^{-2}, being in the range of reported values in literature, was observed. In conclusion, the laser-based bioconjugation seems to be an alternative approach to gold nanoparticle bioconjugates with defined surface coverage. Additionally, observed high conjugation efficiencies are especially interesting for precious biomolecules.

Introduction

Noble metal nanoparticles have attracted great attention in the last decades as they show interesting and versatile properties that differ from their bulk material. Especially, gold nanoparticles are of increasing interest for nanobiotechnology because of their high acceptance level in living systems [1] and the fact that they are fairly easily conjugated with functional molecules. Oligonucleotide-conjugated gold nanoparticles, for example, show a wide spectrum of applications ranging from biological sensors [2] to cell-targeting vectors [3]. Because of this demand, a variety of methods for gold nanoparticle preparation have been established. Among these, the standard synthesis method is based on the reduction of Au(III) in the presence of reducing agents such as citrate [4] or sodium borohydride [5] and stabilizing ligands. Alkylthiols are often used as ligands in unpolar liquids such as toluene because the sulfur atom has a high affinity to the gold surface being a soft Lewis acid [5]. As a result, long carbon chains radiate from the surface and particles are sterically prevented from aggregation in solution. Stabilization in aqueous systems, as demanded for biomedical applications, is often achieved by citrate anions forming a charged layer around gold nanoparticles and providing them with a repulsive force [6] The functionalization with, for example, thiolated oligonucleotides then involves a successive ligand exchange, which might afford certain reaction precautions as heating and buffering to obtain satisfactory yields and surface coverages [7]. To overcome the low bioconjugation yield, Burt *et al.* described a chemical method where the conjugative agent was directly added to the reduction process [8]. But purification to remove remaining precursors and/or reducing agents in order to avoid biological toxicity is still necessary [9]. An alternative method to obtain bioconjugated gold nanoparticles in a one-step process without the need of chemical precursors and reducing agents is laser ablation in liquids [10-13]. This approach takes advantage of the aspect that laser-generated gold nanoparticles possess a novel surface chemistry not reproducible by any other method [13-15]. X-ray photoelectron spectroscopy of these gold nanoparticles observed by Sylvestre *et al.* revealed the presence of the oxidation states Au$^+$ and Au^{3+} besides the metallic Au^0 due to partial oxidation in aqueous media [14]. Because of this partial oxidation, laser-generated gold nanoparticles act as electron acceptors; hence, they are easily coordinated by molecules bearing electron donor moieties as thiols or amines added to the ablation media prior (*in situ*) or after (*ex situ*) the laser process [14,16,17]. Thiolated and unmodified oligonucleotides could thus be conjugated to gold nanoparticles simultaneously or following their generation [10]. But to date, there is no information available on the conjugation efficiency of the laser-based bioconjugation with oligonucleotides, which is a determining parameter for the bioactivity of the modified nanoparticles [18]. There are a number of techniques described to investigate the surface coverage of planar surfaces and spherical particles ranging from microscopic approaches (e.g., AFM) [19] over microbalances [20] to biochemical methods (e.g., gel electrophoresis) [21]. Additionally, a

fluorescence-based method for the quantification of fluorochrome-labeled oligonucleotides after displacement with mercaptoethanol from the surfaces of the gold nanoparticles was introduced by Mirkin *et al.* in 2000 [22]. In the present study, we applied this method in a slightly modified version in order to evaluate a second approach applicable for non-labeled oligonucleotides that is the measurement of the absorbance of oligonucleotides contained in the supernatant after centrifugation. The latter was then used not only to investigate the conjugation efficiency of the laser-based bioconjugation in terms of the percentage of total oligonucleotides bound to the surfaces of nanoparticles but also to evaluate parameters that influence obtainable surface coverages. Investigated parameters were on one hand the concentration of the reactants being oligonucleotides and nanoparticles and on the other hand the way conjugation has been achieved (*in situ* and *ex situ*). Additionally, the footprint of laser-generated nanoparticle bioconjugates was discussed referring to literature values.

Experimental methods
Chemicals
Chemicals were purchased from Fluka Chemie AG (D-82024 Taufkirchen) and Sigma-Aldrich Chemie GmbH (D-89555 Steinheim). Single-stranded oligonucleotides with the sequence 5′cta-cct-gca-ctg-taa-gca-ctt-tg-3′ were purchased from Purimex (D-34393 Grebenstein) with a C6-thiol 5′ modification and for comparison without modification (HS-ssO, ssO). The fluorescence labeling of thiolated ssO with Alexa 488 or Cy5 at the free 3′ terminus was also established by Purimex (HSssO-Alexa 488, HS-ssO-Cy5). The gold foil (thickness: 0.1 µm; purity>99.99%) ablated by laser ablation was received from Goodfellow GmbH (D-61213 Bad Nauheim).

Preparation and characterization of gold nanoparticles
Laser generation of gold nanoparticles was carried out using a femtosecond laser system (Spitfire Pro, Spectra-Physics) delivering 120 fs laser pulses at a wavelength of 800 nm (maximum energy, 400 µJ per pulse; beam diameter, 4 mm). The pulse energy and distance of a 40 mm lens to the surface of the target, referred to as focal position, were fixed to 100 µJ and -2 mm at a repetition rate of 5 kHz because of previously performed degradation and stabilization yield determinations [11]. The focus in air is defined as the 0 focal position. A fluence of 0.35 Jcm^{-2} was estimated by measuring a spot diameter of 270 µm after 500 pulses on a gold target under same experimental conditions. The principle setup is described as follows: A 5 x5 mm gold foil, thoroughly cleaned, was placed on the bottom in a well of a 48 multiwell plate, filled with 500 µL of double distilled aqueous solution (ddH$_2$O) of single stranded oligonucleotides (0.0, 0.1, 0.25, 0.5, 1.0, 2.5,

5.0, and 7.5 µM). The well plate was then placed on an axis system that moved at a constant speed of 1 mms^{-1} in a spiral with outer radius of 1 mm and inner radius of 0.4 mm. Time of irradiation was fixed to 53 s (corresponding to one spiral) in media containing oligonucleotides and to 159 s (corresponding to three spirals) in water, if not indicated differently. TEM was used to determine the size distribution of resulting nanoparticles. At least 500 nanoparticles were sized from TEM micrographs, which revealed three significantly different size distributions in dependence of the HS-ssO concentration (Figure S1 of the Supporting Information A.2). One observes a size quenching with increasing HS-ssO concentration, which reaches its maximum at 0.5 µM (Figure S2 of the Supporting Information A.2). The average diameter of a typical particle preparation at HS-ssO concentrations higher than or equal to 0.5 µM is 5.0 ± 1.3 nm. HS-ssO concentrations of 0.1 µM and 0.25 µM result in slightly larger nanoparticles with an average diameter of 5.7 ± 3.4 nm. No significant difference was observed in the size of nanoparticles generated in 0.1 and 0.25 µM. Generation of gold nanoparticles in water leads to the typical broad distribution with an average Feret diameter of 15.0 ± 10.3 nm as there is no competition between growth and surface coating. Generated nanoparticle mass was estimated by weighing the gold foil three times prior and after ablation on a Sartorius balance (precision: 1 µg). With described laser parameters, average obtained nanoparticle concentrations are 25 ± 2 µgmL^{-1} or 51 ± 2 µg mL^{-1} in aqueous solutions of oligonucleotides and water, respectively. Molar concentrations were calculated considering mass-weighted distributions in order to account for broader size distributions, which is especially important for the generation in pure water. The average particle size then shifts to larger diameters: 5.3 nm for the generation in HS-ssO concentrations ≥ 0.5 µM and 7.0 nm for the generation in ssO concentrations <0.5 µM and 21.1 nm for the generation in water. Number and mass-weighted distributions are displayed in Figure S3 of the Supporting Information A.2. Assuming spherical particles with a density equivalent to that of bulk gold (19.30 gcm^{-3}), the average molar nanoparticle concentration is then 27 ± 2 nM or 13 ± 2 nM for HS-ssO concentrations lower or higher than 0.5 µM, respectively, and 1 nM for unconjugated nanoparticles. Mass and molar concentrations are measured and calculated for each sample prior to surface coverage estimation. For the *ex situ* conjugation of nanoparticles, 475 µL of aqueous nanoparticle dispersion were incubated 24 h with 25 µL of HS-ssO (final HS-ssO concentration 0.1-7.5 µM).
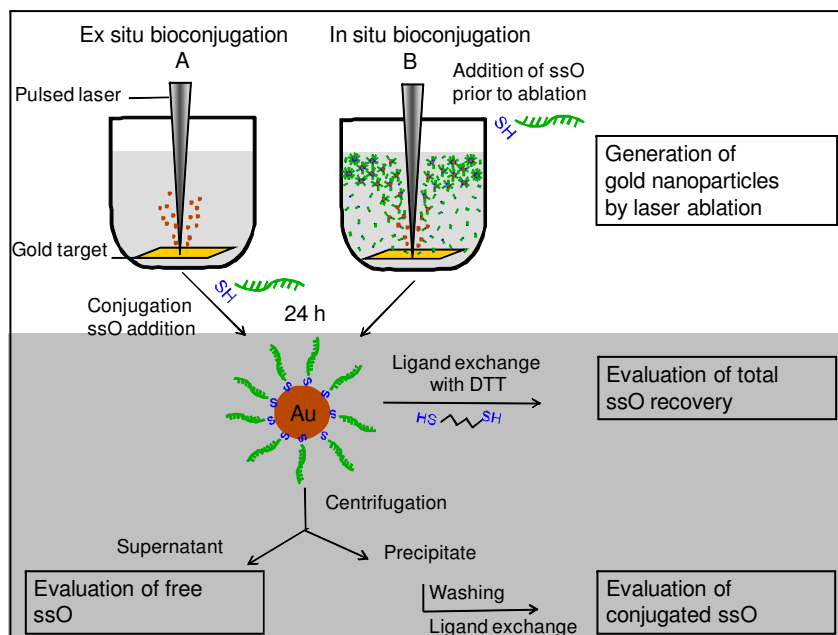
Figure 1.: Schematic description of the analytical process to determine the conjugation efficiency of the laser-based *ex situ* and *in situ* conjugation.

Table 1.: Comparison of recoverages after displacement with DTT of fluorochromes and HS-ssO-(X) after *ex situ* and *in situ* conjugation

	wavelength [nm]	ε [M^{-1}cm^{-1}]	recoverage after *ex situ* conjugation	recoverage after *in situ* conjugation
HS-ssO-X	260	184000	98 ± 2	98 ± 2
Alexa 488	496	70000	95 ± 1	90 ± 3
Cy 5	648	250000	96 ± 1	68 ± 1

Quantification of HS-ssO-X loaded on gold nanoparticles

After 24 h of co-incubation of oligonucleotides and nanoparticles, excess oligonucleotides were removed by centrifugation of nanoparticle suspensions for 30 min at 40000 g. The resulting supernatant was stored for further analyses. In the case of HS-ssO-Alexa 488 conjugation, the red precipitate was then washed twice with ddH$_2$O by successive centrifugation and redispersion and then finally taken up in 200 µL of an aqueous solution of 5 mM dithiothreitol (DTT). After 18 h at room temperature with intermitting shaking, the solutions containing the displaced HS-ssO-Alexa 488 were separated from the gold by a second centrifugation. Absorbance corresponding to excess HS-ssO (260 nm) in the first supernatant (Figure S6 of the Supporting Information A.2) and absorbance at 496 nm corresponding to displaced Alexa 488-labeled HS-ssO (Figure S7 of the Supporting Information A.2) in the second supernatant was recorded with a Shimadzu 1650 UV-Vis spectrometer. Intensities were converted to molar concentrations of ssO by interpolation from a linear standard calibration curve. Standard curves were prepared with known concentrations of HS-ssO-X (Figure S5 of the Supporting Information A.2). Finally, the average number of ssO per particle was obtained by dividing the measured HS-ssO-X molar concentration by the original nanoparticle concentration. Normalized surface coverage values were then calculated by dividing the estimated particle surface area (mean value of the surface-weighted distribution; see Table S1 of the Supporting Information A.2) in the nanoparticle suspension.

Quantification of recoverage or degradation of ssO after ligand exchange.

Twenty-five microliters of a 100 mM aqueous DTT solution was added to 475 µL colloid after *ex situ* and *in situ* conjugation with HS-ssO-X. Following centrifugation after 18 h of ligand exchange, absorbance at 496 and 648 nm was measured to estimate the concentration of displaced Alexa 488 and Cy 5, respectively. Recorded intensities were corrected in order to account for the DTT addition. Values after *ex situ* conjugation correspond to the recoverage after DTT displacement and after *in situ* conjugation to the sum of recoverage after DTT displacement and degradation due to laser irradiation.
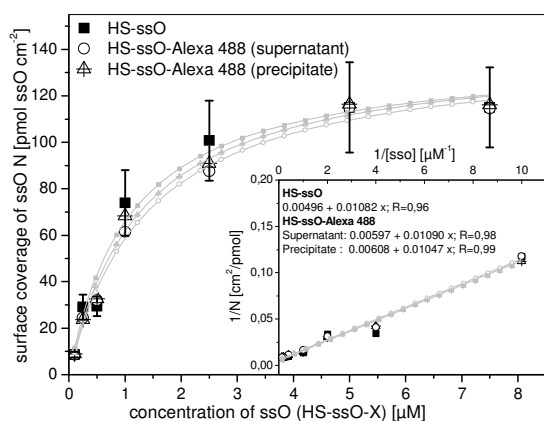
Figure 2.: Surface coverage after *in situ* conjugation of gold nanoparticles with HS-ssO-Alexa 488 as a function of ssO concentration determined by two methods: displacement with DTT and excess ssO in the supernatant. The latter were compared to HS-ssO modified nanoparticles. Error bars represent the variation in surface coverage due to the measurement error during nanoparticle mass determination. Insert: Linearization of the curves.

Results and discussion
Evaluation of measurement procedures and recoverage of analytes
Two different procedures were applied for the determination of the surface coverage and conjugation efficiencies: measurement of the absorbance of a fluorochrome labeled HS-ssO after displacement with DTT (established method from Mirkin *et al.* [22]) and measurement of the absorbance at 260 nm of the supernatant containing excess HS-ssO. While the latter should be also applicable to non-labeled HS-ssO, the first method just allows for the analysis of fluorescence-labeled HS-ssO as the absorbance of DTT interferes with the DNA-specific band at 260 nm. Measuring absorbance instead of fluorescence should avoid possible interference in the analysis because of quenching caused by gold nanoparticles in proximity [23]. But as high integrity of the fluorochrome (also after laser irradiation) and complete desorption of all oligonucleotides from the surface are requirements to guarantee an accurate measurement, we previously investigated these properties for two different fluorophore-labeled oligonucleotides: Alexa 488 and Cy5 (HS-ssO-X). Criteria for the choice of the fluorophores were their relatively high extinction coefficients, excitation wavelengths between the center wavelength of the laser beam (800 nm) and two photon process (400 nm), and high photostabilities. Both fluorochromes are well-recovered, but comparing their photostability after laser irradiation respective of *in situ* conjugation, one observes that Alexa 488 seems to be much more stable than Cy5, which shows a degradation of up to 28 % (32 % loss in recoverage after laser irradiation - 4 % loss without laser irradiation) (Table 1 and Vis spectra in Figure S8 of the Supporting Information A.2). The DNA recoverage, measured by gel electrophoresis, is up to 100 % undergoing laser irradiation or not, indicating that no degra-

dation is measurable. The recoverage of DNA was independent of the labeled fluorophore, which reveals that even the loss in recoverage of the fluorophores is probably enhanced by light exposition. In conclusion, DTT is an efficient ligand for the displacement of ssO, while Alexa 488-labeled HS-ssO are more adequate for analysis than Cy5 because of the lower degradation of Alexa 488 during laser irradiation. Further studies have been therefore committed with Alexa 488-labeled ssO, while the determined recoverage of the Alexa 488 after *in situ* conjugation has been considered for the estimation of surface coverage.

Surface coverage and conjugation efficiency by *in situ* conjugation
In the following, the two previously described methods were applied for the evaluation of the surface coverage of laser-generated gold nanoparticles with unlabeled and Alexa 488-labeled oligonucleotides. Results are displayed as function of the HS-ssO concentration in the ablation media prior to the laser process (*in situ* conjugation) in Figure 2. Error bars represent the variation in surface coverage due to the measurement error during nanoparticle mass determination. Because this fact has an equal impact on each of the three determination methods, error bars were exclusively added for the indirect determination of the surface coverage by remaining HS-ssO in the supernatant. No significant difference in surface coverage was observed between the indirect measurement via the supernatant and displacement of the HS-ssO-Alexa 488 from the surface. This observation is emphasized by the linearization of the curve resulting in an identical slope and intercept within experimental error. The fact that the approach via the supernatant was successful allows for quantification of HS-ssO without the need for further fluorescence labeling. The effect of organic fluorophores linked to HS-ssO on binding during laser ablation could thus be examined.

Again, no significant difference was detected (Figure 2), which assumes that the attachment of Alexa 488 to the free end of HS-ssO does not influence the binding site and binding strength of the HS-ssO on the nanoparticle. This finding indicates that the adsorption of Alexa 488 to the Au surface is much less probable than the formation of thiol-Au bonds. The nanoparticle mass concentration was kept at an average level of 25 ± 2 µgmL^{-1} during these experiments by applying same laser parameters (F= 0.35 Jcm^{-2}, t= 53 s). But nanoparticle size and as a consequence the molar nanoparticle concentration is dependent on the HS-ssO concentration. For HS-ssO concentrations greater than or equal to 0.5 µM, the mass-weighted particle size is 5.3 nm, and the resulting molar nanoparticle concentration is around 27 ± 2 nM. For lower concentrations, the ablation process resulted in slightly larger nanoparticles (mass-weighted

average diameter, 7.0 nm) due to less efficient size quenching [11]. As a consequence, the molar nanoparticle concentration for such probes is around 13 nM. Plotting the surface coverage as a function of the ratio of HSssO to nanoparticles (NP) might therefore be more appropriate than just the molar HS-ssO concentration (Figure 3). This allows not only different nanoparticle size distributions but also varying nanoparticle concentrations to be taken into account. As shown in Figure 2, an increase in oligonucleotide concentration higher than 5 µM does not cause higher surface coverages than 115 pmolcm^{-2}. In contrast, decreasing nanoparticle concentrations down to 6 nM, obtained via shorter irradiation times, results in a higher surface coverage of up to 146 pmolcm^{-2} at a constant HS-ssO concentration of 5 µM (Figure 3). In conclusion, besides the concentration of HS-ssO, the obtained surface coverage might be also influenced by the nanoparticle concentration present during conjugation. Data points below 200 HS-ssO per nanoparticle were not recorded for a fixed ssO concentration of 5 µM. These experiments would afford an increase in nanoparticle concentration, demanding longer ablation times and higher fluences, etc., provoking a possible degradation of oligonucleotides [11]. The determined surface coverage values as a function of the HS-ssO:NP ratio were fitted to the following equation (Eqn. 1) in which N is the surface coverage of HS-ssO, N_{sat} is the surface saturation, and K corresponds to the ssO:NP ratio that is required to obtain one-half of N_{sat}.

$$N = \frac{N_{sat} * [ssO:NP]}{K + [ssO:NP]} \qquad \text{(Eqn.1)}$$

The fit gives the values of 164.2 ± 6.9 pmol cm^{-2} for N_{sat} and 74.8 ± 11.8 ssO per NP for K (Figure 3). The observation of surface saturation allows us to assume that HS-ssO forms a monolayer on the surface of gold nanoparticles, which is in accordance with literature data for gold surfaces functionalized with thiols [5]. The conjugation efficiency of the *in situ* process has been estimated by the percentage of the total HS-ssO bound to the gold nanoparticles, always taking in account that unbound HSssO could be possibly reused after centrifugation for further conjugation experiments. Low HS-ssO:NP ratios of up to 40 seem to enable conjugation efficiencies of more than 90 % (Figure 3). Here, the binding seems to be limited by the amount of present HS-ssO in the ablation media. At higher ratios, the percentage of bound HS-ssO decreases rapidly due to beginning saturation of the nanoparticle surfaces. Interestingly the HSssO:NP ratio (~200) where surface saturation starts, is higher than the observed ratio required for the preparation of colloidal stable and size-quenched laser-generated gold nanoparticles, being around 20 HS-ssO:NP (0.5 µM ssO) [11].
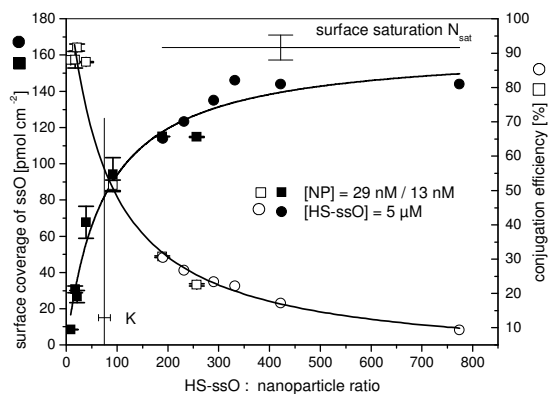

Figure 3.: Surface coverage and conjugation efficiency of the laser-based *in situ* conjugation as function of the ssO:NP ratio. Error bars represent the deviation of two equally performed conjugation experiments.
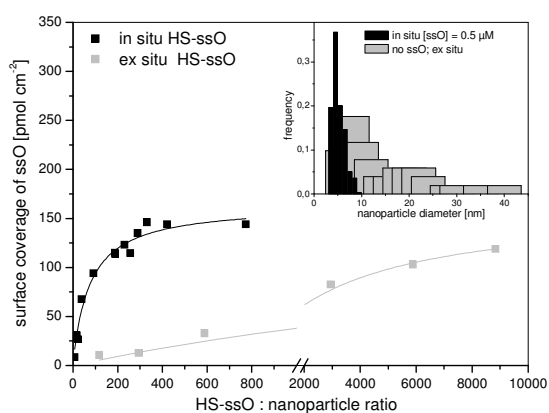

Figure 4.: Comparison of surface coverages obtained by *in situ* and *ex situ* conjugation of laser-generated gold nanoparticles with HS-ssO. Insert: Size distribution of *in situ* and *ex situ*-conjugated gold nanoparticles.

Just one-fifth of the surface saturation value seems to be required for efficient size quenching, which can be obtained with a conjugation efficiency of up to 90 %.

In situ versus *ex situ* conjugation

To account for the difference between *in situ* and *ex situ* conjugation with HSssO, we compared the surface coverage analysis data (Figure 4), while we should bear in mind that additional *ex situ* conjugation might occur during incubation after the *in situ* conjugation process. Obtained K values are 74.2 ± 11.8 and 3311.3 ± 877.0 ssO per NP for *in situ* and *ex situ* conjugation, respectively, while calculated surface saturation values are statistically equal (*in situ*: 164.2 ± 6.9 pmolcm^{-2}; *ex situ*: 163.5 ± 17.9 pmolcm^{-2}). The K value represents the ratio, which is required to reach half of the surface saturation (82 pmolcm^{-2}, corresponding to 41 or 493 ssO per NP). As a result, half of the surface saturation can be reached with 55 % conjugation efficiency by *in situ* conjugation (Figure 3), which decreases down to 15 % by *ex situ* conjugation (Figure S9 of the Supporting Information A.2).
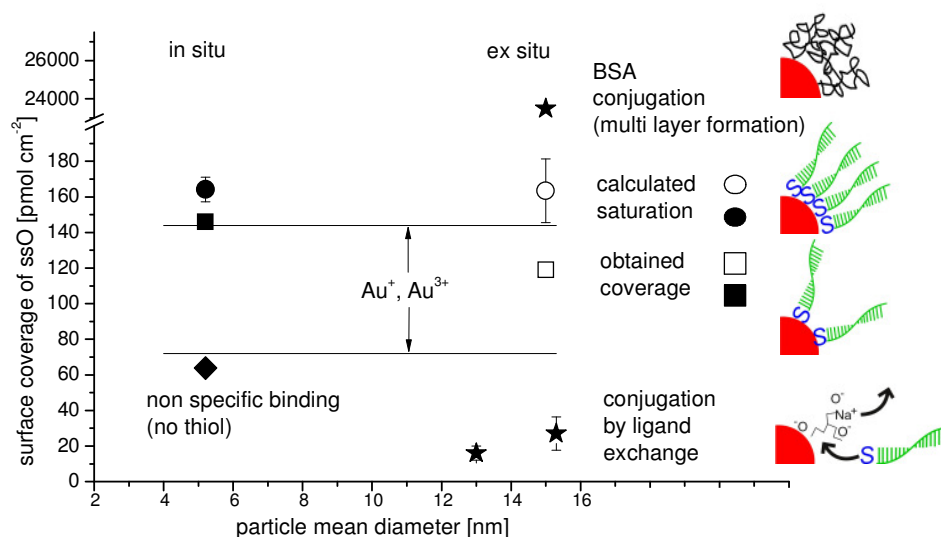
Figure 5.: Regimes of surface coverages obtained by *in situ* and *ex situ* conjugation during laser ablation compared to literature values [BSA conjugation [17], (Au+/Au3+) [26], ligand exchange (13 nm [27], 15.3 nm [22])].

Additionally, because of the different size distribution of nanoparticles and a possible activation of HS-ssO due to laser irradiation (which we could not observe by FTIR), we assume that the ablation process might cause a certain impact on the binding activity. We suppose that bioconjugation takes place in the millisecond to second regime after the collapse of the cavitation bubble. For nanosecond laser ablation, this bubble is formed on the target in a time scale of a few hundreds of microseconds due to local heating of the solvent in the vicinity of the ablated spot [24]. Activity of nanoparticles (surface activity, kinetic energy, etc.) at the time of conjugation might be therefore different in the two processes with different time intervals after primary nanoparticle formation, possibly leading to enhanced binding of oligonucleotides during *in situ* conjugation. While size quenching during *in situ* conjugation has been already discussed, after *ex situ* conjugation no difference is observed in the Feret diameter distribution of the gold nanoparticles. A look at the hydrodynamic size distribution reveals a slight increase of 2 nm due to the increased solvatisation shell of charged HS-ssO (Figure S10 of the Supporting Information A.2).

Footprint of HS-ssO-conjugated gold nanoparticles

The calculated surface saturation of 164.2 ± 6.9 pmolcm^{-2} implies that HS-ssO is binding to the gold surface by an end-on mechanism. Assuming that ssO has a hydrodynamic diameter of 1.2 nm and total length of 7.6 nm [25], the binding in an end-on mechanism would be 147 pmolcm^{-2}, where as the binding by a side-on mechanism would reach 18 pmolcm^{-2} for uncoiled HS-ssO. The maximum surface coverage of 146 pmolcm^{-2}, reached by *in situ* conjugation, coincidates well with this maximal binding in an end-on mechanism, while the calculated surface saturation is about 10 % higher. This might be due to the addition of the C6 chain on

the thiol modification lowering the hydrodynamic diameter of the anchoring site and allowing for higher surface coverage values. It is known that thiols interact with oxidized and not oxidized gold atoms. We found, that our calculated surface saturation is comparable to the amount of charged Au$^+$ and Au^{3+} atoms on the surface of laser-generated gold nanoparticles (Figure 5). Mafuné *et al*. described the attachment of the cationic surfactant cetyltrimethyl ammonium bromide to 11 nanometer-sized laser-generated gold nanoparticles, which led to the blocking of negatively charged Au-O$^-$ species at the surface and destabilization of the colloid [26]. Taking advantage of this electrostatic interaction, they estimated that 170 to 330 surface atoms are oxidized, which is equal to 74-144 pmol (Au$^+$ and Au^{3+}) per cm^2, assuming spherical gold clusters with 11 nm in diameter. Our maximal observed surface coverage values are in this range. However, at the same time, they coincide with the maximal binding in an end-on mechanism. Therefore, it is not evident whether oligonucleotides bind to oxidized gold atoms or not.

As we conjugated unmodified ssO under the same experimental conditions, we observed only half of the surface coverage compared to thiolated ssO (Figure 5). This difference is likely due to a nonspecific conjugation mechanism in the case of unmodified ssO. Comparing the conjugation efficiency of the laser-based bioconjugation with the standard techniques mostly involving ligand exchange, one observes an increase in surface coverage by a factor up to five (Figure 5) [22,27]. Although, it must be mentioned that sequences used by other groups were not exactly the same as in this study and differed slightly in base length and anchoring group (Table S2 of the Supporting Information A.2). Averaging literature values despite of differences, a significant enhancement factor up to five is observed.

Table 2.: Calculated surface saturation and maximal surface coverage values (N_{sat}, N_{max}) and K values for ssO-SH-conjugated gold nanoparticles

	N_{sat} (pmolcm^{-2})	N_{max} (pmolcm^{-2})	K (ssO NP^{-1})
ssO-SH *in situ* (NP, 5 nm)	164.2 ± 6.9	146	74.8 ± 2.1
ssO-SH *ex situ* (NP, 15 nm)	163.5 ± 17.9	119	3311.3 ± 877.0

In addition, we conclude from data that laser-generated nanoparticles seem to be highly available for the conjugation process, probably due to lacking protecting ligands, which might sterically hinder the conjugation process [8]. Meneghetti *et al.* described the *ex situ* conjugation of laser-generated gold nanoparticles with bovine serum albumin (BSA) and detected the formation of a protein multilayer [17]. This fact also underlines the high affinity of bare gold nanoparticles to bioconjugation. In the herein described approach, no multilayer formation was observed, probably because of repulsive forces between charged ssO and a highly specific Au-thiol binding.

Conclusion

We investigated the *in situ* and *ex situ* laser-based bioconjugation of gold nanoparticles with oligonucleotides with regard to conjugation efficiencies and surface coverages, which are highly influenced by the concentration of the conjugative agents and nanoparticles. Calculated surface saturation values N_{sat}, maximal obtained surface coverages N_{max}, and K values are displayed in Table 2. In comparison to conventional nanoparticle bioconjugation techniques as the ligand exchange method, up to five times higher maximal surface coverage values were observed for the laser-fabricated nanoparticles by *in situ* and *ex situ* conjugation. The strength of the interaction of the oligonucleotide with the gold nanoparticle seems to be higher during *in situ* conjugation. Observed conjugation efficiencies in terms of the percentage of total oligonucleotides conjugated to the gold nanoparticles are about four times higher compared to those of *ex situ* conjugation. The oligonucleotide binding in an end-on mechanism via weak covalent thiol-Au bonds was proposed with a space capacity dirigism. Nanoparticles with well-defined diameters, achieved by the size quenching mechanism during *in situ* conjugation are obtained performing the conjugation in an oligonucleotide to nanoparticle ratio of 20. The surface coverage is then hardly one-fifth of the maximum, while more than 90 % of added oligonucleotides are conjugated to the surface. As this surface coverage is in the range of reported values in the literature, bioconjugation during laser ablation presents a prospective and efficient preparation method, especially for the conjugation of precious biomolecules like aptamers or vectors. Another interesting feature is the tunability of the surface coverage allowing the fabrication of bioconjugates with varying degrees of activity, which is important for drug delivery systems [28].

References

[1] N. Lewinski, V. Colvin, and R. Drezek. *Small.* 4:26-49, 2008.

[2] R. Wilson. *Chemical Society Reviews* 37:2028-2045, 2008.

[3] A. Csaki, F. Garwe, A. Steinbrück, G. Maubach, G. Festag, A. Weise, I. Riemann, K. König, and W. Fritzsche. *Nano Letters.* 7:247-253, 2007.

[4] J. Turkevich, P.C. Stevenson, and J. Hillier. *Discussions of the Faraday Society.* 11:55-75, 1951.

[5] M. Brust, M. Walker, D. Bethell, D. J. Schiffrin, and R. J. Whyman. *Journal of the Chemical Society, Chemical Communications.* 7:801-802, 1994.

[6] S. Link, Z. L. Wang, and M. A. J. El-Sayed. *Journal of Physical Chemistry B.* 103:3529-3533 1999.

[7] A.G. Tkachenko, H. Xie, L. Liu, D. Coleman, J. Ryan, W.R. Glomm, M.K. Shipton, S. Franzen, and D.L J. Feldheim. *Bioconjugate Chemistry.* 15:482-490, 2004.

[8] J.L. Burt, C. Gutiérrez-Wing, M. Miki-Yoshida, and M.J. Yacaman. *Langmuir.* 20:11778-11783, 2004.

[9] J.A. Dahl, B.L.S. Maddux, and J. E. Hutchison. *Chemical Reviews.* 107:2228-2268, 2007.

[10] S. Petersen, J. Jakobi, and S. Barcikowski. *Applied Surface Sciences.* 255:5435-5438, 2009.

[11] S. Petersen, and S. Barcikowski. *Advanced Functional Materials.* 19:1167-1172, 2009.

[12] S. Besner, A.V. Kabashin, F.M. Winnik, and M. Meunier. *Journal of Physical Chemistry C.* 113:9526-9531, 2009.

[13] J.P. Sylvestre, A.V. Kabashin, E. Sacher, M. Meunier and J.H.T. Luong. *Journal of the American Chemical Society.* 126:7176-7177, 2004.

[14] J.P. Sylvestre, S. Poulin, A.V. Kabashin, E. Sacher, M. Meunier, and J.H.T. Luong. *Journal of Physical Chemistry B.* 108:16864-16869, 2004.

[15] A.V. Kabashin, M. Meunier, C. Kingston, J.H.T. Luong. *Journal of Physical Chemistry B.* 126 :4527-4531, 2003.

[16] G. Compagnini, A. A. Scalisi, and O. J. Puglisi. *Journal of Materials Research.* 19:2795-2798, 2004.

[17] V. Amendola, and M.J. Meneghetti. *Journal of Materials Chemistry.* 17 :4705-4710, 2007.

[18] D.A. Giljohann, D.S. Seferos, P.C. Patel, J.E. Millstone, N.L. Rosi, C.A. Mirkin. *Nano Letters.* 7:3818-3821, 2007.

[19] N. Mourougou-Candoni, C. Naud, and F. Thibaudau. *Langmuir.* 19:682-686, 2003.

[20] S.H. Brewer, W.R. Glomm, M.C. Johnson, M.K. Knag, S. Franzen. *Langmuir.* 21:9303-9307, 2005.

[21] T. Pellegrino, R. A. Sperling, A. P. Alivisatos, and W.J. Parak. *Journal of Biomedicine and Biotechnology.* 26796, 2007.

[22] L.M. Demers, C.A. Mirkin, R.C. Mucic, R.A. Reynolds, R.L. Letsinger, R. Elghanian, G. Viswanadham. *Analytical Chemistry.* 72:5535-5541, 2000.

[23] E. Dulkeith, M. Ringler, T. A. Klar, J. Feldmann, A. Munoz Javier, and W. J. Parak. *Nano Letters*. 5:585-589, 2005.

[24] T. Tsuji, Y. Okazaki, Y. Tsuboi, and M. Tsuji. *Japanese Journal of Applied Physics*. 46:1533-1555, 2007.

[25] M. Mandelkern, J. G. Elias, D. Eden, and D. M. Crothers. *Journal of Molecular Biology*. 152:153-161, 1981.

[26] H. Muto, K. Yamada, K. Miyajima, and F. Mafuné. *Journal of Physical Chemistry C*. 111:17221-17226, 2007.

[27] J.A. Dougan, C. Karlsson, E. Ewen Smith, and D. Graham. *Nucleic Acids Research*. 35:3668-3675, 2007.

[28] Z.P. Xu, Q.H. Zeng, G.Q. Lua, and A.B. Yu. *Chemical Engineering Science*. 61:1027-1040, 2006.

4.3. Laser ablation-based generation of bio-targeting gold nanoparticles conjugated with aptamers

Johanna Walter, Svea Petersen, Frank Stahl, Thomas Scheper, and Stephan Barcikowski

Laser ablation-based generation of bio-targeting gold nanoparticles conjugated with aptamers

Johanna-Gabriela Walter[1], Svea Petersen[2], Frank Stahl[1], Thomas Scheper[1], and Stephan Barcikowski[2]

[1] Institut für Technische Chemie, Leibniz Universität Hannover, Hannover, Germany
[2] Laser Zentrum Hannover e.V., Hannover, Germany

Abstract

Background: Bioconjugated nanoparticles are important analytical tools with emerging biological and medical applications. In this context *in situ* conjugation of nanoparticles with biomolecules via laser ablation in aqueous media is a highly promising one step method for the production of functional nanoparticles resulting in high conjugation efficiencies. Increased yields are required particularly considering the conjugation of cost intensive biomolecules like RNA aptamers.

Results: Using a DNA aptamer directed against streptavidin *in situ* conjugation results in nanoparticles with diameters of approximately 9 nm exhibiting a high surface density of aptamers (98 aptamers per nanoparticle) and a maximal conjugation efficiency of 40.3%. We have demonstrated the functionality of the aptamer-conjugated nanoparticles in three independent analytical methods including an agglomeration-based colorimetric assay and solid-phase assays proving high aptamer activity. To demonstrate the general applicability of the *in situ* conjugation of gold nanoparticles with aptamers we have transferred the approach to an RNA aptamer directed against prostate specific membrane antigen (PSMA). Successful detection of PSMA in human prostate cancer tissue was achieved utilizing tissue microarrays.

Conclusion: In comparison to conventional generation of bioconjugated gold nanoparticles by chemical synthesis and subsequent biofunctionalization, the laser ablation-based *in situ* conjugation allows the rapid one-step production. Due to high conjugation efficiency and productivity in situ conjugation can be easily used for high throughput generation of gold nanoparticles conjugated with precious biomolecules like aptamers.

Background

Gold nanoparticles (AuNPs) feature unique optical properties including a strong surface plasmon resonance- (SPR-) enhanced absorbance and scattering with high quantum efficiency. In addition with their resistance against photobleaching AuNPs perfectly fulfill requirements for the use as colorimetric sensors and markers. For the sensing or labeling of DNA targets, AuNPs are fairly easily functionalized with DNA via thiol linkers resulting in a highly ordered self assembled monolayer (SAM) [1,2]. Numerous colorimetric applications of DNA-conjugated AuNPs have been developed so far [3].

More recently, several applications of aptamer-conjugated AuNPs have been reported [4,5]. Aptamers are short single stranded DNA or RNA molecules that exhibit high specificity and affinity towards their corresponding target. Thus, aptamers can be thought of as nucleic acid analogues to antibodies that can be selected *in vitro* via SELEX (systematic evolution of ligands by exponential enrichment) against virtually any molecule including proteins as well as small molecules like metal ions [6-8]. Aptamer-conjugated AuNPs have already been successfully applied for the detection of proteins in a dry-reagent strip biosensor [9], detection of thrombin on surfaces [4], colorimetric detection of platelet-derived growth factor [5], detection of adenosine and potassium ions in an agglomeration-based approach [10], detection of thrombin in a dot blot assay [11] and for targeting and therapy of cancerous cells [12,13].

All applications of aptamer-conjugated AuNPs published so far are based on chemical synthesis of AuNPs in the presence of reducing and stabilizing agents and subsequent ligand exchange with aptamers. This ligand exchange might afford heating and buffering to end up with satisfactory yields and surface coverages [14].The latter might be limited by interference of remaining reducing agents with the aptamer during the replacement process. Additionally impurities due to remaining precursors and/or reducing agents might result in possible restriction of AuNPs use in biomedical applications [15,16].

Recently, laser ablation of gold in liquid environment has been applied for the production of AuNPs [17,18] using surfactants for growth quenching resulting in narrow nanoparticle size distributions [19]. Advantages of laser-generated AuNPs include high purity in combination with unique surface characteristics. The Au surface of laser-generated AuNPs is partially oxidized allowing an electrostatic stabilization of the colloid without chemical additives. These partially positively charged AuNPs, acting as electron acceptors, can directly interact with electron donors like amino or thiol groups in the ablation medium [20,21]. During laser ablation the DNA acts as a capping agent allowing precise size control of the resulting AuNPs as it has been
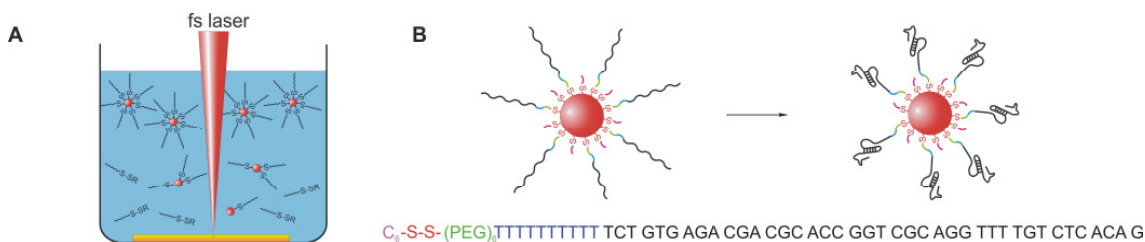
Figure 1.: Generation of aptamer-conjugated AuNPs via in situ conjugation. (A) Schematic illustration of in situ conjugation of AuNPs with aptamers during laser ablation in aqueous aptamer solution. (B) Spacer design and resulting mixed monolayer conjugated nanoparticles. Mixed monolayer formation and careful spacer design contribute to correct aptamer folding.

reported for the addition of cyclodextrines, biopolymers etc. before [22]. No ligand exchange is required, enabling higher conjugation efficiencies and surface coverages compared to wet chemistry methods [23]. Hence, bioconjugation during laser ablation presents a rapid and efficient preparation method especially for the conjugation of precious biomolecules like aptamers or vectors. In spite of these benefits, the utilization of laser ablation-based *in situ* conjugation for the generation of aptamer-conjugated AuNPs has not been reported yet.

We show the functionalization of nanoparticles with aptamers during femtosecond-pulsed laser-induced gold nanoparticle formation in aqueous media utilizing a DNA aptamer directed against streptavidin as a model system. In order to demonstrate the applicability of aptamer-conjugated AuNPs generated via laser ablation in complex biomedical applications we have used an RNA aptamer directed against prostate specific membrane antigen (PSMA) for the detection of PSMA in human prostate cancer tissue utilizing tissue microarrays.

Results and discussion
Choice of aptamer orientation and spacer design

In order to ensure aptamer activity, several factors concerning the ability of the aptamer to fold into the correct three-dimensional structure have been considered. We have previously reported the application of an aptamer directed against streptavidin (referred to as miniStrep) in protein microarray format [24, 25] .Utilizing this approach we have found that the miniStrep aptamer needs an additional spacer placed between aptamer and substrate to show activity which is slightly higher when immobilized via its 3´ terminus. Thus, we decided to utilize 3´ orientation. An additional oligothymidine (T10) spacer was placed between the disulfide group and the aptamer sequence. Tymidine was chosen since this nucleotide has the lowest affinity towards the gold surface in comparison to the other possible nucleotides [26]. Thus, nonspecific binding of the spacer bases to gold is minimized which should increase the surface loading and improve the elevation of the aptamer away from the nanoparticles surface. Taking these considerations into account the miniStrep aptamer

construct used in this work was the following: TCT GTG AGA CGA CGC ACC GGT CGC AGG TTT TGT CTC ACA G–T_{10}-$(CH_2)_3$-S-S-$(CH_2)_3$OH.

In case of the anti PSMA aptamer we also decided to immobilize via the 3´terminus. According to Lupold et al. the aptamer can be subjected to 3´ truncation of up to 15 nucleotides without losing its affinity to PSMA [27]. Since the 3´ terminal bases are not necessary for target recognition we decided to omit the utilization of an additional oligonucleotide spacer. Instead hexaethylenglycol was chosen as a spacer because it does not exhibit intermolecular repulsion that is one source of low DNA loading on AuNPs [28]. Furthermore, it does only occupy a small surface area allowing high packing densities [28] and is known to minimize nonspecific protein binding [29].Therefore, the used aptamer construct was the following: GGG AGG ACG AUG CGG AUC AGC CAU GUU UAC GUC ACU CCU UGU CAA UCC UCA UCG GCA GAC GAC UCG CCC GA-$(CH_2CH_2O)_6$-$(CH_2)_6$-S-S-$(CH_2)_6$OH.

The aptamers were directly used in laser ablation process without prior dithiothreitol (DTT) treatment (Figure 1 A). According to Dougan et al. this does not affect the surface coverage [30]. Moreover, the mercaptohexanol (MCH) of the mixed disulfide (aptamer S-S-$(CH_2)_6$OH) may serve as a co-adsorbent eliminating unspecific binding to the gold surface by occupying free binding sites [31]. Due to the formation of a mixed monolayer consisting of aptamers and short organic residues, the available space for optimal aptamer folding is enhanced (Figure 1 B).

In situ conjugation

Due to rapid one-step processing, laser ablation-based *in situ* conjugation enables the fast screening of different conjugation conditions. Utilizing this high throughput potential, we have determined optimal conjugation conditions by using different concentrations of miniStrep aptamer in Tris(hydroxymethyl)-aminomethan (Tris) buffer during laser ablation. Per investigated concentration the laser ablation process takes less than two minutes. A UV-Vis spectrum of AuNPs produced via laser ablation in the presence of 5 µM aptamer can be found in the Supporting Information (Figure S1)
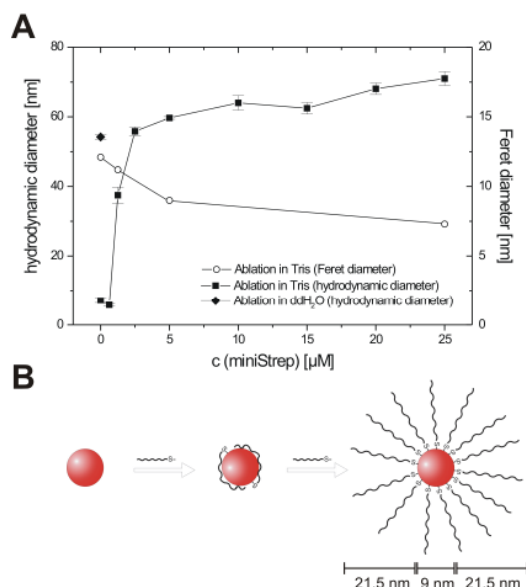
Figure 2.: Characterization of aptamer-conjugated AuNPs. (A) Hydrodynamic diameter and Feret diameter of the aptamer AuNP conjugates as a function of aptamer concentration used during laser ablation. (B) Suggested mechanism of the observed increase of the size of the conjugates. At low surface coverages the negatively charged aptamer lays flat on the positively charged AuNP surface. With increasing surface coverage the aptamers straightened up on the surface resulting in an increased hydrodynamic diameter. Scale bars illustrate the proportions of linearized aptamer and AuNP.

DLS measurements demonstrate that the hydrodynamic diameter (d_h) of the AuNPs increases with increasing aptamer concentrations (Figure 2 A). While d_h after ablation in Tris buffer (without aptamer) is 7 nm, d_h increases with increasing aptamer concentrations up to 5 µM and finally reaches a plateau of approximately 60 - 70 nm (Figure 2 A). We assume that this enlargement of d_h is a result of cumulative aptamer loading on the gold surface. At low surface coverages the aptamer lays flat on the surface due to non specific binding via the lone nitrogen electron pairs of the nucleotides. As the surface coverage increases the aptamers are forced to adopt a more perpendicular conformation due to electrostatic repulsion of the aptamers negatively charged phosphate backbones resulting in an enlargement of d_h (Figure 2 B). We estimated the length of the aptamer (including T_{10} spacer)

to be 21.5 nm utilizing a base to base distance for ssDNA of 0.43 nm [32]. For an aptamer-conjugated AuNP of 9 nm core size this results in a diameter of approximately 52 nm which is close to the observed plateau of d_h and supports our assumption (Figure 2 B).

On first sight the increase of AuNPs hydrodynamic diameter seems to be contradictory to our previous finding of a growth quenching effect induced by increasing DNA concentrations [20]. But in contrast to our previous work, here the ablation was performed in Tris buffer. Tris is able to interact with the surface of the embryonic AuNPs resulting in a prevention of further post-ablation nanoparticle agglomeration. Consequently, the AuNPs produced in Tris buffer are already stabilized by the buffer molecule resulting in reduced diameters (d_h= 7.1 ± 0.8 nm in Tris buffer versus 54.2 ± 0.6 nm in ddH2O (Figure 2 A)) and a diminished influence of the oligonucleotide concentration on the nanoparticles size. This assumption is supported by TEM analysis data. The Feret diameter (d_{Feret}) of AuNPs produced in Tris buffer slightly decreases from 12.1 to 7.3 nm with increasing aptamer concentration (Figure 2 A). In comparison to the Tris molecule the thiolated aptamer exhibits a higher affinity towards the gold surface resulting in better stabilization of embryonic particles and thus smaller AuNPs as detected via TEM analysis. Although there may be some portion of Tris-aptamer ligand exchange after nanoparticle generation, the size quenching effect observed by TEM analysis confirms the successful *in situ* bioconjugation during laser ablation.

In addition to the AuNPs size we have determined the aptamer loading (Table 1). For the AuNPs produced by laser ablation in 5 µM aptamer solution (*in situ*) we have found a loading of 98 aptamers per nanoparticle corresponding to 65 pmol/cm². This aptamer loading is higher than the results achieved by post production (*ex situ*) modification of chemically synthesized AuNPs with short oligonucleotides (Demers et al.: 34 pmol/cm²) [33] and the aptamer loading to chemically synthesized AuNPs reported by Huang et al. (13 pmol/cm²) [5]. The high aptamer loading achieved by *in situ* conjugation confirms the high availability of laser-generated

Table 1.: Characterization of aptamer-conjugated gold nanoparticles. Summary of data obtained for AuNPs conjugated with miniStrep aptamer in Tris buffer ([a] Hydrodynamic diameter, [b] Feret diameter, [c] Aptamers per AuNP surface, [d] Conjugation efficiency).

$c_{(miniStrep)}$ [µM]	d_h (DLS)[a] [nm]	d_{Feret}[b] [nm]	Aptamer/AuNP	Aptamer/A_{AuNP}[c] [pmol/cm²]	E_{con}[d] [%]
0	7.1 ± 0.8	12.1 ± 9.8	-	-	-
1.25	37.5 ± 2.3	11.2 ± 4.2	80 ± 2	33.93 ± 1.04	40.3 ± 0.3
5	61.1 ± 1.9	9.0 ± 5.0	98 ± 4	64.58 ± 1.82	19.8 ± 0.7
25	71.0 ± 2.0	7.3 ± 2.5	74 ± 11	73.90 ± 7.22	6.1 ± 0.9

AuNPs for bioconjugation. The conjugation efficiency was calculated as portion of provided aptamer bound to the nanoparticle surface (Table 1). At 1.25 µM aptamer concentration 40.3% of the available aptamer binds to the AuNPs which demonstrates the suitability of the method for efficient conjugation of precious biomolecules. Since we have observed no denaturation of the aptamer during laser ablation (as discussed in the next section), the remaining amount of aptamer can be reused.

After the ablation process, conjugates were slowly transferred into the aptamer selection buffer by addition of NaCl and MgCl$_2$. During this salting process we have observed precipitation of AuNPs produced at aptamer concentrations lower than 5 µM. The higher stability of AuNPs conjugated at aptamer concentrations of 5 µM (or higher) coincides with the plateau in the hydrodynamic diameter (Figure 2 B) and indicates better stabilization due to higher surface coverages. All further experiments were performed with AuNPs produced in 5 µM aptamer solution which was a compromise between maximal aptamer density and minimal aptamer consumption (Table 1). Under these conditions we were able to produce 75 µg (150 µg/ml) miniStrep-conjugated AuNPs within less than two minutes. The free aptamer was removed by centrifugation. In order to maintain conjugate activity, the centrifugation was performed at rather mild conditions (16600×g). This procedure results in a slightly increased average Feret diameter (14.6 nm) due to loss of small nanoparticles (see Supporting Information, Figure S2).

Functionality of miniStrep-conjugated AuNPs
The functionality of the immobilized miniStrep aptamer was confirmed by three independent methods. First, a classical agglomeration-based method was applied. Therefore, a fixed amount of AuNPs (0.69 nM) conjugated with miniStrep aptamer was incubated with different amounts of streptavidin (0 − 15.9 nM) and UV-Vis was detected. Since streptavidin is a tetrameric protein, agglomeration can be observed as a red shift of SPRMax (Figure 3 A). The shift in SPR$_{Max}$ increases with increasing concentrations of streptavidin and passes through a maximum at a streptavidin concentration of 2 nM. In addition to the SPR$_{Max}$ shift we have observed the formation of a red film on the wall of the reaction vessel along with a loss of AuNPs in solution at streptavidin concentrations from 1 nM to 4 nM. We assume that the red film is composed of big agglomerates while small agglomerates stay in solution and can be detected via the shift of SPR$_{Max}$ and TEM analysis. TEM micrographs of the agglomerates indicated a defined composition and tetrahedral structure of these agglomerates (Figure 4). Based on TEM analysis we have determined an agglomerate size of 35 nm (edge-to-edge length). In order to verify the proposed tetrahedral structure we have calculated the size of the agglomerates based on the observed shift of SPR$_{Max}$ utilizing the "plasmon ruler equation" [34]:

$$\frac{\Delta\lambda}{\lambda_0} \approx 0.18 \times \exp\left(\frac{-\left(\dfrac{s}{D}\right)}{0.23}\right)$$

This approximation describes the dependence between the observed shift of SPR$_{Max}$ ($\Delta\lambda$) on the interparticle gap (s) and nanoparticle size (D). Including our experimental results ($\Delta\lambda$=6 nm; λ_0=523.5 nm; D=d$_{Feret}$=14.6 nm) we have calculated an interparticle distance of 9.3 nm and an edge-to-edge length of the proposed tetrahedron of 38.5 nm. Taking into account that equation (1) is an empirical approximation established for a pair of interacting nanoparticles rather than for a tetramer and considering that the geometry of streptavidin is not perfectly tetrahedral, the deviation of 10% between the agglomerate sizes measured by TEM analysis and calculated from the shift of SPR$_{Max}$ seems to be acceptable. The good agreement between the agglomeration sizes obtained by two independent methods supports the proposed tetrahedral structure of the agglomerates. At streptavidin concentrations above 2 nM the shift of SPR$_{Max}$ decreases due to saturation of aptamers immobilized on the AuNPs surface with streptavidin (Figure 3 B). This saturation effect is in accordance with the observations of Huang et al. who have used an aptamer against a dimeric protein (platelet-derived growth factor)
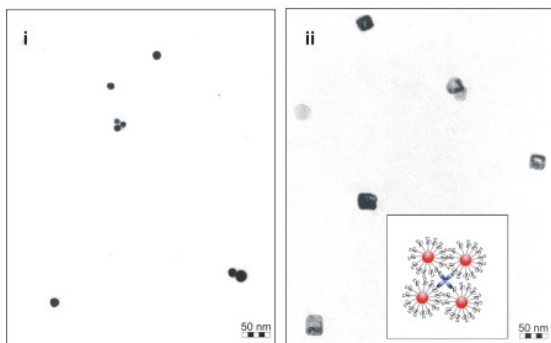
Figure 3.: Verification of the activity of aptamer-conjugated AuNPs. (A) The shift of the SPR maximum clearly indicates the formation of agglomerates in the presence of streptavidin. (B) Schematic illustration of the formation of agglomerates as a function of streptavidin concentration: At low streptavidin concentration relatively small agglomerates occur (i). At a medium streptavidin concentration the tetrameric protein induces the formation of large agglomerates (ii). An excess of streptavidin inhibits the formation of agglomerates by saturation of the aptamers bound to the nanoparticle surface (iii).

Figure 4.: TEM analysis of AuNPs conjugated with aptamers against streptavidin. TEM micrographs of AuNPs without streptavidin (i) and after incubation with streptavidin (ii). Insert displays a scheme of the proposed composition of the agglomerates. Please note that the agglomerates are displayed simplified in the scheme, de facto streptavidin is not planar but tetrahedral.

Figure 5.: Dot blot. Dot blot detection of streptavidin utilizing aptamer-conjugated gold nanoparticles (A). ESEM image of nanoparticles bound to streptavidin immobilized on the nitrocellulose membrane (B).

[5]. In order to gain quantitative insight into streptavidin binding and thus aptamers activity, the AuNPs were incubated with an excess of Cy3 labeled streptavidin. The agglomerates of aptamer-coated nanoparticles and attached streptavidin were removed by ultracentrifugation and the amount of bound streptavidin was determined by measuring the remaining streptavidin concentration in the supernatant.

Since the aptamer loading was determined for the whole AuNP population generated by laser ablation (d_{Feret}= 9.0 nm) and the binding of Cy3 labeled streptavidin was performed with the AuNP subpopulation resulting from removal of free aptamer by centrifugation (d_{Feret}= 14.6 nm) it was not possible to compare aptamer loading directly to amount of bound streptavidin. In order to estimate the aptamer activity, it was assumed that the aptamer density (pmol/cm^2) is not significantly affected by the nanoparticle diameter. Based on this assumption the aptamer loading was calculated to be 64.58 ± 1.82 pmol/cm^2 and the amount of streptavidin bound to AuNPs surface was 67.23 ± 0.76 pmol/cm^2 resulting in approximately 100% aptamer activity. This indicates that the aptamer is not degraded during the laser ablation process and optimal aptamer folding was achieved by careful design of the spacer.

To examine the applicability of the aptamer-conjugated AuNPs in solid phase assays, we have performed a simple dot blot assay (Figure 5 A). The nanoparticle aptamer conjugates exclusively bind to the immobilized streptavidin while no binding can be observed to BSA. The experiment was repeated with unconjugated nanoparticles resulting in no binding of AuNPs to the immobilized proteins (data not shown). This clearly demonstrates the specific binding of AuNPs to streptavidin via the aptamer conjugated to the nanoparticle surface.

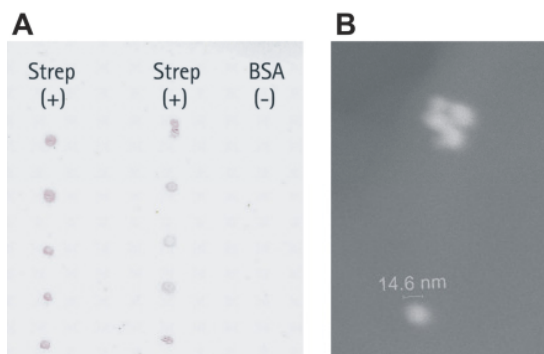The AuNPs bound to streptavidin during the dot blot assay were further analyzed via ESEM. The

ESEM micrograph approves the Feret diameter of the nanoparticles determined by TEM (Figure 5 B).

Functionality of anti PSMA-conjugated AuNPs

Encouraged by the positive performance of the dot blot assay our next aim was to prove the applicability of aptamer-conjugated AuNPs in more complex and demanding solid-phase assays. Therefore, we have used AuNPs conjugated with an aptamer directed against PSMA for detection of PSMA in prostate cancer (adenocarcinoma) tissue sections.

AuNPs conjugated with anti PSMA aptamer show a staining pattern similar to anti PSMA antibody. In both cases a positive staining of acinar epithelial cells was observed (Figure 6). In tissue sections treated with anti PSMA aptamer-conjugated AuNPs an additional staining of muscle cells was observed that was not detected in the positive control. Since the negative control does not show positive binding to epithelial cells nor false positive binding to muscle cells we assume the binding of anti PSMA conjugates to muscle cells to be induced by the PSMA aptamer. A positive staining of smooth muscle cells in prostate cancer has also been reported for one monoclonal antibody against PSMA (7E11) [35] and some authors assume that there may be a "PSMA-like" target in smooth muscle cells [36, 37]. Following this consideration the binding of AuNPs conjugated with anti PSMA aptamer to muscle cells may be the result of cross-reactivity of the aptamer with this unknown "PSMA-like" target. In summary, our results demonstrate that the anti PSMA aptamer AuNP conjugates are able to detect PSMA in acinar epithelial cells of human prostate cancer. This exemplifies the broad applicability of aptamer-conjugated AuNPs even in high complex biological matrices and bioimaging applications.
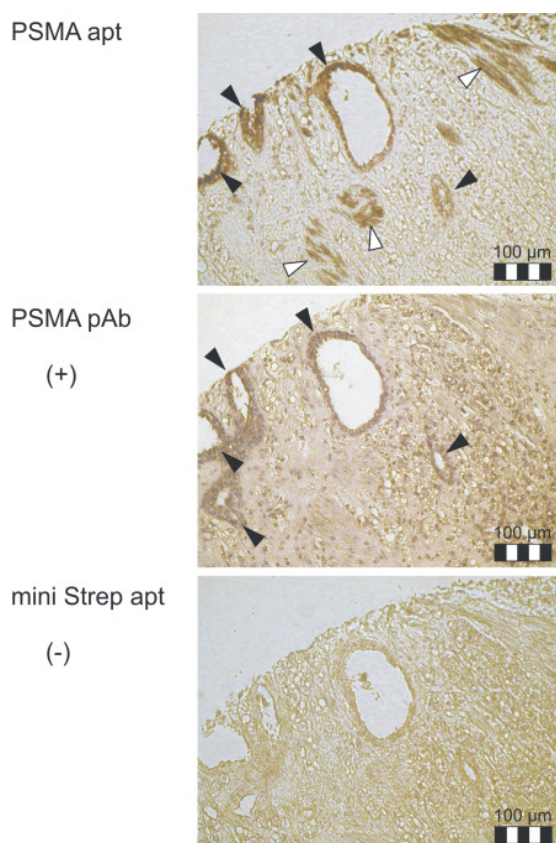
Figure 6.:- Detection of PSMA in human prostate cancer tissue. Detection of PSMA positive structures in prostate cancer tissue sections by immunohistochemical staining utilizing anti PSMA aptamer (PSMA apt)-conjugated AuNPs. As negative control AuNPs conjugated with miniStrep aptamer (miniStrep apt) were used. A polyclonal antibody directed against PSMA (PSMA pAb) was used as a positive control. Positive control was additionally stained with Haematoxylin and Eosin. Black arrows indicate specific staining, white arrows flag unspecific binding.

Conclusions

We have demonstrated the suitability of laser ablation-based *in situ* bioconjugation for production of functional aptamer-conjugated gold nanoparticles. Exploiting the potential of this rapid one-step method for high throughput screening, we have optimized the conjugation regarding aptamer loading and conjugation efficiency. Addressing the general applicability of the method, we have utilized two different aptamers composed of DNA and RNA. The high degree of aptamer activity determined on AuNP surface verifies that there is no heat-induced denaturation of the aptamer during laser ablation. We have proven the functionality of conjugates by three different methods (agglomeration-based assay, dot blot assay, tissue microarray) indicating the broad applicability of aptamer-conjugated gold nanoparticles for bioanalytical applications even in high demanding assays. Moreover, *in situ* conjugation avoids possible contamination by toxic educts, residual reducing agents or preservatives. Thus, this method could also be especially advantageous for medical applications.

Since *in situ* conjugation is a fast and simple one-step approach to pure conjugated AuNPs with high conjugation efficiency and productivity it can be easily used for the high throughput production of large amounts of different conjugated nanoparticles.

Methods
Materials

All chemicals were purchased from Sigma-Aldrich (Steinheim, Germany) or Fluka Chemie AG (Taufkirchen, Germany) and used as received. The aptamer against streptavidin (TCT GTG AGA CGA CGC ACC GGT CGC AGG TTT TGT CTC ACA G $-T_{10}$-$(CH_2)_3$-S-S-$(CH_2)_6$OH, referred to as miniStrep) [24] and anti PSMA aptamer (GGG AGG ACG AUG CGG AUC AGC CAU GUU UAC GUC ACU CCU UGU CAA UCC UCA UCG GCA GAC GAC UCG CCC GA-$(CH_2CH_2O)_6$-$(CH_2)_6$-S-S-$(CH_2)_6$OH) [27] were purchased from Biospring GmbH (Frankfurt, Germany). The gold foil was of 0.1 mm thickness and > 99.99% purity and was obtained from Goodfellow GmbH (Bad Nauheim, Germany).

Generation of aptamer-conjugated AuNPs

Laser ablation was performed in the buffer system the aptamer was originally selected in. For the miniStrep aptamer 50 mM Tris(hydroxymethyl)-aminomethan (Tris) pH 8.0 was used, anti PSMA aptamer was conjugated in 20 mM N'-2-Hydroxyethylpiperazine-N'-2 ethanesulphonic acid (HEPES) pH 7.4. Laser generation of AuNPs was performed utilizing a Spitfire Pro femtosecond laser system (Spectra-Physics) providing 120 fs laser pulses at a wavelength of 800 nm. 5×5 mm gold foils were placed in the wells of a 24 well plate filled with 500 µl of aptamer solution in the respective buffer. Ablation was performed while moving the plate at a constant speed of 60 mm×min^{-1} in a spiral (outer radius: 3 mm, inner radius: 1.5 mm) utilizing an axis system. The pulse energy was fixed to 100 µJ and the repetition rate was 5 kHz. In order to avoid heat-induced degradation of the aptamer, the focus position was adjusted to be -2 mm beneath the focus position determined in air [20].

Post generation processing of the aptamer-conjugated AuNPs

After laser ablation, the conjugates were allowed to age overnight at 4 °C before NaCl was added in increments of 25 mM by addition of 2 M NaCl in Tris-Cl or HEPES respectively. After each NaCl addition the colloidal solution was mixed and incubated for 1 h at room temperature. The addition of MgCl$_2$ and CaCl$_2$ was performed after another over night incubation at 4 °C by addition of 1 M MgCl$_2$ and 1 M CaCl$_2$. Final buffer compositions were the following: miniStrep: 150 mM NaCl, 10 mM MgCl$_2$, 50 mM Tris-Cl pH 8.0; anti PSMA: 150 mM NaCl, 1 mM MgCl$_2$, 1 mM CaCl$_2$, 0.05% Tween 20, 20 mM HEPES pH 7.4.

To remove free aptamer, the ablation medium was centrifuged for 15 min at 15000 rpm. The supernatant was transferred into a new centrifugal tube and centrifuged for another 30 min. The supernatant was discarded and the pellets were pooled and resuspended in the respective buffer. This process was repeated 4 times.

Characterization methods
UV-Vis spectra of the AuNP solutions were recorded utilizing a Shimadzu 1650 spectrophotometer. In order to determine the AuNP concentration the absorption at 380 nm (mainly corresponding to the interband transition of gold) was measured. Intensities were converted to AuNP mass concentrations by interpolation from a linear standard calibration curve (R^2 = 0.99). Standard curves were prepared with known concentrations of AuNP by weighting a gold target three times before and after ablation. Transmission electron micrographs (TEM) were commissioned at Stiftung Tierärztliche Hochschule, Institut für Pathologie (Prof. Dr. W. Baumgärtner, Kerstin Rohn) and were obtained utilizing a TEM Philip CM30 with 0.23 nm resolution. One drop of the colloidal solution was placed on a carbon coated, formvar covered copper grid and dried at room temperature. Given diameters are averaged over at least 200 AuNPs. Dynamic light scattering (DLS) measurements were performed utilizing a Zetasizer ZS (Malvern). Three consecutive measurements were carried out and average values are presented.

The amount of aptamer bound per nanoparticle was determined by measuring the concentration of the unbound aptamer. Therefore, aptamer-conjugated AuNPs were removed by ultracentrifugation (Beckman Coulter Optima Max, 30000×g) and the adsorption of the supernatant was measured at 260 nm against a serial dilution of aptamer in Tris buffer. Mean values of three measurements are presented.

Determination of miniStrep aptamer functionality
The agglomeration-based streptavidin assay was performed by incubating a fixed amount of miniStrep-conjugated AuNPs (0.69 nM) with varying concentrations of streptavidin (0-15.9 nM) for 16 h at room temperature. UV-Vis was measured to monitor the shift of SPR_{Max}.
Furthermore, the aptamer activity was determined in a "golden blot" [38] format similar to the method published by Wang *et al.* [11]. In brief, streptavidin (0.5 µl, 1 mg/ml in PBS) was spotted in 10 replicates onto a nitrocellulose membrane (Sartorius, Goettingen, Germany). After 1 h incubation at room temperature, blocking of the membrane was performed with 1% BSA in miniStrep selection buffer. The membrane was washed in the same buffer and incubated with a solution of AuNPs (20 µg/ml) for 2 h. Finally the membrane was washed with miniStrep selection buffer. As a negative control, BSA (0.5 µl,

1 mg/ml in PBS) was spotted on the membrane. Furthermore, the experiment was repeated with "bare" AuNP produced in Tris buffer in the absence of aptamer. In this experiment the miniStrep selection buffer was replaced by 50 mM Tris-Cl pH 8.0 in order to maintain colloidal stability of the non-stabilized nanoparticles. Environmental scanning electron microscopy (ESEM) of the membrane after incubation with AuNPs was performed with a Quanta 400 F (FEI, Eindhoven, Netherlands) in low vacuum conditions. A piece of membrane was placed on an aluminum holder and visualized without previous sputtering.
In order to determine the activity of the miniStrep aptamer bound to the AuNPs surface, the conjugate (28.5 µg/ml, 0.15 nM) was incubated with Cy3-labeled streptavidin (166.7 µg/ml, 2.8 µM) for 16 h at room temperature in the dark. The conjugates and bound streptavidin were removed by ultracentrifugation. The amount streptavidin bound to the nanoparticles was determined by measuring the streptavidin concentration remaining in the supernatant utilizing a Fluoroskan ascent fluorescence plate reader (Ex: 544 nm, Em: 590 nm). Mean values of 4 measurements are presented.

Determination of anti PSMA aptamer functionality
The activity of anti PSMA aptamers conjugated to AuNPs was investigated utilizing a tissue microarray consisting of paraffin embedded prostate cancer tissues (US Biomax, Rockville, MD, USA). After baking the slides at 60 °C for 30 min paraffin was removed by two washing steps in xylene (10 min each). The tissue arrays were rehydrated by consecutive washes in 100%, 95% and 70% ethanol followed by a washing step in ddH$_2$O (5 min each). Antigen retrieval was performed by placing the slides into 0.01 M sodium citrate pH 6.0 for 15 min at 95 °C. Consequently slides were washed with anti PSMA aptamer selection buffer and blocked in 5% goat serum (Millipore) in the same buffer. The anti PSMA selection buffer was used for all consequent assay steps. Incubation with the aptamer modified AuNPs (20 µg/ml) was performed for 2 h at 20 °C and 300 rpm in an Eppendorf shaker equipped with a slide adaptor after placing a secure seal incubation chamber (Grace Biolabs, Bend, OR, USA) filled with 800 µl of the respective AuNP solution on the slide. Slides were washed two times for 5 min with 1% goat serum and fixed for 15 min with 2.5% glutaraldehyde solution. Silver enhancement was performed utilizing a silver enhancer kit (Sigma) according to the instruction provided by the manufacturer.
AuNPs conjugated with miniStrep Aptamer in HEPES buffer were chosen as a negative control. All washing and incubation steps were performed as described above. As positive control, rabbit anti PSMA antibody directed against the C-terminal domain of human PSMA (Millipore)

was used.[39] Here, all washing and incubation steps were performed utilizing PBS. After incubation with 2.5 µg/ml rabbit anti PSMA for 2 h the slides were washed two times for 5 min with 1% goat serum and consequently incubated with a 1:20 dilution of 12 nm colloidal gold conjugated with goat anti rabbit IgG (Jackson Immuno Research; OD at 520 nm of stock solution: 2) for 1.5 h. High background of developed tissue arrays was removed as described by Springall *et al.* [40].

Competing interests
The authors declare that they have no competing interests.

Authors' contributions
JGW and SP carried out the *in situ* conjugations and partial drafting of the manuscript. JGW carried out the determination of aptamer functionality. JGW and FS carried out the tissue microarray experiments. SB carried out principal study design, manuscript drafting and supervision of nanoparticle generation. TS participated in the conception design and supervised aptamer-related work. All authors read and approved the final manuscript.

Acknowledgements

References
[1] A.P. Alivisatos, K.P. Johnsson, X. Peng, T.E. Wilson, C.J. Loweth, M.P. Bruchez Jr., and P.G. Schultz. *Nature.* 382:609-611, 1996.

[2] C.A. Mirkin, R.L. Letsinger, R.C. Mucic, and J.J. Storhoff. *Nature.* 382:607-609, 1996.

[3] K. Sato, K. Hosokawa, and M. Maeda. *Analytical Science.* 23:17-20, 2007.

[4] V. Pavlov, Y. Xiao, B. Shlyahovsky, and I. Willner. *Journal of the American Chemical Society* 126:11768-11769, 2004.

[5] C.C. Huang, Y.F. Huang, Z. Cao, W. Tan, and H.T. Chang. *Analytical Chemistry.* 77:5735-5741, 2005.

[6] C. Tuerk and L. Gold. *Science.* 249:505-510, 1990.

[7] A.D. Ellington and J.W. Szostak. *Nature.* 346:818-822, 1990.

[8] D.L. Robertson and G.F. Joyce. *Nature.* 344:467-468, 1990.

[9] H. Xu, X. Mao, Q. Zeng, S. Wang, A.N. Kawde, and G. Liu. *Analytical Chemistry.* 81:669-675, 2009.

[10] W. Zhao, W. Chiuman, J.C. Lam, S.A. McManus, W. Chen, Y. Cui, R. Pelton, M.A. Brook, and Y. Li. *Journal of the American Chemical Society.* 130:3610-3618, 2008.

[11] Y. Wang, D. Li, W. Ren., Z. Liu, S. Dong, and E. Wang. *Chemical Communications.* 2520-2522, 2008.

[12] C.D. Medley, J.E. Smith, Z. Tang, Y. Wu, S. Bamrungsap, and W. Tan. *Analytical Chemistry.* 80:1067-1072, 2008.

[13] Y.F. Huang, K. Sefah, S. Bamrungsap, H.T. Chang, and W. Tan. *Langmuir.* 24:11860-11865, 2008.

[14] A.G. Tkachenko, H. Xie, L. Liu, D. Coleman, J. Ryan, W.R. Glomm, M.K. Shipton, S. Franzen, and D.L J. Feldheim. *Bioconjugate Chemistry.* 15:482-490, 2004.

[15] S. Besner, A. Kabashin, F. Winnik, and M. Meunier. *Applied Physics A.* 93:955-959, 2008.

[16] E.E. Connor, J. Mwamuka, A. Gole, C.J. Murphy, and M.D. Wyatt. *Small.* 1:325-327, 2005.

[17] J. Sylvestre, A. Kabashin, E. Sacher, and M. Meunier. *Applied Physics A.* 80:753:758, 2005.

[18] S. Barcikowski, A. Hahn, A. Kabashin, and, B.N. Chichkov. *Applied Physics A.* 87:47-55, 2007.

[19] F. Mafuné, J. Kohno, Y. Takeda, T. Kondow, and H. Sawabe. *Journal of Physical Chemistry B.* 105:5114-5120, 2001.

[20] S. Petersen and S. Barcikowski. *Advanced Functional Materials.* 19:1167-1172, 2009.

[21] S. Petersen, J. Jakobi, and, S. Barcikowski. *Applied Surface Science.* 255:5435-5438, 2009.

[22] J.P. Sylvestre, A.V. Kabashin, E. Sacher, M. Meunier, and J.H.T. Luong. *Journal of the American Chemical Society.* 126:7176-7177, 2004.

[23] S. Petersen and S. Barcikowski. *Journal of Physical Chemistry C.* 113:19830-19830, 2009.

[24] J.A. Bittker, B.V. Le, and D.R. Liu. *Nature Biotechnology.* 20:1024-1029, 2002.

[25] J.G. Walter, O. Kokpinar, K. Friehs, F. Stahl, and T. Scheper. *Analytical Chemistry.* 80:7372-7378, 2008.

[26] H. Kimura-Suda, D.Y. Petrovykh, M.J. Tarlov, and L.J. Whitman. *Journal of the American Chemical Society.* 125:9014-9015, 2003.

[27] S.E. Lupold, B.J. Hicke, Y. Lin, and D.S. Coffey. *Cancer Research.* 62:4029-4033, 2002.

[28] S.J. Hurst, A.K. Lytton-Jean, and C.A. Mirkin. *Analytical Chemistry.* 78:8313-8318, 2006.

[29] F. Zhang, M.W. Skoda, R.M. Jacobs, S. Zorn, R.A. Martin, C.M. Martin, G.F. Clark, G. Goerigk, and F. Schreiber. *Journal of Physical Chemistry A.* 111:12229-12237, 2007.

[30] J.A. Dougan, C. Karlsson, W.E. Smith, and D. Graham. *Nucleic Acids Res.* 35:3668-3675, 2007.

[31] S. Balamurugan, A. Obubuafo, S.A. Soper, and D.A. Spivak. *Analytical & Bioanalytical Chemistry.* 390:1009-1021, 2008.

[32] S. Park, K. Brown, and K. Hamad-Schifferli. *Nano Letters.* 4:1925-1929, 2004.

[33] L.M. Demers, C.A. Mirkin, R.C. Mucic, R.A. Reynolds, R.L. Letsinger, R. Elghanian, and G.A. Viswanadham. *Analytical Chemistry.* 72:5535-5541, 2000.

[34] P. Jain, W. Huang, and M. El-Sayed. *Nano Letters.* 7:2080-2088, 2007

[35] Y. Kinoshita, K. Kuratsukuri, S. Landas, K. Imaida, P.M. Rovito Jr., C.Y. Wang, and G.P. Haas. *World Journal of Surgery.* 30:628-636, 2006.

[36] S.S. Chang, V.E. Reuter, W.D. Heston, N.H. Bander, L.S. Grauer, and P.B. Gaudin. *Cancer Research.* 59:3192-3198, 1999.

[37] M.C. Gong, S.S. Chang, M. Sadelain, N.H. Bander, and W.D. Heston. *Cancer Metastasis Reviews.* 18:483-490, 1999.

[38] D. Brada and J. Roth. *Analytical Biochemistry.* 142:79-83, 1984.

[39] G.P. Murphy, T.G. Greene, W.T. Tino, A.L. Boynton, and E.H. Holmes. *Journal of Urology.* 160:2396-2401, 1998.

[40] D.R. Springall, G.W. Hacker, L. Grimelius, and J.M. Polak. *Histochemistry.* 81:603-608, 1984.

5.   Laser-based generation and cellular uptake of gold nanoparticle-peptide conjugates

The immobilization of NAs on AuNPs, which has been shown to be achievable by fs LAL, is promising for the targeted diagnostic and therapeutic application of NPs.

However, besides NAs, the immobilization of peptides on AuNPs gains similar importance. They also contain recognition motifs, which might be used for a localized accumulation of the functionalized NPs. Furthermore, peptides containing so-called protein transduction domains are more and more used as carriers for various biomolecules but also NPs to efficiently translocate across cell membranes. As the cellular internalization is highly affected by NP size, surface charge etc. (chapter 2.1.2), the investigation of the optimal design of the NP-peptide conjugate is especially important for this issue. The applicability of the laser-based bioconjugation for the simple and rapid immobilization of peptides to AuNPs, addressed in the comprehended paper (chapter 5.1), was thus examined with the model CPP Penetratin. An activated penetratin, featuring a pyridyl disulfide (NPys) function at its N-terminal end with high affinity towards gold was chosen for specific functionalization.

Conjugation efficiency was found to depend on the pH of the ablation medium, probably due to the pH-dependent net charge of peptides and the charge of laser-generated AuNPs (chapter 2.4.3). Results reveal furthermore that there are probably three effects defining the bioconjugate size and shape at varied penetratin concentrations during fs LAL. A first size quenching effect, as also reported for NAs, was followed by the formation of aggregates, observed for penetratin concentrations higher or equal 5 µM. The cause might be a reduction in electrostatic repulsions as combination of negatively charged NP surface (Au-O$^-$) and positively charged penetratin. With even increased penetratin concentrations, the decrease of interparticle spacing and the deformation of spherical primary NPs were determined. This reshaping of primary particles probably results from a laser-induced partial melting and subsequent fusion of AuNPs with low interparticle distances in aggregates. The surface coverage of penetratin per AuNP represents an additional property, which was found to be tunable by the concentration of penetratin in the ablation medium.

To conclude, fs LAL allows the design of peptide-conjugated AuNPs with different particle and aggregate size and peptide surface coverage. In a preliminary biological application included in the paper, we could show a successful uptake of AuNP-Pen bioconjugates for the first time. Up to 100 % of co-incubated bovine endothelial cells were

marked with penetratin-conjugated AuNPs within 2 h. For comparison, just 77 % of the cells were marked with ligand-free NPs after 48 h of co-incubation (Own paper included in the thesis [2]). Hence, the penetratin conjugation seems to enhance uptake efficiency, and it also triggers a different mechanism. In contrast to uncoated AuNPs, the penetratin-conjugated AuNPs are situated in intracellular vesicles. The single steps of the internalization into cells of the cell line M3E3/C3 with stem cell character for pulmonary cells are depicted in TEM micrographs in Figure 5.1. They range from the association to the cellular membrane and the protrusion of the membrane around the AuNPs to the formation of intracellular vesicles. The mechanism is therefore supposed to be of micropinocytotic nature.
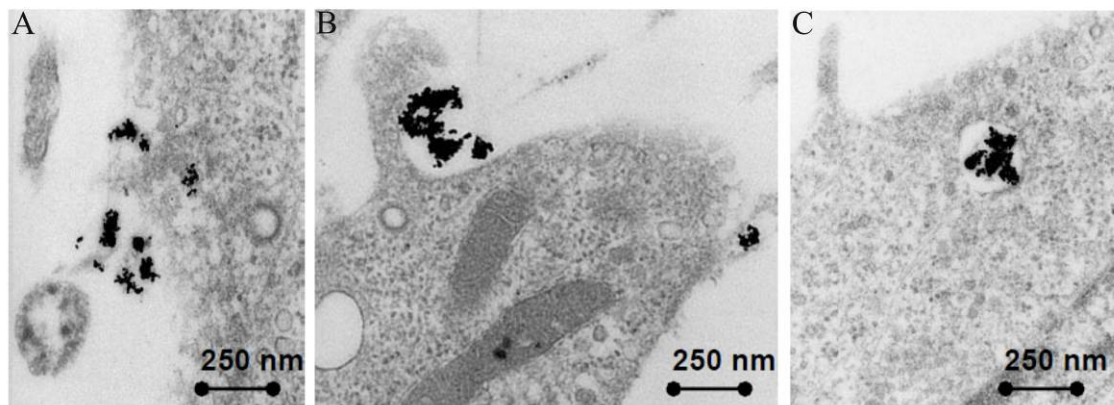
Figure 5.1.: TEM micrographs, visualizing the involved single steps of the internalization of penetratin-conjugated AuNPs into M3E3/C3: (A) membrane association, (B) protrusion of the membrane around AuNPs, and (C) AuNPs in intracellular vesicles.

The time scale of the internalization is shown in Figure 5.2. While after 30 minutes of co-incubation, most of the AuNPs are still membrane-associated (blue arrows) or not associated at all (yellow arrows), they are mainly situated in intracellular vesicles after 4 h of co-incubation (red arrows). These particle-carrying vesicles seem to be directed towards the cell nucleus.
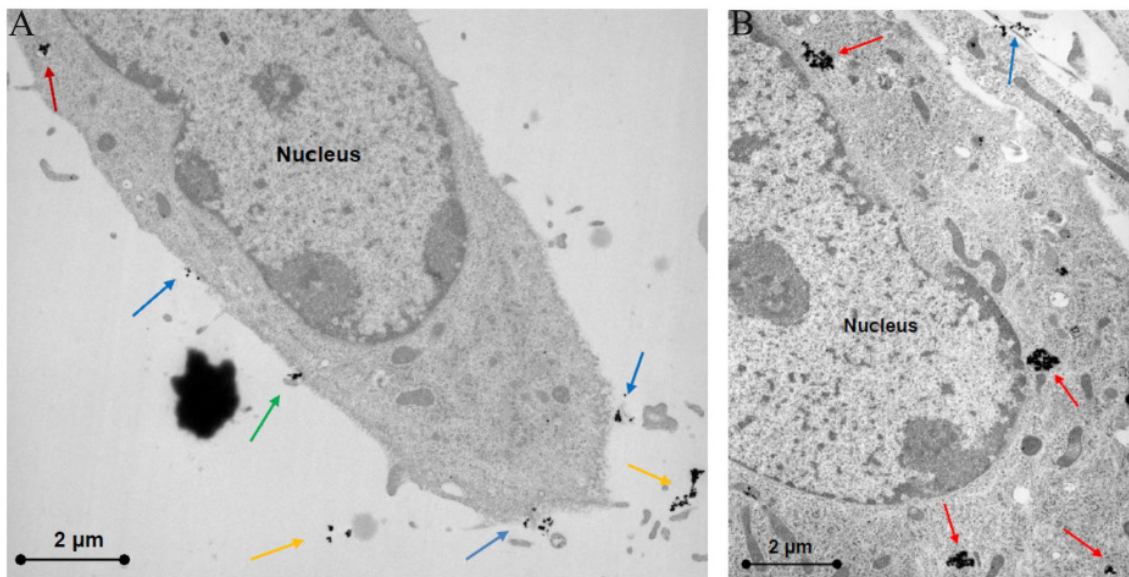
Figure 5.2.: TEM micrographs visualizing the time scale of internalization of penetratin-conjugated AuNPs into M3E3/C3: (A) 30 min and (B) 4 h of co-incubation.

The vesicular internalization of AuNPs, leading to the formation of aggregates, has advantages but also disadvantages, depending on the desired application. If the particles are not able to escape the vesicles, no interaction of AuNPs with specific cellular compartments can be achieved. Hence intracellular targeting would not be possible. But aggregation leads to a significant red shift of the SPR (chapter 2.1.1), which might be especially interesting for in vivo imaging and also photothermal therapy. Light scattering and heat release will be then efficiently triggered by 800 nm light irradiation, having a penetration depth of up to a few centimeters.

5.1. Penetratin-conjugated gold nanoparticles – Design of cell penetrating nanomarkers by femtosecond laser ablation

Svea Petersen, Annette Barchanski, Ulrike Taylor, Sabine Klein, Detlef Rath, and Stephan Barcikowski

Penetratin-conjugated gold nanoparticles - Design of cell penetrating nanomarkers by femtosecond laser ablation

Svea Petersen[1], Annette Barchanski[1], Ulrike Taylor[2], Sabine Klein[2], Detlef Rath[2], and Stephan Barcikowski[1]

[1]Laser Zentrum Hannover e.V., Hannover, Germany,
[2]Institute of Farm Animal Genetics, Friedrich-Loeffler-Institute, Mariensee, Germany

Abstract

Gold nanoparticles (AuNPs) are promising imaging agents for the long-term visualization and tracing of intracellular functions, as they bear outstanding optical properties and are fairly easily bioconjugated. However, the design of such multifunctional nanosystems might be limited by their bioavailability. Cell penetrating peptides (CPP) have shown to be efficient molecular transporters with very few indices of cytotoxicity also in conjunction to nanoparticles. But, probably due to the lack of methods, enabling a rapid design of nanoparticle bioconjugates with defined surface coverage values, there are no studies screening the influence of the peptide concentration and the morphology of AuNPs on cellular uptake efficiency and mechanism. The current work aims to explore the approach of *in situ* conjugation during laser ablation in liquids for the variable design of CPP-NP conjugates at the example of penetratin-conjugated AuNPs. By the variation of the peptide concentration during laser ablation, AuNPs with different degree of aggregation and peptide surface coverage values are obtained. The generation of cell penetrating nanomarkers by laser ablation thus enables correlation of particle size and shape and surface coverage with biological activity, i.e., internalization efficiency and mechanism. In a preliminary biological application, laser scanning confocal and transmission electron microscopy revealed a successful uptake of penetratin-conjugated AuNPs for the first time in up to 100 % of co-incubated cells within two hours.

Introduction

The visualization and observation of physiological structures and cellular functions is vital for understanding, diagnosing and treating diseases. Multifunctional nanosystems, composed of a combination of an inorganic core with a biomolecule shell, are reported to be promising imaging agents [1]. One inorganic core material with a high acceptance level in living systems are gold nanoparticles (AuNPs) [2]. They feature unique optical properties including a strong surface plasmon resonance (SPR) with high quantum efficiency and resistance to photobleaching, making them visable by laser scanning confocal microscopy (LSCM) [3]. The SPR maximum (SPR_{Max}) can vary from 500 to 1000 nm in dependence of nanoparticle size, aspect ratio and interparticle spacing. For example, the reduction of interparticle spacing during particle aggregation results in a red shift of SPR_{Max} due to interparticle plasmon coupling [4]. As a result, gold aggregates are easily excitable by near infrared lasers within the optical window of blood and tissue; hence they might be used for visualization and simultaneous photothermal therapy of labeled sites [5].

The functionalization of AuNPs can be achieved fairly easily via thiol linkers resulting in a highly ordered self assembled monolayer (SAM) [6]. With this method extracellular and intracellular targeting agents such as aptamers [7], antibodies [8] and/or effector molecules [9] are conjugable to the nanoparticle core.

However, the design of such multifunctional nanosystems might be limited by the question of their bioavailability. Previous studies have reported the direct but size and shape-dependent internalization of chemically derived AuNPs into several cell lines, while the time scale of internalization often occupies up to 48 h [10]. For a more efficient internalization, a number of invasive methods have been developed under cell culture conditions. The plasma membrane can be disrupted by electroporation, particle bombardment, ultrasound or microinjection, or permeabilized by detergents, organic solvents, or hypotonic buffers. In most approaches, the membrane disruption cannot be controlled, so that very often cell viability after treatment is low. Furthermore the conjugation to viral vectors [11] and dendrimers [12] was shown to enhance the cellular uptake of AuNPs. But the *in vivo* application of both approaches is confined as the biocompatibility of dendrimers has to be previously increased by PEGylation [13] and the risk of pathogenic mutations of viral vectors cannot be ruled out [14].

Molecular transporters with high uptake efficiency at low concentrations have been discovered in the early 90s, when a series of short peptide sequences, known as protein transduction domains (PTDs) were identified to efficiently cross cellular membranes [15]. Among these cell penetrating peptides (CPP), the most popular are Tat peptide and penetratin, derived from the human immunodeficiency virus type-1 (HIV-1) Tat (transactivator of transcription) and the *drosophilia antennapedia* homeodomain (Antp) respectively. The internalization mechanisms are still controversially discussed; one even assumes that some peptides cross the cellular membrane by more than one mechanism in

dependence of the cargo molecule and the peptide concentration [16]. Both, Tat and penetratin, were shown to induce successful internalization of diverse biomolecules including DNA [17] and proteins [18]. Additionally, Tat conjugated to AuNPs via BSA [19] or tiopronin [20] has been already described to efficiently deliver the nanoparticles into cells and even the nucleus.

However, probably due to the lack of rapid nanoparticle synthesis methods, enabling a fast design of nanoparticle bioconjugates with defined surface coverages, there are no studies screening the influence of the peptide concentration, the morphology of AuNPs and further CPP on the internalization of nanoparticles. In previous studies we established the *in situ* bioconjugation of AuNPs with thiolated single stranded oligonucleotides during ultrashort-pulsed laser ablation in liquids [21]. This one-step method allowed a rapid and simultaneous generation and conjugation of AuNPs with variable surface coverage values and bioconjugate sizes in dependence of the biomolecule concentration [22]. Here, we explore this method for the design of penetratin-conjugated gold nanoparticles. An activated penetratin (Pen: (Ac)NPys-CRQIKI-WFQNRRMKWKK(Ac)), featuring a pyridyl disulfide (NPys) function at its N-terminal end with high affinity towards gold was chosen for specific functionalization of AuNPs. After examining the conjugation efficiency at various pH values of the ablation medium, AuNP-Pen bioconjugates are generated within less than one minute of laser ablation in aqueous solutions containing different amounts of Pen. SPR, surface coverage, and particle size and shape are thus systematically varied and their correlation with biological activity, i.e., internalization efficiency and mechanism may be enabled. In the paper at hand, we discuss a preliminary biological application, investigating the internalization efficiency of AuNP-Pen bioconjugates in comparison to the direct internalization of ligand-free AuNPs for the first time.

Results and discussion
The conjugation efficiency is defined by the pH value of the ablation medium
As the net charge of peptides and the charge of laser-generated AuNPs are dictated by the pH value of their environment [23], conjugation efficiency will probably also function in dependence of the pH of the ablation medium.

Penetratin is highly positively charged at neutral pH contributed by basic residues of lysine (K) and/or arginine (R). The net charge of penetratin was calculated at various pH values based on the acid dissociation constants of the individual amino acids and the C terminus (Figure 1 A) [24]. Because the N terminus of the peptide is acetylated, there was no N terminus included in calculating the pI of 12.8, and only the charged
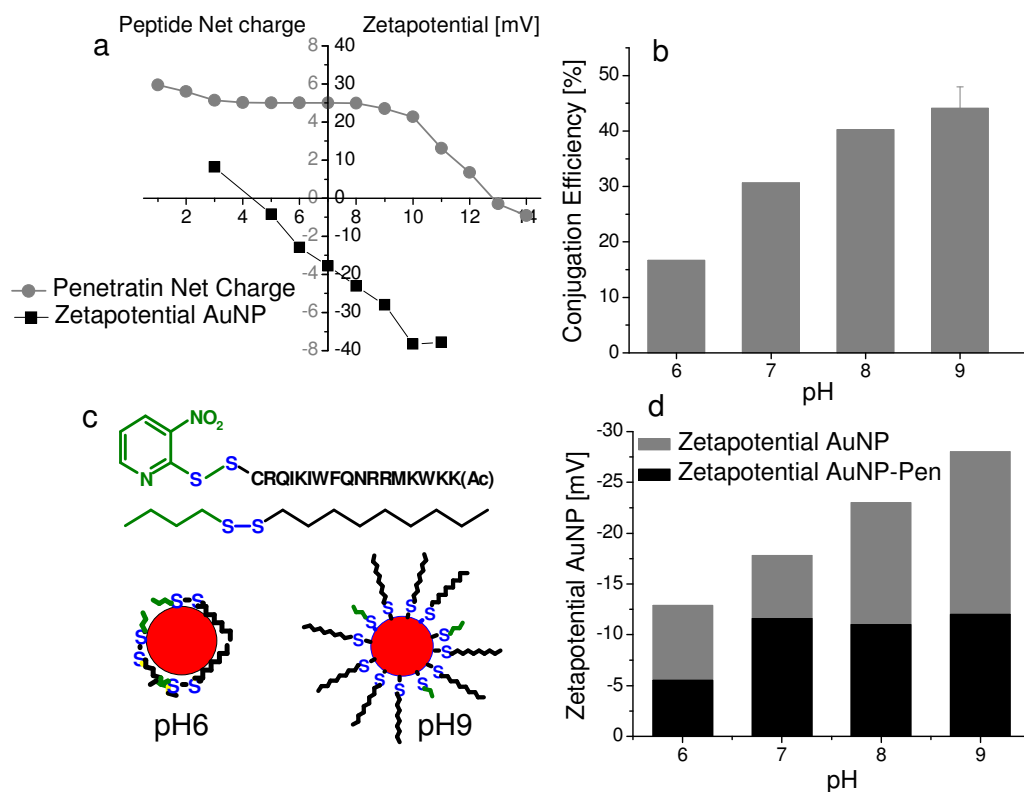
Figure 1.: Conjugating AuNP with penetratin: (A) Calculated penetratin net charge and the measured zetapotential of AuNPs with varying pHs. (B) Percentage of added peptides (5µM) conjugated to AuNPs increases with the pH of the laser ablation medium. (C) Estimated footprint of bioconjugates generated at pH6 and pH9. (D) Zetapotential of bioconjugates decreases in value with augmenting conjugation.

amino acids (K, R) and the C terminus contributed to the overall peptide charge.

The pH-dependent charge of AuNPs, generated under our experimental conditions, was estimated by ζ-potential measurements. The decay of the ζ-potential with increasing pH values (Figure 1 A) confirms data reported in literature, which describe the partial oxidation of AuNPs and their successive association by dissociated water [23,25]. As a result, protonated hydroxyl groups ($-OH_2^+$), non protonated hydroxyl groups (-OH) and $-O^-$ are in equilibrium, whose relative abundance is dictated by the pH value of their environment. Under our experimental conditions, AuNPs hardly show any charge at pH values < 6; hence -OH is dominant on the AuNPs surface leading to particle aggregation in the absence of stabilizing molecules due to the lack of efficient electrostatic stabilization. At pH values ≥ 6 the abundance of $-O^-$ increases and the AuNPs global charge is getting increasingly negative. The conjugation of AuNPs with penetratin was investigated at pH 6 to pH 9, in order to avoid increased repellence between AuNP and penetratin at low pHs due to the presence of some protonated hydroxyl groups at the AuNPs surface and isoelectric point aggregation and/or precipitation of the peptide at elevated pHs. Extreme pHs were furthermore omitted to achieve better biocompatibility conditions already during bioconjugate synthesis and reduce purification steps for biological application.

An augmentation of conjugation efficiency, being defined as the percentage of total peptides bound to the AuNPs surface, could be observed with increasing pHs (Figure 1 B). A possible explanation might be a dominant non-specific electrostatical interaction of penetratin with negatively charged AuNPs at low pHs, demanding more space than the formation of Au-thiol bonds. At higher pH, the peptide is slightly losing its positive charge, which might enhance dative

binding of penetratin via the sulfide to the positive gold core (Figure 1 C). Mass spectrometry measurements (MALDI-TOF) of samples, obtained in pH 9, reveal an increased second peak, having a mass difference of 155 Da compared to the molar mass. This difference corresponds to the nitro-pyridyl sulfide residue, which is obviously more efficiently cleaved by the present gold nanoparticles at pH 9 compared to pH 6, confirming the assumption of an enhanced dative binding at higher pH (Figure S1 in Supporting Information A.4). The formation of a mixed disulfide layer of peptide and nitro-pyridyl sulfide on the AuNPs surface might be the result, as it has been already reported for gold substrates in literature [26]. Following bioconjugates will be generated at pH 9.
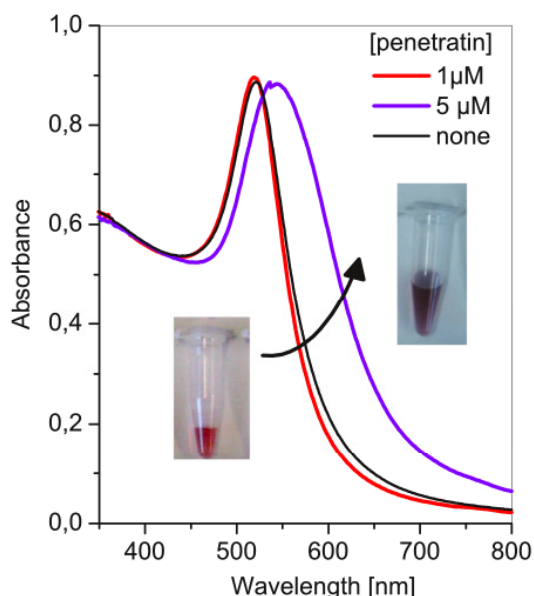
Figure 2.: UV-Vis spectra of ligand-free and penetratin-conjugated AuNP generated by laser ablation in water and in 1 and 5 μM penetratinsolutions at pH 9.
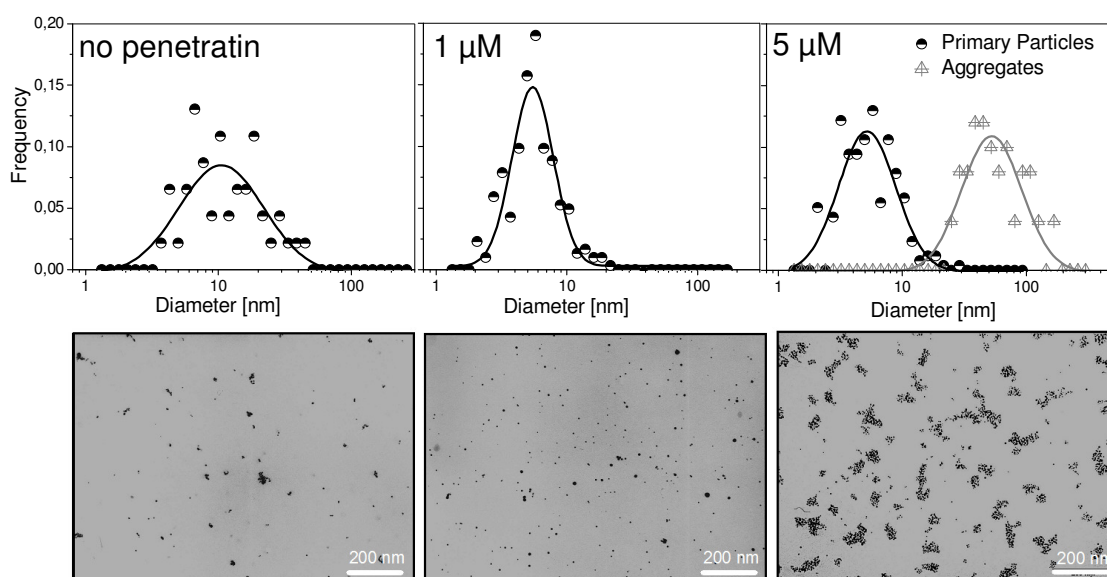
Figure 3.: Influence of penetratin concentration on size and shape of the nanomarkers: TEM histograms (top) and TEM images (bottom) of ligand free and penetratin-conjugated AuNP generated by laser ablation in water and in 1 and 5 μM penetratin solutions at pH9
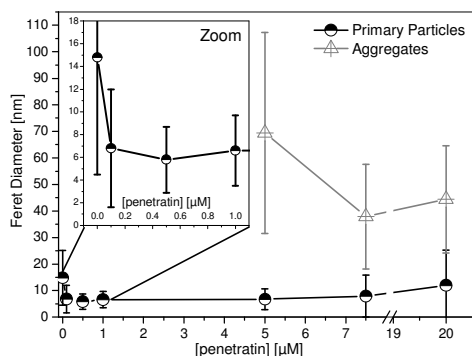
Figure 4.: Influence of penetratin concentration on the Feret diameter (average diameter of primary particles and aggregates of AuNP-Pen conjugates).
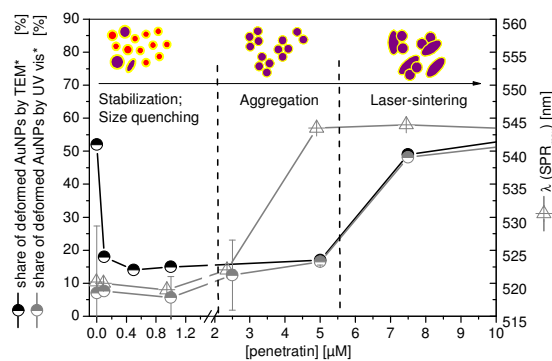

Figure 5.: Share of deformed AuNPs, estimated by TEM and UV-vis spectroscopy, and shift in SPR_{max} in function of the penetratin concentration in the ablation medium at pH9. *The share of deformed AuNPs, estimated by TEM micrographs, was defined as the share of AuNP with a form factor of less than 0.9. ** The share of deformed AuNPs, estimated by UV-vis spectroscopy, was defined as the ratio of the absorbance at 800 and 380 nm.

The ζ-potential of all bioconjugates shifted towards zero compared to ligand free AuNPs, generated at the same pH (Figure 1 D). The ζ-potential difference increased from +7.4 mV at pH 6 to +16 mV at pH 9, correlating with the amount of conjugated positively charged penetratin.

Designing AuNP-CPP bioconjugates varying the penetratin concentration

The design of AuNP-Pen bioconjugates was characterized after laser-based bioconjugation in aqueous solutions containing different amounts of penetratin at pH 9. Within less than one minute of laser ablation, the ablation media were intensively colored, while a red shift of SPR_{max} with increasing penetratin concentration was observed (Figure 2).

In order to estimate the Feret diameter distribution and shape of the nanomarker, TEM micrographs were recorded and size histograms were deduced for varied peptide concentrations in the ablation media (Figure 3 TEM images of bioconjugates, generated in 0, 1, and 5 µM penetratin). Results reveal that there are probably three effects defining the bioconjugate size and shape at varied penetratin concentrations during laser ablation. Among these, the first mechanism is the documented and known size quenching effect, appearing during nanoparticle generation by laser ablation in liquids containing reactive molecules [23,27].

Here, AuNPs generated in water, show the typical broad size distribution with an average Feret diameter of 15 nm, which then starts to decrease

with increasing peptide concentrations down to 6 nm (Insert Figure 4), where it stabilizes until a penetratin concentration of 5 µM (Figure 4).

The second effect becomes obvious by regarding TEM micrographs, where the formation of aggregates is observed for penetratin concentrations higher or equal 5 µM (Figure 3). This effect seems more specific to peptide-like molecules, since it is not observed during the conjugation of nucleic acids [21]. As we observed more aggregation for higher peptide concentrations, the reason of "bridging" flocculation can be excluded. The cause might be more likely a reduction in electrostatic repulsions, which is confirmed by the lower ζ-potential value of bioconjugates with increasing peptide concentrations (Figure S2 of the Supporting Information A.4). The shift in SPR_{max} follows the formation of aggregates and is therefore dedicated to the decrease of the interparticle spacing (Figure 5).

The third effect occurs at penetratin concentrations above 5 µM and results in the decrease of interparticle spacing and the deformation of spherical primary nanoparticles (Detailed micrographs of bioconjugate aggregates generated in 5 and 20 µM of penetratin in Figure S3 of the Supporting Information A.4). This reshaping of primary particles probably results from a laser-induced partial melting and subsequent fusion of AuNPs with low interparticle distances in aggregates, as it has been observed by Mafuné *et al.* during irradiation of a mixture of gold and

Table 1.: Summary of nanohybrid surface coverage and particle characteristics. Values are means ± standard deviation.

[Penetratin] [µM]	$d_{F(NP)}$	$d_{F(Cluster)}$	Zeta Potential [-mV]	Penetratin/NP
0	15 ± 10	-	28 ± 3	-
0.1	7 ± 5	-	26 ± 1	10
0.5	6 ± 3	-	29 ± 1	24
1	7 ± 3	-	25 ± 1	27 ± 2
5	7 ± 4	69 ± 38	12 ± 2	43 ± 6
7.5	8 ± 8	38 ± 20	9 ± 5	74

platinum nanoparticles [28]. As a consequence, primary particle size, detected by TEM, seems to re-increase while aggregate size decreases (Figure 4). For an estimation of the degree of particle deformation, we calculated the percentage of total AuNP in TEM micrographs having a form factor (FF) below 0.9. A perfect circle, characteristic for primary nanoparticles even when assembled in aggregates, has an FF of 1.0 whereas irregular structures like sintered particles, deviate from unity towards zero, as their degree of circularity becomes less perfect [29]. The resulting graph in function of the peptide concentration correlates well with the described observations and interestingly also with the ratio of the absorbance at 800 nm to the absorbance at 380 nm of the SPR spectra (Figure 5). The absorbance at 800 nm is mainly due to asymmetric aggregates, while the absorbance at 380 nm is primarily caused by the interband transition of gold, being a good parameter for the estimation of AuNP concentrations. However, for lower peptide concentrations the correlation was deficient, as estimation by TEM analysis indicated a higher degree of deformed particles than the SPR spectra. Possibly AuNPs, generated in the absence or in the presence of a very low amount of penetratin, just show a low degree of aggregation in dispersion and form aggregates with overlapping nanoparticles on the TEM grid due to drying effects during the preparation for microscopical analysis and therefore mimic deformed particles.

In relevance to biological application, one can conclude that laser ablation enables the fast generation of bioconjugates with tunable particle size and shape. Both parameters have been reported to determine cellular internalization. For example two independent groups reported that the cell penetration of AuNPs by endocytosis is most efficient for nanoparticle sizes of 40 nm [10,30]. Additionally, Lee *et al.* described the enhanced uptake of AuNP aggregates compared to primary AuNPs of 15 nm in average diameter [31]. Although the uptake mechanism of penetratin-conjugated AuNPs might be different, one could suggest that the aggregates are interesting candidates to aid the effective internalization of nanomarkers. The SPR of the laser-generated bioconjugates remains sharp until 5 µM, which guarantees a wavelength precise bioimaging even for aggregates. For higher peptide concentrations the SPR broadened (further UV-Vis spectra in Figure S4 of the Supporting Information A.4). The surface coverage of CPP per AuNP represents an additional property, which is tuneable by the concentration of penetratin in the ablation media (Table 1). Like nanoparticle size and shape, the surface coverage might also have an influence on the cellular uptake efficiency and mechanism.

Cellular internalization of penetratin-conjugated gold nanomarkers

In order to gain a first insight into the cell penetrating properties of femtosecond laser-generated AuNP-Pen nanomarker, we performed a 2 h co-incubation of bovine endothelial cells with ligand free AuNPs and AuNPs, conjugated to penetratin by *in situ* conjugation during laser ablation in 5 µM penetratin. LSCM proved the outstanding optical properties of AuNP-Pen aggregates of 70 nm with an average surface coverage of 43 penetratin per each primary nanoparticle by determining SPR-enhanced light scattering at 543 nm with no photobleaching even after long-term irradiation. Both incubations showed the successful internalization of AuNPs. However, the uptake efficiency seems to be significantly increased by penetratin conjugation. LSCM evidenced the presence of AuNPs in up to 100 % of co-incubated cells if the particles were penetratin-conjugated, while ligand free AuNP were found in approximately half the cells (Figure 6). TEM images underlined this fact. The penetratin conjugation apparently induces a different uptake mechanism: while ligand free AuNPs diffused individually or in small clusters into the cells as also previously observed by Salmaso *et al.* [32], penetratin-conjugated AuNPs are accumulated in vesicles. The size, shape and surface coverage dependency of uptake efficiency and mechanism of laser-generated Au-Pen bioconjugates should be investigated in future.
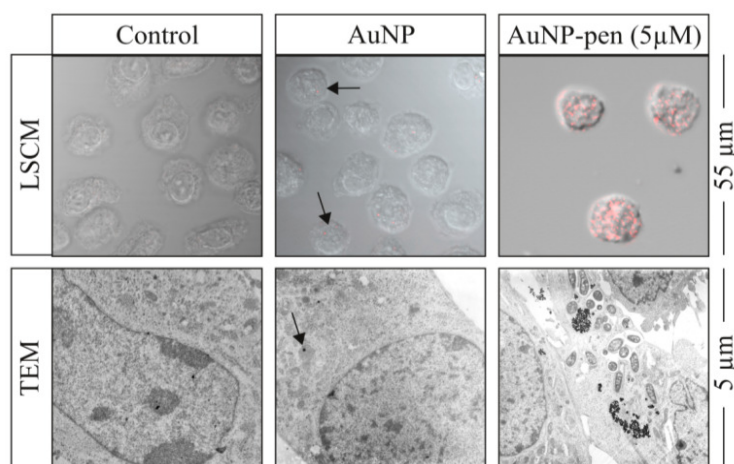

Figure 6.: Influence of penetratin conjugation on cellular AuNP internalization: Representative laser scanning confocal microscopy images (top, red spots represent the backscatter of AuNPs after excitation at 543 nm) and transmission electron microscopy images (bottom) of immortalised bovine endothelial cells (GM7373); from left to right: negative controls, co-incubation with AuNPs and AuNP-penetratin conjugates for 2 h. The bioconjugates were generated by laser ablation in 5 µM penetratin.

Conclusion

In situ conjugation during laser ablation allows the rapid design of cell penetrating nanomarkers. Significantly en-

hanced penetratin conjugation efficiencies could be observed at higher pHs while the design of bioconjugates depends on the peptide concentration during ablation. Thus, AuNPs with different particle and aggregate size and peptide surface coverage could be generated, enabling the correlation of particle morphology and surface coverage with biological activity, i.e., internalization efficiency and mechanism. In a preliminary biological application during the recent work, we could show a successful uptake of AuNP-Pen bioconjugates, generated in 5 µM penetratin for the first time. Up to 100 % of co-incubated cells were marked with penetratin conjugated AuNP within 2 h.

Experimental section
Generation and bioconjugation of gold nanoparticles

Laser generation of gold nanoparticles was carried out using a femtosecond laser system (Spitfire Pro, Spectra-Physics) delivering 120 fs laser pulses at a wavelength of 800 nm (maximum energy: 400 µJ per pulse, beam diameter: 4 mm). The pulse energy and the distance of a 40 mm lens to the target's surface, referred to focal position, were fixed to 100 µJ and -1 mm at a repetition rate of 5 kHz. The focus in air is defined as the 0 focal position. The principle set-up is described as follows: A 5x5 mm gold foil (thickness: 0.1 µm, purity>99.99 %; Goodfellow GmbH) thoroughly cleaned, was placed on the bottom in a well of a 48-well plate, filled with 500 µL double-distilled aqueous solution (ddH$_2$O) of penetratin (0.0; 0.1, 0.5; 1; 5; 7.5 and 20 µM) (Scheme 1). The activated penetratin ((Ac)NPys-CRQIKIWFQNRRMKWKK(Ac)), featuring a pyridyl disulfide (NPys) function at its N-terminal end with high affinity towards gold was purchased at MP Biomedicals. As it has been previously reported that it is not necessary to disrupt the disulfide bond with a reducing agent to get self-assembly processes onto gold substrates [26], the peptide was directly added to the ablation medium prior to the laser process. The well plate was then placed on an axis-system that moved at a constant speed of 1 mms^{-1} in a spiral with outer radius of 1 mm and inner radius of 0.4 mm. Time of irradiation was fixed to 53 s (corresponding to one spiral).

Bioconjugate characterization

Zetapotential measurements were performed with the Zetasizer ZS (Malvern). Typically 200 µL of the colloid were added to 800 µL water and the resulting dilution was injected into the electrophoretic cell. Three consecutive measurements were carried out and mean values are presented.

The conjugation efficiency was evaluated by the percentage of the total amount of peptide conjugated to AuNP. Therefore the amount of unconjugated penetratin was measured by UV-Vis spectroscopy (Shimadzu 1650) at 280 nm after separation of bioconjugates from remaining
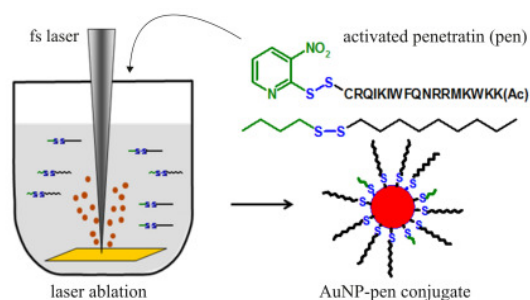
Scheme 1.: *In situ* bioconjugation of AuNPs with the cell penetrating peptide penetratin during laser ablation in liquids

unconjugated penetratin by centrifugation for 30 min at 40.000 g. Intensities were converted to molar concentrations by interpolation from a linear standard calibration curve. Standard curves were prepared with known concentrations of penetratin.

The average number of penetratin per AuNP was obtained by dividing the penetratin concentration, deduced by taking the difference of the total and the measured peptide concentration in the supernatant, by the original AuNP concentration. Normalized surface coverage values were then calculated by dividing the estimated particle surface area (assuming spherical particles) in the nanoparticle suspension.

MALDI-TOF of conjugates was performed at Stiftung Tierärztliche Hochschule, Rinderklinik (Prof. Dr. H. Bollwein, Dr. M. Ekhlase-Hundrieser) with Kratos Kompact MALDI 2. One microliter of α-cyano-4-hydroxycinnamic acid matrix was mixed with 1 µL of the sample and dried prior to analysis.

UV-Vis spectra of the colloidal solutions were recorded in the spectral region 230-800 nm (Shimadzu 1650).

All transmission electron micrographs were registered at Stiftung Tierärztliche Hochschule, Institut für Pathologie (Prof. Dr. W. Baumgärtner, Kerstin Rohn) utilizing an EM10 C electron microscope. In case of the colloidal solution one drop was placed on a carbon coated, formvar covered copper grid and dried at room temperature. Given diameters are averaged over at least 500 AuNPs. The form factor (FF) is calculated by the following equation, $FF= 4\pi A/p^2$ where A is the area and p the perimeter of each AuNP.

Cell culture and co-incubation with nanoparticles

The cells used in the studies were derived from a bovine immortalized endothelial cell line (GM7373 [33]), obtained from the Cell culture Collection, Institute of Infectology, FLI, Riems, Germany). All experiments were carried out in six-well-dishes (TPP AG, Trasadingen, Switzerland). Cells were seeded in Dulbecco's modified Eagle's medium (DMEM; PAA Laboratories GmbH, Pasching, Austria) supplemented with 10 % heat-inactivated fetal bovine serum (Invitrogen, Karlsruhe, Germany) and 1 % penicillin/streptomycin (PAA Laboratories GmbH, Pasching, Austria) and allowed to attach and

grow at 37 °C in a humidified 5 % CO_2 atmosphere. After 24 hours new medium was added, this time however lacking the antibiotics. Following another 24 hours the medium was replaced again by DMEM alone or DMEM including AuNPs with or without Penetratin in a final concentration of 50 µM Au and then incubated for further 2 hours. All experiments were carried out in duplicates and repeated three times.

Cell preparation for LSCM-analysis
Generally cell preparation for LSCM corresponded to previously described trials [34]. In short, after detachment and fixation in 0.5 % paraformaldehyde (Merck KGaA, Darmstadt, Germany) cells were mixed 1:4 with Vectashield (Vector Laboratories Inc., Burlingame, USA) and mounted on a slide within a paper reinforcement ring, in order not to flatten the cells by the subsequently placed cover slip, which was fixed onto the slide with nail varnish. Visualization by LSCM was performed using an Axioplan 200 and a confocal imaging system LSM510 (Carl Zeiss MicroImaging GmbH, Jena, Germany) within the spectrum of visible light. A Helium-Neon-Green laser of 543 nm was used to excite the surface plasmon resonance of the gold nanoparticles.

Cell preparation for TEM analysis
Cells to be used for TEM examinations were not detached but fixed adhered to the bottom of the six-well-dishes with the aid of 2 ml of 2 % glutaraldehyde (Sigma Aldrich, Schnelldorf, Germany) in Dulbecco's Phosphate-buffered Saline (PBS; Sigma-Aldrich Chemie GmbH, Steinheim, Germany), in which they remained at 4 °C until further processing. The thus fixed cells were prepared for electron microscopy essentially as previously described [35] with slight modifications. Briefly, the cell culture was rinsed in 0.1 M cacodylate buffer (pH 7.4), then postfixed in 1 % (v/v) osmium tetraoxide, rinsed again in cacodylate buffer, dehydrated with increasing concentrations of ethanol and subsequently embedded in Epon. The prepared cell layer was trimmed and processed for standard transmission ultrastructural examination.

References

[1] K.T. Thurn, E.M.B. Brown, A. Wu, S. Vogt, B. Lai, J. Maser, T. Paunesku, and G.E. Woloschak. Nanoscale Research Letters. 2:430–441, 2007.

[2] N. Lewinski, V. Colvin, and R. Drezek. Small. 4:26-49, 2008.

[3] K. Sokolov, J. Aaron, B. Hsu, D. Nida, A. Gillenwater, and M. Follen, Technology in Cancer Research and Treatment. 2:491-504, 2003.

[4] S. Link and M. El-Sayed, Journal of Physical Chemistry B. 103:8410-8426, 1999.

[5] L.L. Ma, M.D. Feldman, J.M. Tam, A.S. Paranjape, K.K. Cheruku, T.A. Larson, J.O. Tam, D.R. Ingram, V. Paramita, J.W. Villard, J.T. Jenkins, T. Wang, G.D. Clarke, R. Asmis, K. Sokolov, B. Chandrasekar, T.E. Milner, and K.P. Johnston. ACS Nano. 3:2686–2696, 2009.

[6] a) A.P. Alivisatos, K.P. Johnsson, X. Peng, T.E. Wilson, C.J. Loweth, M.P. Bruchez, and P.G. Schultz. Nature. 382:609-611, 1996. b) C.A. Mirkin, R.L. Letsinger, R.C. Mucic, and J.J. Storhoff. Nature. 382:607-609, 1996.

[7] C.D. Medley, J.E. Smith, Z. Tang, Y. Wu, S. Bamrungsap, and W. Tan. Analytical Chemistry. 80:1067-72, 2008.

[8] A.A. Karyakin, G.V. Presnova, M.Y. Rubtsova, and A.M. Egorov. Analytical Chemistry. 72:3805–3811, 2000.

[9] N.L. Rosi, D.A. Giljohann, C.S. Thaxton, A.K. Lytton-Jean, M.S. Han, and C.A. Mirkin. Science. 312:1027–1030, 2006.

[10] a) B.D. Chithrani, A.A. Ghazani, and W.C.W. Chan. Nano Letters. 6:662-668, 2006. b) H.K. Patra, S. Banerjee, U. Chaudhuri, P. Lahiri, and A.K. Dasgupta. Nanomedicine: Nanotechnology, Biology and Medicine. 3:111-119, 2007. c) R. Shukla, V. Bansal, M. Chaudhary, A. Basu, R.R. Bhonde, and M. Sastry. Langmuir. 21:10644-10654, 2005.

[11] M. Everts, V. Saini, J.L. Leddon, R.J. Kok, M. Stoff-Khalili, M.A. Preuss, C.L. Millican, G. Perkins, J.M. Brown, H. Bagaria, D.E. Nikles, D.T. Johnson, V.P. Zharov, and D.T. Curiel. Nano Letters. 6:587-591, 2006.

[12] X. Shi, S. Wang, S. Meshinchi, M.E. Van Antwerp, X. Bi, I. Lee, and J.R. Baker. Small. 3:1245-1252, 2007.

[13] H. Kobayashi, S. Kawamoto, T. Saga, N. Sato, A. Hiraga, T. Ishimori, J. Konishi, K. Togashi, and M.W. Brechbiel. Magnetic Resonance in Medicine. 46:781-788, 2001.

[14] S. Hacein-Bey-Abina, C. von Kalle, M. Schmidt, F. Le Deist, N. Wulffraat, E. McIntyre I. Radford, J.L. Villeval, C.C. Fraser, M. Cavazzana-Calvo, and A. Fischer. The New England Journal of Medicine. 348:255-256, 2003.

[15] a) M. Green and P. M. Loewenstein. Cell. 55:1179-1188, 1988. b) D. Derossi, A.H. Joliot, G. Chassaing, and A. Prochiantz. Journal Biology and Chemistry. 269:10444-10450, 1994.

[16] a) K.M. Stewart, K.L. Horton, and S.O. Kelley. Organic & Biomolecular Chemistry. 6:2242-2255, 2008. b) J.R. Maiolo, M. Ferrer, and E.A. Ottinger. Biochimica et Biophysica Acta. 1712:161-172, 2005.

[17] A. Astriab-Fischer, D. Sergueev, M. Fischert, B.R. Shaw, and R.L. Juliano. Pharmaceutical Research. 19:744-754, 2002.

[18] a) S. Fawell, J. Seery, Y. Daikh, C. Moore, L.L. Chen, B. Pepinsky, and J. Barosoum, Proceeding of the National Academy of Science. 91:664-668, 1994. b) M. Jain, S.C. Subash, A.P. Singh, G. Vebkatraman, D. Colger, and S.K. Batra. Cancer Research. 17:7840-7846, 2005.

[19] A.G. Tkachenko, H. Xie, Y. Liu, D. Coleman, J. Ryan, W.R. Glomm, M.K. Shipton, S. Franzen, and D.L. Feldheim. Bioconjugate Chemistry. 15:482-490, 2004.

[20] J. M. Fuente and C.C. Berry. Bioconjugate Chemistry. 16:1176-1180, 2005.

[21] S. Petersen and S. Barcikowski. Advanced Functional Materials. 19:1167-1172, 2009.

[22] S. Petersen and S. Barcikowski. Journal of Physical Chemistry C.113:19830-19835, 2009.

[23] J.P. Sylvestre, S. Poulin, A.V. Kabashin, E. Sacher, M. Meunier, and J.H.T. Luong. Journal of Physical Chemistry B. 108:16864-16869, 2004.

[24] N.Cox, in Lehninger Biochemistry, Vol. 4, Springer, Berlin, Germany. Ch. 5, 2009.

[25] H. Muto, K. Yamada, K. Miyajima, and F.J. Mafuné. Journal of Physical Chemistry C. 111:17221-17226, 2007.

[26] W. Lee, D.B. Lee, B.K. Oh, W.H. Lee, and J.W. Choi. Enzyme and Microbial Technology. 35:678-682, 2004.

[27] F. Mafuné, J. Kohno, Y. Takeda, T. Kondow, and H. Sawabe. Journal of Physical Chemistry B. 105:5114-5120, 2001.

[28] F. Mafuné, J. Kohna, Y. Takeda, and T. Kondow, *Journal of the American Chemical Society.* 125:1686-1687, 2003.

[29] E.J. Cox. *Journal of Paleontology.* 1:179–183, 1927. Form factor (FF) = $4\pi A/p^2$; A: area; p: perimeter.

[30] W. Jiang, B.Y.S. Kim, J.T. Rutka, and W.C.W. Chan. *Nature Nanotechnology.* 3:145-150, 2008.

[31] S.H. Lee, K.H. Bae, S.H. Kim, K.R. Lee, and T.G. Park. *International Journal of Pharmaceutics.* 364:94-101, 2008.

[32] S. Salmaso, P. Calicati, V. Amendola, M. Meneghetti, J.P. Magnusson, G. Pasparakis, and C. Alexandre. *Journal of* Materials *Chemistry.* 19:1608-1615, 2009.

[33] G. Schares, J. Meyer, A. Barwald, F.J. Conraths, R. Riebe, W. Bohne, K. Rohn, and M. Peters. *International Journal of Parasitology.* 33:229-234, 2003.

[34] J.B. Grinspan, S.N. Mueller, and E.M. Levine. *Journal of Cellular Physiology.* 114:328-338, 1983.

[35] U. Taylor, S. Klein, S. Petersen, W. Kues, S. Barcikowski, and D. Rath. *Cytometry.* Accepted 2010.

6.   Up-scale of the laser-based bioconjugation

The *in situ* bioconjugation during fs LAL has so far been established in a batch system. This approach evolved as a powerful tool for the simple generation of conjugated AuNPs for biological testing, but when aiming at an industrialization of the process, this approach might have some limitations with regard to NP productivity. Although the ablated mass increases with ablation time, the slope referring to NP productivity is decreasing continuously. This tendency is illustrated in Figure 6.1 at the example of AuNP generation in an aqueous solution of ssO by fs LAL with a pulse energy of 100 µJ at various focal positions (numbers are referred to the determined focal position in air; for further data see Supporting Information A.1). One observes that within ten minutes the ablation rate drops by more than 50 %.
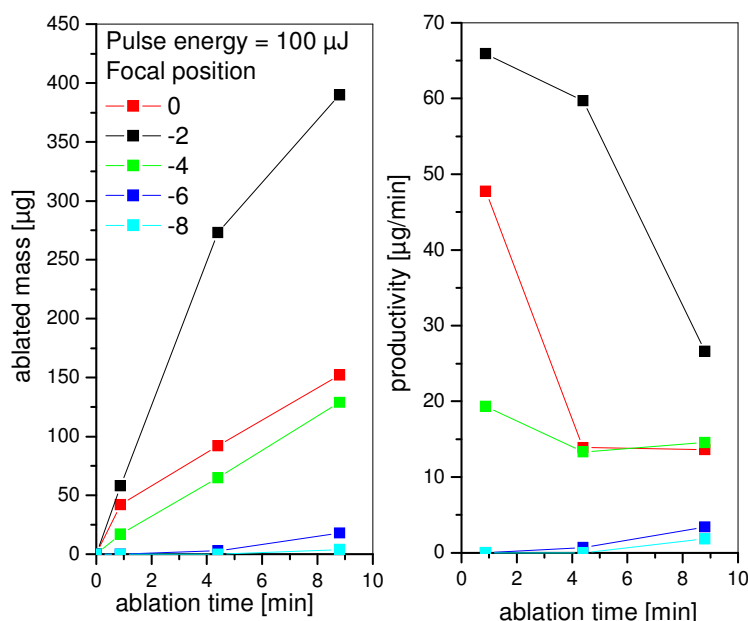
Figure 6.1.: Ablated mass and productivity as function of the ablation time for AuNP generation in an aqueous solution of ssO by fs LAL.

This fact is probably due to light scattering and absorption of AuNPs dispersed in the liquid with incident laser pulses. The resulting shielding effect of the colloidal particles causes the observed continous decrement of ablation efficiency and rate with time. The interference of present AuNPs with laser radiation when reaching a certain threshold intensity, might furthermore provoke the formation of a nanoplasma or even the fragmentation of AuNPs. In dependence of their binding strength and length, the stability/integrity of stabilization or functionalization agents would be possibly also affected.

This risk of degradation should be one major concern especially for *in situ* bioconjugation. Our experiments with AuNP generation by fs LAL in an aqueous ssO solution confirm this assumption. The maximal achieved nanoparticle yield and the degradation rate of ssO follow the same trend as function of the focal position (Figure 6.2). Further proof was given in our own paper, included in the thesis [3], showing a linear correlation of the degradation rate and the maximal NP yield.
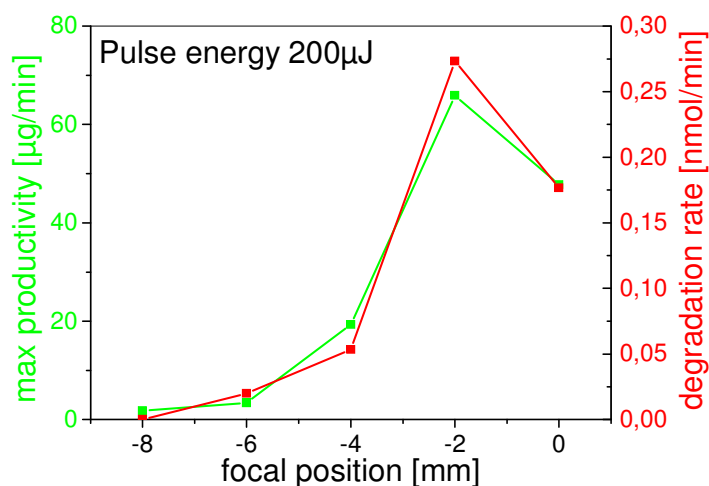
Figure 6.2.: Maximal nanoparticle productivity and degradation rate of ssO in function of the focal position during *in situ* bioconjugation of ssO with AuNPs.

Thus, although the AuNP yield can be generally enhanced by applying higher pulse energies and/or optimized focusing conditions, the applicable conditions for *in situ* bioconjugation during laser ablation are limited by the thermosensitivity of the added biomolecule.

In summary, the absence of high amounts of NPs during *in situ* bioconjugation would probably allow higher ablation efficiencies in general and the application of higher pulse energies, furthermore aiming at higher NP yields. The removal of the NPs from the laser active volume directly after their generation should thus significantly enhance NP production rates. In this context, the paper in chapter 6.1 deals with the application of a flow chamber, providing a liquid flow of biomolecules for the transportation of NPs from their region of generation. SsO served as a model substance in order to compare with previous results (own paper included in the thesis [3]). We observed, that increasing flow rates allowed the application of higher pulse energies without provoking degradation of ssO. Thus the invented flow chamber concept allows higher production rates of AuNPs without risking a reduction in bioconjugate quality.

6.1.   *In situ* bioconjugation in stationary liquid and in liquid flow

Csaba László Sajti, Svea Petersen, Ana Menéndez Manjón, and Stephan Barcikowski

In situ bioconjugation in stationary media and in liquid flow by femtosecond laser ablation

Csaba László Sajti, Svea Petersen, Ana Menéndez-Manjón, and Stephan Barcikowski

Laser Zentrum Hannover e.V., Hannover, Germany

Abstract

In situ functionalization of gold nanoparticles with fluorophore-tagged oligonucleotides is studied by comparing femtosecond laser ablation in stationary liquid and in biomolecule flow. Femtosecond laser pulses induce significant degradation to sensitive biomolecules when ablating gold in a stationary solution of oligonucleotides. Contrarily, *in situ* conjugation of nanoparticles in biomolecule flow considerably reduces the degree of degradation studied by gel electrophoresis and UV-Vis spectrometry. Ablating gold with 100 µJ femtosecond laser pulses DNA sequence does not degrade, while degree of fluorophore tag degradation was 84 % in stationary solution compared to 5 % for 1 mL/min liquid flow. It is concluded that femtosecond laser-induced degradation of biomolecules is triggered by absorption of nanoparticle conjugates suspended in the colloid and not by ablation of the target. Quenching of nanoparticle size appears from 0.5 µM biomolecule concentration for 0.3 µg/s nanoparticle productivity indicating the successful surface functionalization. Finally, increasing liquid flow rate from stationary to 450 mL/min enhances nanoparticle productivity from 0.2 µg/s to 1.5 µg/s, as increasing liquid flow allows removal of light absorbing nanoparticles from the ablation zone, avoiding attenuation of subsequent laser photons.

Introduction

Nanoparticles, especially plasmonic materials such as gold nanoparticles characterized by highly enhanced resonant absorption and scattering properties, are particularly useful in cell-targeted drug delivery [1], high resolution bio-imaging [2,3], biomedical diagnostics and therapeutics [4] when conjugated with functional molecules (e.g., oligonucleotides). During the last decade, a variety of methods for gold nanoparticle preparation have been established. Among these, the standard chemical synthesis is based on the reduction of Au(III) in presence of reducing agents such as citrate [5] or sodium borohydride [6] and stabilizing ligands, while bioconjugation was described by directly adding conjugative agents during the reduction process. These chemical techniques might have a critical drawback involving the use of chemical precursors and reducing agents requiring a purification procedure where residual ligands limit subsequent conjugation.

Pulsed laser ablation in liquids (PLAL) is a recently emerged alternative single step approach enabling size-controlled generation of stable nanoparticle colloids [7-10] with outstanding purity and novel surface chemistry not reproducible by any other conventional manufacturing route. Recently, Sylvestre *et al*. revealed the presence of the oxidation states Au$^+$ and Au^{3+} besides the metallic Au^0 due to partial oxidation of the nanoparticles in aqueous media [9]. Owing to this partial oxidation, laser-generated gold nanoparticles act as electron acceptors; hence, they are easily coordinated by molecules bearing electron donor moieties as thiol, amine or carboxyl groups added to ablation media prior (*in-situ* conjugation) or after (*ex-situ* conjugation) the laser process. However, we recently published that *in-situ* conjugation leads to about four times higher conjugation efficiency than *ex-situ* functionalization [11].

Although ultrashort-pulsed laser present a promising tool for *in situ* bioconjugation, due to minimal thermal impact to ablated material and surrounding media when ablating with laser fluences close to the ablation threshold [12], it has been already shown to induce similar residual thermal effects as nanosecond lasers in the high fluence regime [13]. Furthermore, femtosecond pulses have been already found to melt and photothermally reshape ablated gold nanoparticles in water [14] and also to induce certain degradation to gold conjugates, however the degradation mechanism still remains unclear [15].

In this paper, we describe the *in situ* conjugation of gold nanoparticles with oligonucleotides by ultrashort-pulsed laser ablation in stationary liquid and in a controlled biomolecule flow. Degree of biomolecule degradation was quantitatively investigated and the possible mechanisms of femtosecond laser-induced DNA degradation are discussed and show the trade-off between quality and nanoparticle production rate.

Experimental details
Nanoparticle generation method

Ultrashort PLAL was carried out using a commercial femtosecond laser system (Spitfire Pro, Spectra-Physics) delivering 120 fs laser pulses with 5 kHz repetition rate at a central wavelength of 800 nm. Laser irradiation was focused onto the surface of a 100 µm thick gold foil (Goodfellow GmbH) merged into 4 mm of liquid layer. During nanoparticle generation the ablation chamber was continuously moved with a three axis positioning system (3D Microcac) providing constant lateral speed of 1 mm/s in a spiral ablation pattern.
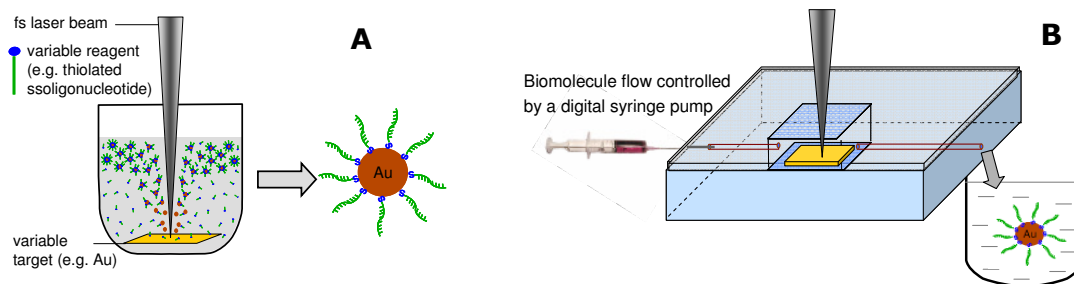
Figure 1.: Schematic illustration of the *in-situ* bioconjugation in (A) stationary liquid and (B) in biomolecule flow by femtosecond laser ablation.

Two experimental concepts were utilized, performing laser ablation in stationary liquid and in biomolecule flow, presented schematically in Figure 1. Ablation in a stationary liquid was performed in a glass vessel filled with 500 µL of aqueous solution (H$_2$O>18 MΩcm, Millipore) of thiolated single stranded oligonucleotides (ssO). In a second experimental arrangement gold nanoparticle ssO conjugates were synthesized in a controlled oligonucleotide flow generated by a digital syringe pump (NE-300, New Era) using a self-constructed flow chamber presented in Figure 1 B.

Characterization techniques
Degree of degradation was investigated by gel electrophoresis and by UV-Vis absorption in the spectral region of 220-800 nm (Shimadzu 1650), of gold nanoparticles functionalized by a thiolated ssO sequence (5'cta-cct-gca-ctg-taa-gca-ctt-tg-3', Mod. 5':C6-Disulfide, Biospring GmbH) and by ssO sequence tagged by Cy5 fluorophore (Cy5-ssO 5'agc-aca-tct-cgg-tcc-ctg-3', Mod. 3' C6-Disulfide, Mod. 5' Cy5, Purimex DNA/RNA Oligonucleotides), respectively. The ablation media after nanoparticle generation were treated with 5 mM aqueous dithithreitol-solution (DTT) to displace surface bound ssO via an exchange reaction and induce nanoparticle aggregation as consequence. This method guarantees that both conjugated and unconjugated ssO are analyzed quantitatively. The ssO containing ablation media were loaded on a 20 % denaturing polyacrylamide gel, run for 3 hours at 300 V and silver stained. To quantify the integrity of ssO after irradiation, we compared the intensity of intact ssO band with the intensity of the ssO band prior to nanoparticle generation. To visualize the bands, gels were stained and developed using Fast*Silver* (G Biosciences, USA). Scans of resulting stained gels were analyzed with Image J software. Biomolecule degradation was also quantified by the Cy5 absorption band at 648 nm by UV-Vis spectrometry. For this purpose, the ablated colloids were first treated by DTT, and in a next step gold nanoparticles were forced to agglomerate by 200 mM aqueous NaCl solution. After 10 minutes of centrifugation at 5000 rpm the absorption spectrum of Cy5-ssO containing supernatant were analyzed. Size measurements were performed by dynamic light scattering (DLS, Zetasizer ZS Malvern Instruments) and by transmission electron microscopy (TEM, EM 10C Zeiss), while nanoparticle production rate was determined by differential weighing of the target by a precision micro-balance (Sartorius M3P) via the estimation that no material was attached on the process chamber wall.
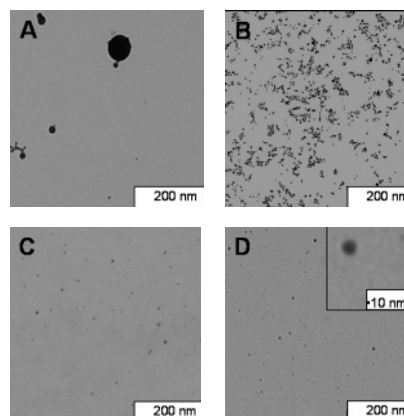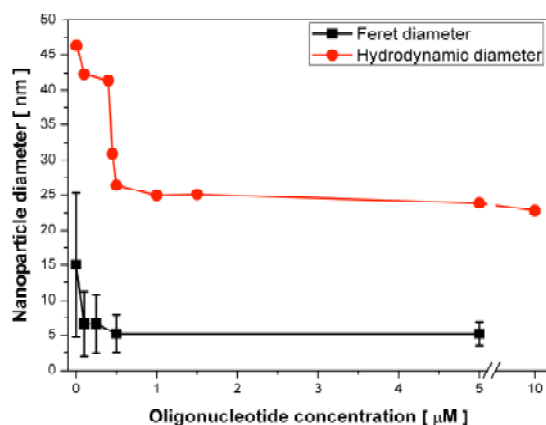
Figure 2.: Influence of oligonucleotide concentration on the hydrodynamic and Feret diameters of laser-generated bioconjugates (left) and TEM images of pure gold nanoparticles (A) and bioconjugates synthesized by 0.1 µM (B), 0.5 µM (C) and by 5 µM (D) biomolecule concentration.
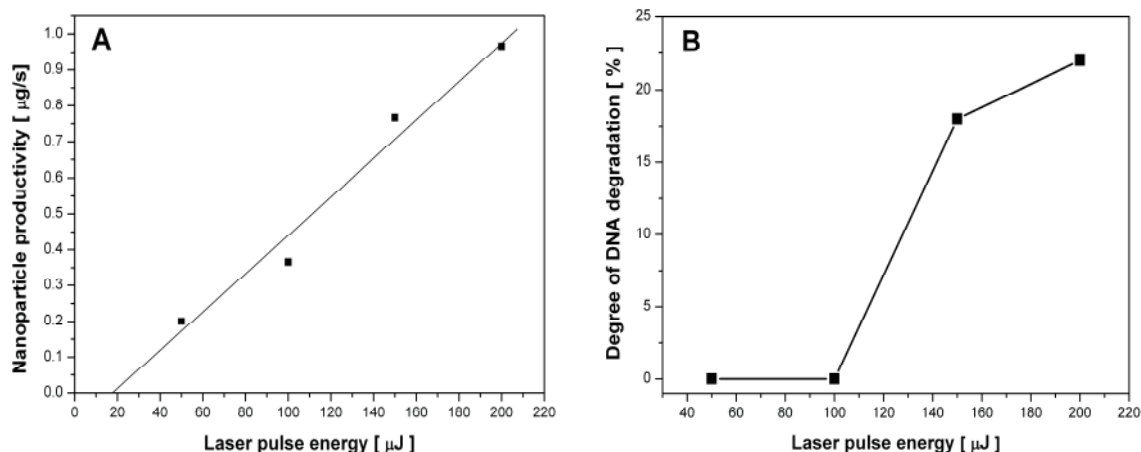
Figure 3.: (A) Gold nanoparticle productivity and (B) corresponding degree of oligonucleotide degradation in function of the focused laser pulse energy determined by gel electrophoresis using 3 µM DNA concentration

Results and discussion

During laser ablation, the ejected material is in a chemically extremely active state of growth and it is well known that nanoparticle size can be significantly influenced by the amount of conjugative agents in solution. Figure 2 A shows the Feret and hydrodynamic diameters of nanoparticle bioconjugates in function of the ssO concentration obtained by 100 µJ of pulse energy in stationary liquid. Reciprocal dependency of primary nanoparticle size on the concentration of ssO was clearly revealed. That is in good agreement with data obtained in a previous study for conjugation with dodecanthiol in hexane [16]. The significant difference between nanoparticle size by TEM and DLS is due to the fact that hydrodynamic size of nanoparticles is strongly affected by the presence of DNA molecules and by solvation of conjugates. It seems that a critical concentration of ssO is required to achieve a significant growth quenching. As the concentration falls below 0.5 µM, agglomerates are detected which could also be visualized by the quotient of the plasmon resonance spectrum at 800 and 380 nm. Ablating with higher ssO concentrations no further size decrease was

observed and a plateau in both Feret and hydrodynamic particle size appeared. TEM micrographs also confirmed this tendency (Figure 2 B).

As known from literature, ablation efficiency and nanoparticle yield increase with pulse energy, although at the same time, heat impact to material and the risk of molecule degradation also increases [17]. Process window of negligible degradation of biomolecules with highest ablation rate have to be identified. We thus examined nanoparticle productivity at focal position with different pulse energies in stationary 3 µM ssO solution and studied oligonucleotide degradation by gel electrophoresis in parallel, shown in Figure 3 A and 3 B, respectively. Nanoparticle productivity increased with pulse energy, reaching 1 µg/s with 200 µJ focused laser pulses corresponding to about 8×10^{11} conjugates per second with average size of 5 nm. This yield is higher than the one obtained by femtosecond PLAL of gold in pure water being only 0.2 µg/s or about 6×10^{9} nanoparticles per second considering an average particle diameter of 15 nm. As published earlier, ablating in water gold nanoparticles tend to redeposit on the target's surface
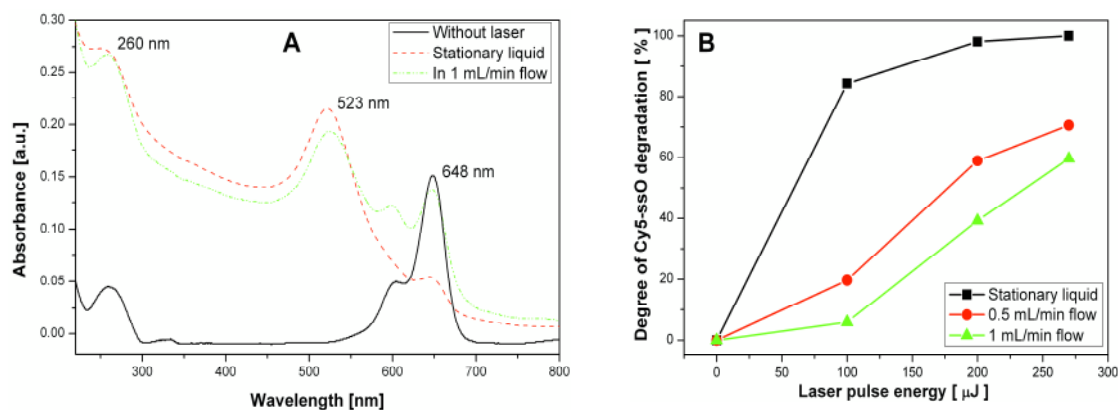
Figure 4.: (A) Absorption spectrum of nanoparticle bioconjugates (DNA ~ 260 nm, gold nanoparticle ~ 523 nm, fluorophore tag ~ 648 nm) ablated with 100 µJ pulse energy in stationary liquid and in biomolecule flow. (B) Degree of Cy5-labeled oligonucleotide degradation at 648 nm in function of laser pulse energy.

after ablation, whilst during *in situ* functionalization they remain in the solution, enhancing production rate of colloidal particles [16]. Besides enhanced ablation rate, degree of oligonucleotide disintegration also increases with pulse energy, presented in Figure 3 B. After one minute of ablation, no degradation of ssO was observed up to 100 µJ focused pulse energy, followed by a rapid increase in photo/thermal-induced cleavage of DNA sequences. Ablation with 200 µJ femtosecond laser pulses causes significant degradation of about 22 %. As already published, activation energy of heat-induced DNA depurination followed by cleavage of nearby phosphor-diesters is 127 kJmol^{-1} [17,18]. We roughly estimated the molar energy density in the vicinity of the focus position to be 6.8 GJcm^{-2}mol^{-1} considering 200 µJ pulse energy, 50 µm focal diameter and 3 µM concentration in a total volume of 500 µL, neglecting the nonlinear absorption cross-section of DNA for 800 nm as it is not yet published. Due to the fact that this high amount of energy is deposited within the time scale faster than the electron phonon coupling, being about 4.7 ps for gold [19], fabricating nanoparticles with femtosecond laser ablation close to the ablation threshold remains a cold process and laser energy seems to be mainly deposited at the gold target.

In order to investigate whether the laser ablation itself, or the presence of nanoparticles trigger biomolecule degradation during femtosecond PLAL, we ablated gold in the presence of 1.5 µM Cy5-tagged ssO with various pulse energies in stationary solution and in biomolecule flow and studied the main absorption peak of Cy5 at 648 nm. Figure 4 A clearly demonstrates the difference between reference biomolecule spectrum and absorption spectra obtained by the two experimental concepts using 100 µJ pulse energy. It was clearly revealed that femtosecond laser ablation in stationary Cy5-ssO media induces drastic degeneration to the fluorophore tag, while ablation in a biomolecule flow with same laser parameters minimizes degradation. In the spectra of bioconjugates, besides the principal peak and by-peak of Cy5 at 648 nm and 604 nm respectively one observes a second band at 260 nm. This transition results from the electronical shifts in purines and pyrimidines contained in the oligonucleotide. Figure 4 B depicts quantitatively the degree of Cy5-labeled oligonucleotide degradation at 648 nm in function of laser pulse energy and liquid flow rate. As expected, degree of degradation reduces considerably with higher flow rates. Since only the total residence time of ablated species in the ablation zone is varied by the liquid flow rate, we assume that biomolecule-fluorophore disintegration by femtosecond laser irradiation is mainly induced and amplified by absorption and scattering of subsequent laser beam on previously ablated, suspended nanoparticles/nanoparticle conjugates in the colloidal solution and not triggered directly by the ablation itself. Applying

100 µJ focused laser pulses for 1 minute, degree of Cy5-ssO degradation was measured to be 84 % for gold ablation in stationary oligonucleotide solution, 20 % using 0.5 mL/min biomolecule flow and only 5 % using 1 mL/min flow rate. Using 1 mL/min of liquid flow, the ablated species are estimated to leave the vicinity of the focal point in the time scale of about a few microseconds, hence faster than the time constant determined by the laser repetition rate (200 µs). We thus assume that not ideal laminar liquid flow results in convection of nanoconjugates into the entire volume of the ablation chamber (about 100 µL), and they might be further reirradiated with subsequent laser pulses, resulting in a small degree of biomolecule degradation.
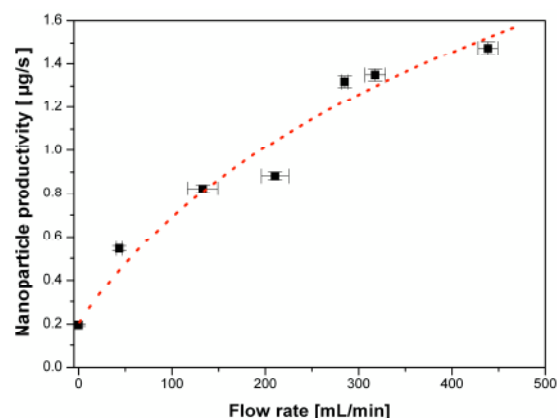
Figure 5.: Gold nanoparticle productivity in water in function of liquid flow velocity using 100 µJ focused laser pulse energy.

Besides the prevention of photo-degradation, increasing liquid flow rate was found to lead to an important rise of nanoparticle productivity using 100 µJ, presented in Figure 5. For this purpose, we utilized a high power peristaltic pump (PD 5001, Heidolph Instruments). Raising liquid flow speed from stationary to 450 mL/min resulted in a significant increase of nanoparticle production rate from 0.2 µg/s to 1.5 µg/s, respectively, while we did not observe significant variation in nanoparticle size and thus assumed that fragmentation might take place under longer post-irradiation times. Ablation rate increased about logarithmically with the outflow velocity and it seems to begin to saturate at 450 mL/min. Without liquid drain/flow, the ablated nanoparticles disperse slowly into the entire liquid. Thus after each ablation sequence a dense particle cloud is ejected characterized by a relatively long residence time in front of the target leading to significant absorption of the subsequent laser pulse.

Conclusion

Femtosecond laser ablation of gold in aqueous solution of thiolated oligonucleotides was established as a powerful single step approach to conjugate oligonucleotide sequences to gold nanoparticles *in situ*. Quenching of nanoparticle size appeared from 0.5 µM biomolecule concentration for 0.3 µg/s nanoparticle productivity

clearly indicating the successful surface functionalization. Quantitative investigation of biomolecule signals by gel electrophoresis and UV-Vis spectrometry of Cy5-tagged oligonucleotides revealed that generation of bioconjugates in stationary liquid is drastically limited by laser pulse energy as significant degradation occurs during ablation. Functionalization of nanoparticle surface in a biomolecule flow with equal laser parameters radically reduces the degree of degradation even for high laser fluences. Ablating gold with 100 µJ focused laser pulse energy, integrity of oligonucleotides was 16 % for stationary and 95 % for 1 mL/min oligonucleotide flow. We assume that femtosecond laser-induced photo-degradation of biomolecules is mainly caused by absorption/scattering of subsequent laser beam by colloidal nanoparticle conjugates. Increasing liquid flow rate from stationary to 450 mL/min allowed the prompt removal of nanoparticles from the ablation zone, resulting in a significant increase of nanoparticle production rate from 0.2 µg/s to 1.5 µg/s, during femtosecond laser ablation in water with 100 µJ laser pulses.

Acknowledgement

References

[1] S. Aryal, J.J. Grailer, S. Pilla, D.A. Steeben, and S. Gong. *Journal of Materials Chemistry.* 19:7879-7884, 2009.

[2] K.T. Yong, M.T. Swihart, H. Ding, and P.N. Prasad. *Plasmonics.* 4:79-93, 2009.

[3] M. Bruchez, M. Moronne, P. Gin, S. Weiss, and A.P. Alivisatos. *Science.* 281:2013-2016, 1998.

[4] I. Brigger, C. Dubernet, and P. Couvreur, *Advanced Drug Delivery Reviews.* 54:631-651, 2002.

[5] J. Turkevich, P.C. Stevenson, and J. Hillier. *Dicussions of the Faraday Society.* 11:55-75, 1951.

[6] M. Brust, M. Walker, D. Bethell. D.J. Schiffrin, and R. Whyman. Journal of the Chemical *Society, Chemical Communications.* 801-802, 1994.

[7] F. Mafunè, J. Kohno, Y. Takeda, and T. Kondow. *Journal of Physical Chemistry B.* 104:9111-9117, 2000.

[8] J.P. Sylvestre, A.V. Kabashin, E. Sacher, and M. Meunier. *Applied Physics A.* 80:753-758, 2005.

[9] J.P. Sylvestre, S. Poulin, A.V. Kabashin, E. Sacher, M. Meunier, and J.H.T. Luong. *Journal of Physical Chemistry B.* 108:16864-16869, 2004.

[10] S. Barcikowski, F. Devesa, and K. Moldenhauer. *Journal of Nanoparticle Research.* 11:1883-1893, 2009.

[11] S. Petersen and S. Barcikowski. *Journal of Physical Chemistry C. 113:19830-19835, 2009.*

[12] B.N. Chichkov, C. Momma, S. Nolte, F. von Alvensleben, and A. Tünnermann. *Applied Physics A.* 63:109-115, 1996.

[13] A.Y. Vorobyev, and, C. Guo, *Journal of Physics: Conference Series* 59:418-423, 2007.

[14] S. Link, C. Burda, B. Nikoobakht, and M.A. El-Sayed. *Journal of Physical Chemistry B.* 104:6152-6163, 2000.

[15] S. Besner, A.V. Kabashin, F.M. Winnik, and M. Meunier. *Journal of Physical Chemistry C.* 113:9526-9531, 2009.

[16] S. Petersen, J. Jakobi, A. Hörtinger, and S. Barcikowski, *Journal of Laser Micro/Nanoengineering* 4:71-74, 2009.

[17] S. Petersen and S. Barcikowski. *Advanced Functional Materials* 19:1167-1172, 2009.

[18] L. Zhang, and, Q. Wu. *Journal of Bioscience and Bioengineering* 30:599-604, 2005.

[19] M. Ligges, I. Rajkovic, P.X. Zhou, O. Posth, C. Hassel, G. Dumpich, and D. von der Linde. *Applied Physics Letter.* 94:101910, 2009.

7. Summary and outlook

Summary

Gold nanomarkers cover a broad range of biomedical applications, including biological sensing and diagnosis, while each of them requires a specific design of the nanosystem. Meeting this demand, the thesis at hand evidences the applicability of femtosecond laser ablation in liquids (fs LAL) for the simple and rapid bioconjugation of gold nanoparticles (AuNPs) with nucleic acids and peptides. Results of bioconjugate and process characterization show how this method can possibly facilitate the required experimental search of an adequate nanoparticle design for each biological purpose. This also includes the investigation of the suitability of laser-generated AuNPs with novel surface chemistry for biomedical applications. Moreover, with regard to industrialization, one possible approach for the upscale of bioconjugation during fs LAL has been presented.

Femtosecond laser ablation of a gold foil in water results in ligand-free, positively charged and therefore electrostatically stabilized AuNPs, representing a new class of nanoparticles for biomedical applications compared to chemically derived AuNPs. The surface chemistry of AuNPs is known to dictate some biomedically relevant properties, as biocompatibility and cellular internalization. Biocompatibility of laser-generated AuNPs towards cells and other biomolecules could be evidenced in this thesis. A co-incubation performed with recombinant eGFP-C1-HMGB1 expression plasmids and subsequent transfection into mammalian cells does not seem to alter the protein expression and the protein functionality (DNA binding), while the presence of AuNPs seems to have a significantly positive effect on the transfection efficiencies. The observed effect was size-dependent: medium-sized AuNPs enhanced transfection efficiency nearly by the factor of 6. Moreover, their co-incubation with cells of a bovine-immortalized cell line seems to impair cell viability only at doses that clearly exceed the amounts needed for the marking of cellular features, as determined by fluorescence activated cell sorting (FACS) analyses as well as immunohistochemical and colorimetric assays. Interestingly, LSCM, proving the known optical properties of AuNPs (high quantum yield, no photobleaching) and TEM analysis indicate the presence of a probably passive non-endocytic cellular membrane translocation. This is contrary to the frequently reported localization of chemically-derived AuNPs in intracellular vesicles. In conclusion, with regard to biocompatibility, visualization and cellular internalization, ligand-free AuNPs produced by fs LAL seem promising candidates to become a new generation of biomarkers.

Their required bioconjugation is achievable *in situ,* i.e., simultaneously to their generation, making fs LAL an interesting approach to bioconjugates for screening purposes. As a first model bioconjugation, the immobilization of thiolated ssO on AuNPs was investigated. In this regard, thiolated ssO were added to an aqueous ablation medium prior to ablating a gold foil by fs LAL. Since the resulting AuNPs act as electron acceptors (Lewis-acid), they are easily coordinated by molecules bearing electron donor moieties (Lewis-base) as NH_2, COOH etc. as most biomolecules do. The introduction of a thiol group gives a higher control of conjugation, as the binding to the AuNP surface will mostly occur by Au-S bonds due to the soft Lewis character of both gold and sulfur. This novel approach was discussed with regard to optimal laser and process parameters, which were evaluated concerning integrity of biomolecules and productivity of NP generation. Results reveal that the synthesis of 20 µg of ssO-functionalized AuNPs, sufficient for one or two biological tests, can be achieved in less than one minute without degradation of ssO, proved by gel electrophoresis. Furthermore, we investigated the applicability of the method for the design of peptide-conjugated AuNPs. The cell penetrating peptide penetratin, featuring a pyridyl disulfide (NPys) function at its N-terminal end with high affinity towards gold was chosen for specific functionalization. Using parameters evaluated before, similar NP productivities were observed and the bioactivity of the conjugates could be evidenced in a preliminary biological application showing a significant increase in uptake efficiency compared to AuNPs, obtained by laser ablation in water. The uptake mechanism is supposed to be of micropinocytotic nature, supported by TEM analysis at different incubation times

Besides biomolecule integrity, the quality of bioconjugates was moreover discussed with regard to bioconjugate size. In this matter, the novel preparation method proved to take advantage of the purity of NPs generated by fs LAL without the use of chemical precursors, and the tendency of dispersed additives to coordinate to embryonic particles quenching their growth. The bioconjugate size hence dependends on the biomolecule concentration present during fs LAL. For ssO, we observed a decrease in NP size with increasing ssO concentration until stabilization was reached at 0.5 µM. For the peptide penetratin, this size quenching effect was also detected, but in this case it was followed by the formation of aggregates, observed for penetratin concentrations higher or equal 5 µM, probably due to a reduction in electrostatic repulsions as combination of negatively charged AuNPs and positively charged penetratin. With even increased penetratin concentrations, the decrease of interparticle spacing in the aggregates and the deformation of spherical primary NPs were determined. This reshaping of primary particles probably results from a laser-induced partial melting and subsequent fusion of AuNPs with low interparticle distances in aggregates. Hence, bioconju-

gates with different degree of aggregation could be generated, which might be of interest for an enhanced cellular internalization.

We also addressed the surface coverage of biomolecules on nanoparticles derived by fs LAL. In both cases (ssO and penetratin) we could show a biomolecule to nanoparticle ratio dependency, allowing the fabrication of bioconjugates with varying degrees of bioactivity. The surface coverage of penetratin on AuNPs was furthermore influenced by the pH of the ablation medium. Higher pH values resulted in increased surface coverages, probably due to the decreased electrostatic attraction of AuNPs and penetratin and the resulting enhanced thiol-mediated binding. For the ssO-conjugated AuNPs obtained by *in situ* bioconjugation, up to five times higher maximal surface coverage values were observed in comparison to AuNPs obtained by conventional CRM and subsequent ligand exchange reaction. An ssO binding in an end-on mechanism via weak covalent thiol-Au bonds was hence proposed with a space capacity dirigism. The observed high surface coverage values provide the AuNPs with one essential prerequisite for biomedical assays, which is the high stability in saline solutions. Moreover, they show that *in situ* bioconjugation during fs LAL is an efficient approach in terms of biomolecule yield. Up to 90 % of the total amount of ssO conjugates to AuNPs resulting in surface coverages of ssO per NP in the range of reported values in the literature. However, it has to be noted that conjugation efficiency seems to be higher during *in situ* conjugation than during *ex situ* conjugation. Activity of NPs (surface activity, kinetic energy, etc.) at the time of conjugation might be different in the two processes, possibly leading to this difference in the strength of interaction. Irrespective of this finding, one could conclude that the high conjugation efficiencies make in situ bioconjugation during fs LAL especially interesting for precious biomolecules.

In this context, we have demonstrated the suitability of laser-ablation-based *in situ* bioconjugation of AuNPs with two different functional aptamers: one DNA aptamer directed against streptavidine and one RNA aptamer directed against PSMA. A high degree of aptamer activity was determined on AuNP surface, which verifies that there is no heat-induced denaturation of the aptamer during LAL. We have proven the functionality of conjugates by three different methods (agglomeration-based assay, dot blot assay, tissue microarray) indicating the broad applicability of aptamer-conjugated AuNPs for analytical applications even in highly demanding bioimaging assays.

In conclusion, the established *in situ* bioconjugation is a fast and simple one-step approach to pure conjugated AuNPs with high conjugation efficiency. Results indicate that this novel approach is applicable to a broad range of biomolecules and even different NP core materials could be envisaged.

NP productivity is satisfactory for research purposes, but a high throughput production of large amounts of bioconjugates is limited by laser pulse energy as higher pulse energies entail significant degradation of added biomolecules during ablation. As we could show that biomolecule degradation is even more enhanced in the presence of AuNPs, we assumed that functionalization of AuNPs in a biomolecule flow represents an alternative approach, enabling higher NP productivities without compromising bioconjugate quality. Depending on the pulse energy and the flow rate, we could thus decrease degradation by up to 83 %. This allows the use of higher pulse energies, resulting in increased NP productivities, which might be furthermore enhanced by the flow itself, reducing the shielding of the laser beam by present AuNPs.

Outlook

The *in situ* bioconjugation during LAL has been well established and characterized for the fabrication of AuNPs conjugated to either NAs or peptides. But some biomedical applications would demand the functionalization of NPs by more than one molecule. Two approaches aiming at least multifunctional nanoparticle bioconjugates are conceivable by the established batch process. One could for example simply add all functional molecules to the ablation medium prior to the laser process. If the added molecules have a similar affinity to gold, obtainable surface coverages should theoretically be dictated by their concentration ratio. But similar affinity demands similar molecules, which is probably not often the case. It is more likely that one functional molecule has a higher affinity to gold than the other. As consequence, it will preferentially coordinate to gold and obtainable surface coverages are arduous to predict. The second approach involves a subsequent *ex situ* conjugation after *in situ* conjugation. Taking the example of ssO and peptide conjugation, ssO could be added to the ablation medium prior to the laser process at a concentration allowing NP size stabilization at an average surface coverage. Due to our results, an ssO to AuNP ratio of 20 results in size-stabilized bioconjugates with a surface coverage of one-fifth of the maximum. Hence, 80 % of the surface would in theory still be available for peptide *ex situ* conjugation. For this approach it might be of advantage if the more affine molecule is used during *in situ* conjugation in order to reduce the risk of ligand exchange during *ex situ* conjugation.

However, as we could already show in the last part of the thesis that *in situ* bioconjugation during LAL in liquid flow allows higher production rates compared to the batch system, multifunctionalization might be also envisaged in this reactor design. One can imagine adding several biomolecules by separated channels before and after the generation (Figure 7.1).

A further improvement of this approach with regard to NP productivity would be the addition of one or more biomolecules via one or more channels after NP generation. Thus none of the biomolecules will cross the laser-active volume and the risk of degradation should be negligible as consequence. However, injecting the biomolecule solution(s) after NP generation would demand an exact knowledge of the time scale of NP growth and aggregation. For instance, when injecting too late, the obtained NP size distribution is possibly broader than the one obtainable by *in situ* bioconjugation. But from a different point of view, this channel-assembly might also help in resolving time scales of NP growth and aggregation.

This approach could possibly allow real high throughput bioconjugate fabrication. The applicable pulse energy will then be limited by the laser system itself. Having in mind the actual power limit of fs lasers at around 400 W (for comparison: the average power of the applied laser system during this thesis is 2 W), one could imagine the so far unused potential.
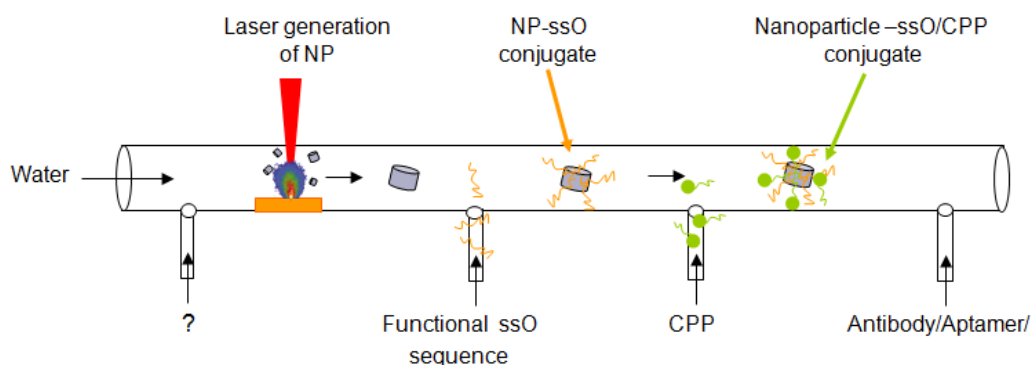
Figure 7.1.: Concept of multifunctionalization of laser-generated NP in liquid flow. [Own Patent: Verfahren und Vorrichtung zur Herstellung metallhaltiger organischer Verbindungen, PCT/EP2009/059116 (July 15th 2009)]

Annex

A.   Supporting Information

A.1.   *In situ* bioconjugation - Single step approach to tailored na-
noparticle bioconjugates by ultrashort-pulsed laser ablation

Chemicals

Chemicals were purchased from Fluka Chemie AG (D-82024 Taufkirchen), Merck KGaA (D-64271 Darmstadt) and Sigma-Aldrich Chemie GmbH (D-89555 Steinheim). The oligonucleotide 5'cta-cct-gca-ctg-taa-gca-ctt-tg-3', Mod. 5':C6-Disulfide was purchased from Biospring GmbH (D-60386 Frankfurt am Main) and the gold foil (thickness: 0.1 μm, purity >99.99%) from Goodfellow GmbH (D-61213 Bad Nauheim). Oligonucleotides omitted the treatment with dithiothreitol (DTT) prior to conjugation, which is usually carried out to ensure that the thiol modified oligonucleotide is in a mono-thiol form rather than disulfide when applied to nanoparticles. Dougan *et al.* have observed that the conjugation process is even improved when using alkyl-thiolated oligonucleotides as there is no trade off in conjugate stability or surface coverage as a result of omitting reduction with DTT [1].

Generation Method

Laser generation of gold nanoparticles was carried out using a femtosecond laser system (Spitfire Pro, Spectra-Physics) delivering 120 fs laser pulses at a wavelength of 800 nm (maximum energy: 400μJ per pulse, beam diameter: 4 mm). If not indicated differently, the pulse energy and the distance of a 40 mm lens to the target's surface, referred to focal position, were fixed to 100 μJ and -2 mm at a repetition rate of 5 kHz due to the degradation and stabilization yield determinations. The focus in air is defined as the 0 focal position. The principle set-up is described as follows: A 5x5 mm gold foil, thoroughly cleaned, was placed on the bottom of a petri dish filled with 500 μL of a 3 μM aqueous solution of single stranded oligonucleotide (H_2O>18 MΩcm, ssO: 5'cta-cct-gca-ctg-taa-gca-ctt-tg-3', Mod. 5':C6-Disulfide). The depth of the layer above the target was 1 cm. The plate was placed on an axis-system, that moved at a constant speed of 1 mms^{-1} in a spiral with outer radius of 1 mm and inner radius of 0.4 mm. Time of irradiation was fixed to 53 s (corresponding to one spriral) if not indicated differently. Further durations explored in degradation and stabilization yield determination were

264 s (corresponding to 5 spirals) and 528 s (corresponding to 10 spirals). The fluence was estimated being the same as in air.

Characterization methods

UV-Vis Spectra of the colloidal solutions were recorded in the spectral region 230-800 nm, with a Shimadzu 1650.

Analytical Ultracentrifugation data were collected on a Beckmann XL-A 4-Loch Rotor An60Ti analytical ultracentrifuge using the vendor's software. Sedimentation velocity experiments were performed at 20°C with angular velocities of 1600 rpm for unconjugated probes and a gradient from 1600 rpm to 50000 rpm for conjugated probes. The concentration of the probes was adjusted to an absorbance of 0.8 at 520 nm. Scans were taken every 6 min for up to 120 scans and data were parameterized via equation S1

$$c(s) = c \frac{\ln(\frac{x}{x_m})}{t\omega^2} \qquad \text{(Eqn S1.)}$$

The size distribution can then be deduced via equation S2:

$$S = \frac{m(1 - \bar{\upsilon}\rho_s)}{6\pi\eta_s rf} \qquad m = \frac{4}{3}\pi r^3 \rho \qquad \text{(Eqn S2.)}$$

where m is particle mass, $\bar{\upsilon}$ is the partial specific volume of the particle, ρ_s is the density of the solvent, η_s is the viscosity of the solvent, r is the radius of the particle and f is the frictional coefficient (f=1 due to TEM analysis)

A transmission electron microscope (TEM Philips CM30) with 0.23 nm point to point resolution was used to obtain micrographs of the colloids. Samples were prepared by placing a drop of solution on a carbon coated, formvar-covered copper grid, and dried at room temperature. The diameter of 700 particles was measured to obtain the particle size distribution.

Dynamic Light Scattering and ζ-potential measurements were performed with the Zetasizer ZS (Malvern). Typically 200 µL of the colloid were added to 800 µL water and the resulting dilution was injected into the cuvette or the electrophoretic cell respectively. Three consecutive measurements are carried out and mean values are presented. For the determination of the stabilization yield the gold foils were weighed three times prior and after ablation on a Sartorius balance (resolution: 1 µg). Mean Values are presented.

Degradation studies

Conjugates were generated following the generation method. Various pulse energies (50 µJ, 100 µJ, 150 µJ, 200 µJ) and focal positions (0, -2 mm, -4 mm, -6 mm, -8 mm) were applied. The irradiation time was increased from 53 s to 264 s to 528 s. The media were then analyzed by gel electrophoresis. For 20% gels, 20 mL of an acrylamide/bis-acrylamide (37.5:1) solution was mixed with 14.4 g urea and 2.5 mL 10xTBE buffer. The mixture was heated above 37 °C to dissolve the urea. 7.5 ml water, 150 µL 10 % ammonium persulfate and 75 µL tetramethylethylendiamin were added. The mixture was swirled and then immediately poured in a gel tray (Maxi (20x20 cm) CTV400, VWR) and let to polymerize for 2 hours. For gel electrophoresis experiments 90 µL of the ablation media after nanoparticle generation were treated with 10 µL of a 100 mM aqueous DTT-solution for 2 hours. DTT was used to rapidly displace the surface bound oligonucleotides via an exchange reaction and induce nanoparticle aggregation as consequence. This method guarantees that conjugated and unconjugated oligonucleotides are analyzed by gel electrophoresis. To ensure that all nanoparticulate sediment was separated from the supernatant, the samples were centrifuged 30 min at 15000 rpm and further work was carried out with 50 µL of the supernatant. To denature the oligonucleotides 10 µL of formamide was added and the mixture was heated 2 min at 95 °C. 20 µL of a loading buffer containing 75 % glycerol, 0.125 % bromphenol blue and 0.125 % xylene cyanole was added. The references, containing the same concentration of oligonucleotide, omitted the laser irradiation and were treated equally before gel electrophoresis and run with the samples on each gel. 10 µl of sample was loaded in each well. Gels were run 3 hours at 300 V in 1xTBE buffer (pH around 8.3 - 8.5). To visualize the bands on the gel after gel electrophoresis, gels were fixed in 30 % EtOH, 10 % glacial acid for 30 min. After thoroughly rinsing, the gels were stained and developed using Fast*Silver*™ (G Biosciences, USA). Detection limit is 0.3 ng (123 ng on gel equal 100 % integrity). Scans of resulting stained gels were analyzed with Image J. The intensity of the bands $I(x)$ was compared to the references $I(0)$ in order to deduce the degree of degraded biomolecule by equation S3.

Deg (x) = 1- I(x)/ I(0)   (Eqn. S3.)

Determined values are then indicated in percentage. In each conjugation experiment 1.5 nmol are in solution, which allows the calculation of intact amount of oligonucleotide after laser irradiation. The decrement in oligonucleotide in nmol/min is calculated via a fit of the degree of degradation in function of time: degree of degradation $(t)= 1-\exp(t/\tau)$, where $1/\tau$ represents the decrement in oligonucleotides.

Table S1.: Summary of degradation experiments.

pulse energy	focal position	degree of integrity						decrement in ssO
		53s		264s		528s		
[µJ]	[mm]	[%]	[nmol]	[%]	[nmol]	[%]	[nmol]	[nmol/min]
50	0	100	1.50	95	1.43	68	1.02	0.05
50	-2	100	1.50	90	1.35	65	0.98	0.06
50	-4	100	1.50	100	1.50	100	1.50	0.00
50	-6	100	1.50	100	1.50	100	1.50	0.00
50	-8	100	1.50	100	1.50	100	1.50	0.00
100	0	100	1.50	94	1.41	67	1.01	0.05
100	-2	100	1.50	73	1.10	58	0.87	0.10
100	-4	100	1.50	100	1.50	100	1.50	0.00
100	-6	100	1.50	100	1.50	100	1.50	0.00
100	-8	100	1.50	100	1.50	100	1.50	0.00
150	0	95	1.43	97	1.46	62	0.93	0.06
150	-2	82	1.23	58	0.87	31	0.47	0.20
150	-4	88	1.32	79	1.19	70	1.05	0.07
150	-6	100	1.50	100	1.50	100	1.50	0.00
150	-8	100	1.50	100	1.50	100	1.50	0.00
200	0	88	1.32	50	0.75	44	0.66	0.18
200	-2	78	1.17	37	0.56	30	0.45	0.27
200	-4	100	1.50	94	1.41	68	1.02	0.05
200	-6	96	1.44	100	1.50	86	1.29	0.02
200	-8	100	1.50	100	1.50	100	1.50	0.00

Stabilization yield determination

The ablated mass was determined as indicated in the characterization methods.
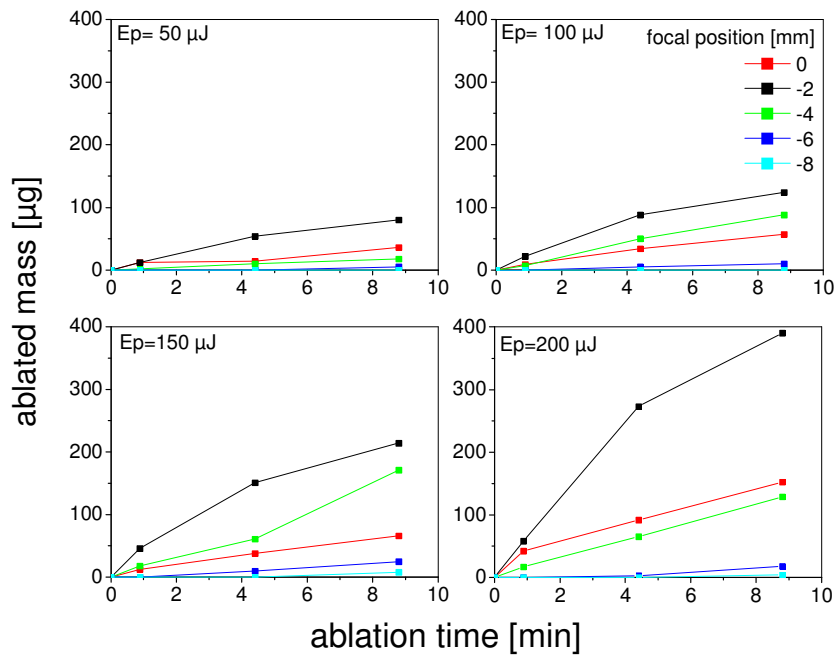
Figure S1.: Ablated mass in function of time, focal position and pulse energy (Ep) for bioconjugates.
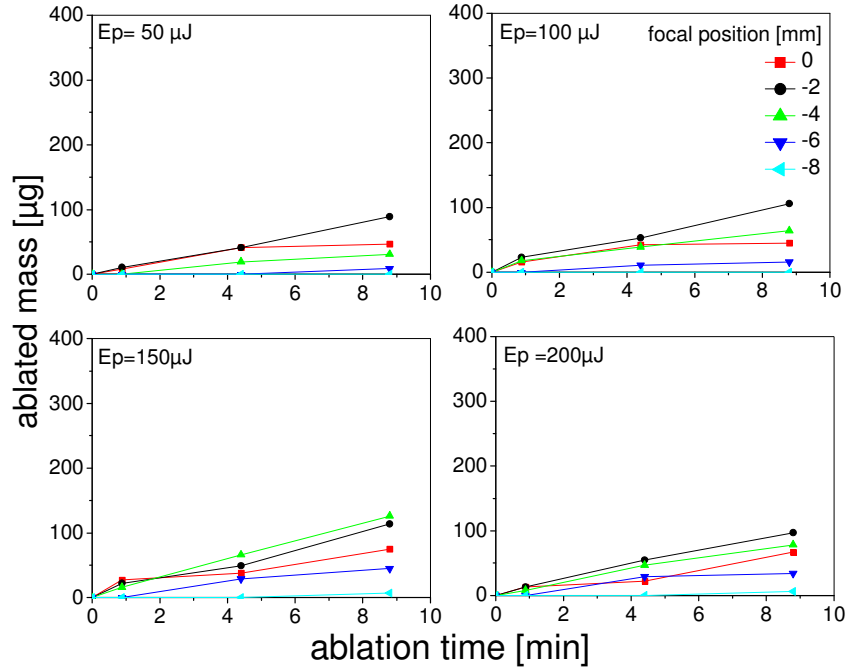
Figure S2.: Ablated mass in function of time, focal position and pulse energy (Ep) for unconjugated gold nanoparticles (Au NP).

The stabilization yield was calculated by taking the means of the ablated mass per time intervals.

Annex

Table S2.: Ablation mass values and calculated stabilization yields for conjugates and AuNP.

Ep	Foc	ablated mass [µg]						stabilization yield [µg/min]	
		53s		264s		528s		conjugates	
[µJ]	[mm]	conjugates		conjugates		conjugates		conjugates	
			AuNP		AuNP		AuNP		AuNP
50	0	12	8	14	41	36	47	6.40	6.61
50	-2	12	11	54	41	80	89	10.40	10.64
50	-4	2	0	10	19	18	31	2.10	2.35
50	-6	0	0	0	0	5	9	0.38	0.34
50	-8	0	0	0	0	0	0	0.00	0.00
100	0	9	16	34	42	57	45	7.47	10.23
100	-2	22	23	88	53	124	106	17.17	15.57
100	-4	7	18	50	39	88	64	9.51	10.70
100	-6	0	0	5	11	10	16	0.76	1.21
100	-8	0	0	0	0	0	0	0.00	0.00
150	0	12	27	38	38	66	75	9.07	14.07
150	-2	46	22	151	49	214	114	31.92	15.81
150	-4	18	16	61	66	171	126	19.13	15.34
150	-6	0	0	10	29	25	45	1.36	3.97
150	-8	0	0	0	0	8	7	0.61	0.27
200	0	42	13	92	22	152	67	25.08	9.19
200	-2	58	13	273	55	390	97	50.74	12.08
200	-4	17	8	65	47	129	78	15.73	9.07
200	-6	0	0	3	29	18	34	1.36	2.58
200	-8	0	0	0	0	4	6	0.61	0.23

Ep: pulse energy; Foc.: focal position

When comparing the stabilization yields, one observes no significant difference for the pulse energies of 50 µJ and 100 µJ. A look at higher pulse energies reveals an increase in the stabilization yield of conjugates.

Sizes

The size distributions have been determined by DLS, AUZ and TEM (see Characterization methods).
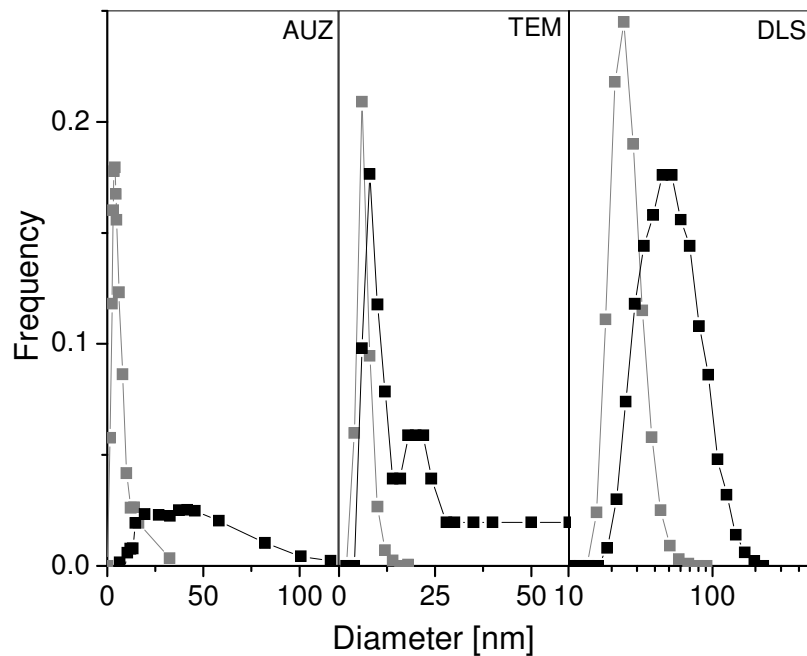
Figure S3.: Size distributions for conjugates and AU-NP by three independent techniques (AUZ, TEM, DLS).
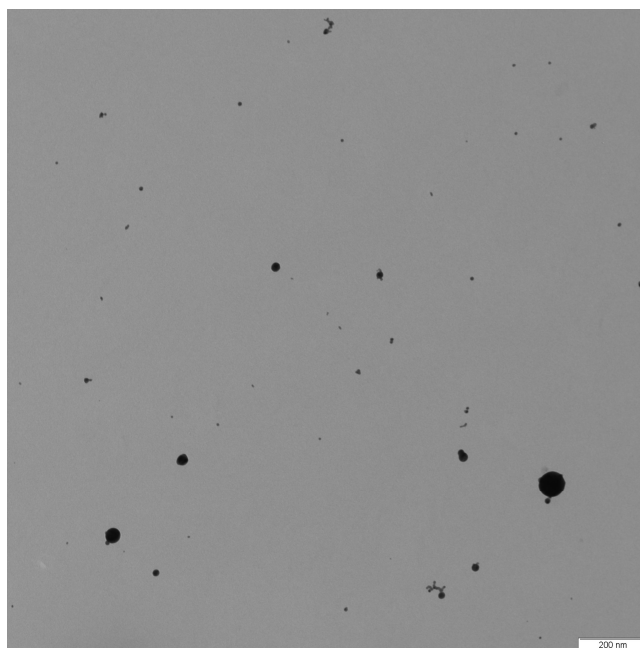
Figure S4.: TEM micrograph of unconjugated gold nanoparticles.

Concentration dependency of the growth quenching

The laser generation was carried out in different concentrations of oligonucleotide: 10 µM, 5 µM, 1.5µM, 1 µM, 0.5 µM, 0.45 µM, 0.4 µM, 0.1 µM, 0.01 µM and 0 µM. The hydrodynamic diameter was determined by DLS measurements.
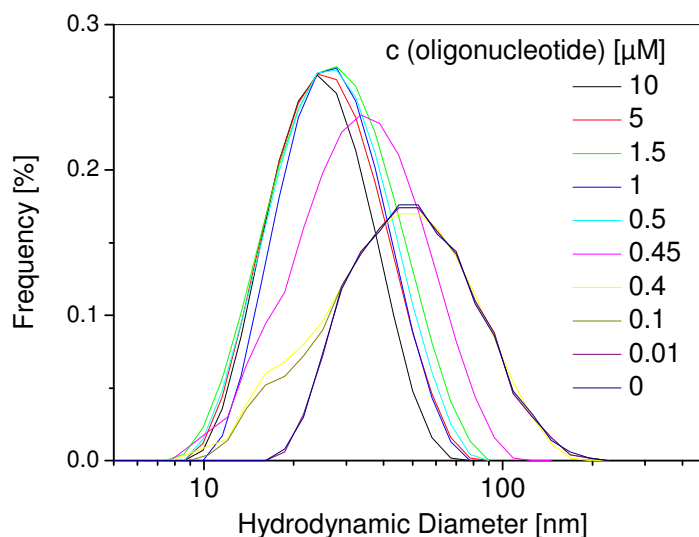
Figure S5.: Oligonucleotide concentration dependency of the size distribution.

Table S3.: d_{50} and d_{90} values at differnet oligonucleotide concentrations.

oligonucleotide concentration [µM]	10	5	1.5	1	0.5	0.45	0.4	0.1	0.01	0
d_{50} [nm]	22.76	23.79	25.08	24.95	26.37	30.94	41.4	42.32	46.31	46.29
d_{90} [nm]	36.9	41.18	45.36	41.45	43.84	56.47	82.29	83.38	86.52	86.89

The size quenching effect due to conjugation can be observed at a concentration above 0.5 µM of oligonucleotide. At lower concentrations particles adopt the size range of unconjugated probes.

Controllability of the hydrodynamic diameter

Conjugates were generated following the generation method, varying the focal position (0,-2 mm, -4 mm, -6 mm) and the pulse energy (50 µJ, 100 µJ, 150 µJ, 200 µJ). The resulting size of conjugates was determined by DLS.

Table S4.: Dependency of the diameter on the laser fluence and focal position.

Focal position	Fluence	Hydrodynamic diameter (d_{50})
[mm]	[J/cm^2]	[nm]
0	1001.80	34.04
0	751.30	32.76
0	500.89	31.20
0	250.45	33.48
-2	0.62	23.68
-2	0.47	24.04
-2	0.30	24.00
-2	0.16	26.24
-4	0.156	23.00
-4	0.12	23.12
-4	0.08	21.32
-4	0.04	17.92
-6	0.07	20.04
-6	0.05	20.72
-6	0.03	15.48
-6	0.02	13.24

Stability in saline solutions

The laser generation was carried out in 5 µM oligonucleotide following the instruction in the generation method. 5M NaCl was added at intervals increasing the salt concentration by 0.05 M increments to a final concentration of 2 M.
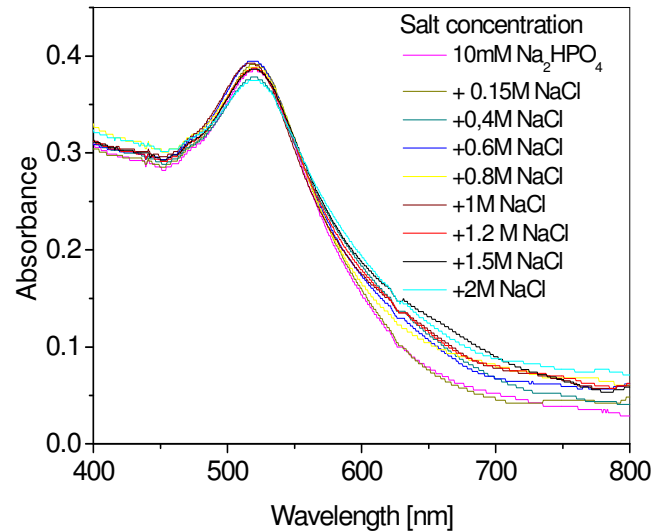
Figure S6.: UV-Vis spectra of conjugates in different saline solutions.

The conjugates are stable in saline solutions. With increasing salt concentrations the absorbance in the region 600-800 nm is increased indicating agglomerates in solution. We used the transfection buffer Eppendorf Hypoosmolar Electroporation Buffer (PH) no.: 4308 070.501 for stability assays.

References

[1] J.A. Dougan, C. Karlsson, W.E. Smith, and D. Graham. *Nucleic Acid Research* 35:3668-3675, 2007.

A.2. Conjugation efficiency of the laser based bioconjugation of gold nanoparticles with nucleic acids

Nanoparticle Characterization

Transmission electron microscopy was used to determine the size distribution of resulting nanoparticles. Samples for TEM analysis were prepared by placing a drop of nanoparticle dispersion, as obtained by laser ablation, on a carbon coated, formvar-covered copper grid, and dried at room temperature. At least 500 nanoparticles were sized from TEM micrographs, which revealed three significantly different size distributions in dependance of the ssO concentration (Figure S1).
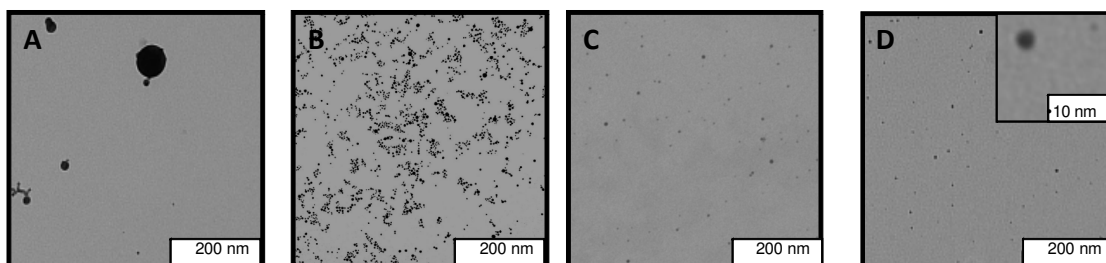
Figure S1.: TEM analysis of nanoparticles generated in increasing thiolated oligonucleotide (HS-ssO) concentrations (A) no ssO, (B) 0.1 µM ssO, (C) 0.5 µM ssO, (D) 5 µM ssO.

One observes a size quenching with increasing HS-ssO concentrations, which reaches its maximum at 0.5 µM (Figure S2). The average diameter of a typical particle preparation at HS-ssO concentrations higher than or equal to 0.5 µM is 5.0 ± 1.3 nm. An HS-ssO concentration of 0.1 µM and 0.25 µM results in slightly bigger nanoparticles with an average diameter of 5.7 ± 3.4 nm. No significant difference was observed in the size of nanoparticles generated in 0.1 and 0.25 µM. Generation of gold nanoparticles in water leads to the typical broad distribution with an average Feret diameter of 15.0 ± 10.3 nm (Figure S1 A), as there is no competition between growth and surface coating.
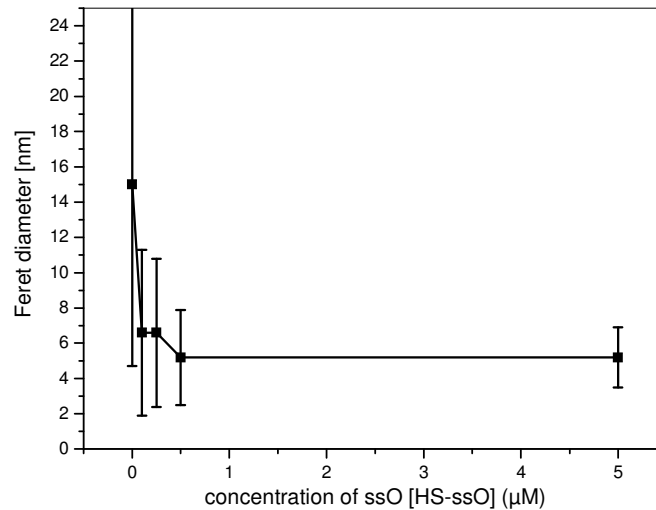
Figure S2.: Average Feret diameter of laser generated gold nanoparticles as function of the added oligonucleotide concentration.

Number, mass and surface-weighed size distributions of the three different kinds of nanoparticles are displayed in Figure S3. While the mass weighted size distribution is applied for the calculation of molar nanoparticle concentrations, the surface weighted distribution is used for the determination of surface coverages.
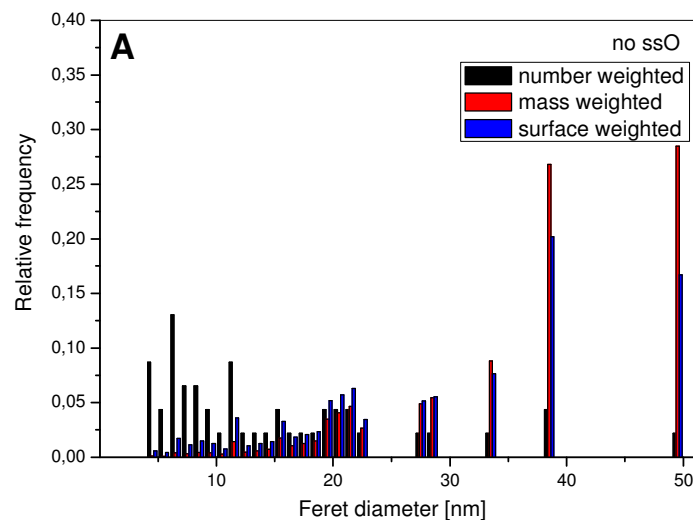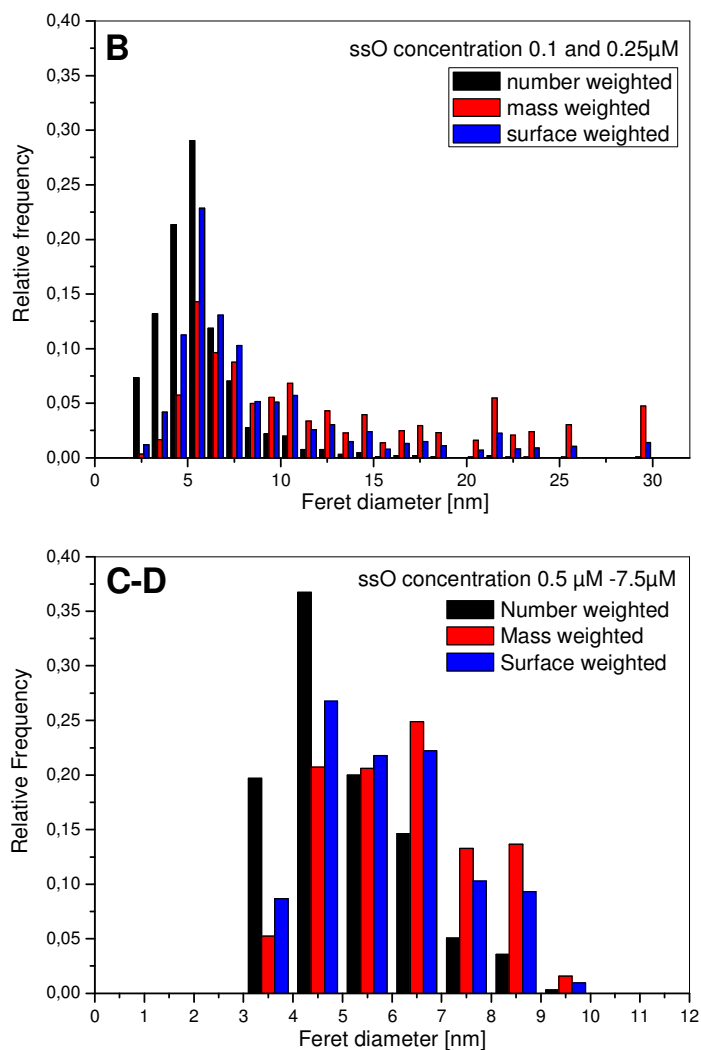
Figure S3.: Number, mass and surface weighted size distributions of nanoparticles generated in increasing oligonucleotide concentrations (A: no ssO, B: 0.1 μM; 0.25 μM ssO, C: 0.5 μM ssO; D: 5 μM ssO).

Calculated average particle masses and surface areas are shown in Table S1.

Table S1.: Average particle mass and average particle surface area

	Average particle mass [g]	Average particle surface [cm^2]
In situ conjugation (ssO ≥ 0.5μM)	1.54E-18	8.36E-13
In situ conjugation (ssO < 0.5 μM)	3.47E-18	12.17E-13
Ex situ conjugation	94.50E-18	101.34E-13

UV-Vis spectroscopy, performed with a Shimadzu 1650 confirms the broader size distribution of gold nanoparticles generated in water compared to bioconjugates.
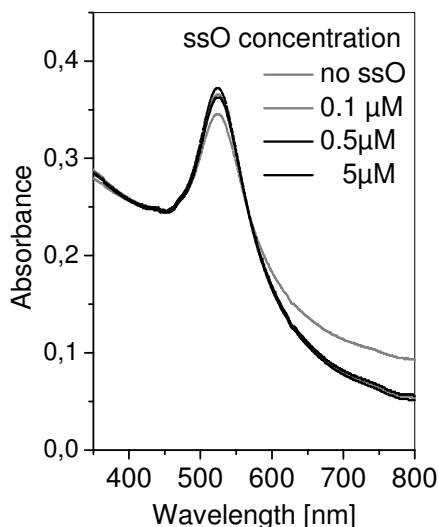
Figure S4.: UV-Vis spectroscopy of gold nanoparticles generated by laser ablation in different ssO concentrations.

Nanoparticle mass was controlled via weighing the target before and after each ablation process. The resolution of the balance reaches down to 1 µg, which results in a measurement error in nanoparticle concentration of 4 µgmL^{-1}, as we deal with mass differences. Since this fact has an equal impact on each of the three determination methods, error bars were exclusively added for the indirect determination of the surface coverage by remaining HS-ssO in the supernatant after *in situ* conjugation in Figure 2.

Quantification of ssO loaded on gold nanoparticles

Excess oligonucleotides were removed by centrifugation of nanoparticle suspensions for 30 min at 40,000g. The resulting supernatant was stored for further analysis. In the case of HS–ssO-Alexa 488 conjugation, the red precipitate was then washed twice with ddH$_2$O by successive centrifugation and redispersion and then finally taken up in 200 µL of an aqueous solution of 5 mM dithiothreitol (DTT). After 18 h at room temperature with intermitting shaking, the solutions containing the displaced HS–ssO-Alexa 488 were separated from the gold by a second centrifugation. Absorbance corresponding to excess ssO (260 nm) in the first supernatant (see Figure S6) and absorbance at 496 nm corresponding to displaced Alexa 488 labeled ssO (see Figure S7) in the second supernatant was recorded with a Shimadzu 1650 UV-VIS spectrometer. Intensities were converted to molar concentrations of HS-ssO-X by interpola-

tion from a linear standard calibration curve. Standard curves were prepared with known concentrations of HS-ssO-X (see Figure S5). Finally, the average number of HS-ssO-X per particle was obtained by dividing the measured HS-ssO-X molar concentration by the original nanoparticle concentration. Normalized surface coverage values were then calculated by dividing the estimated particle surface area (assuming spherical particles) in the nanoparticle suspension.
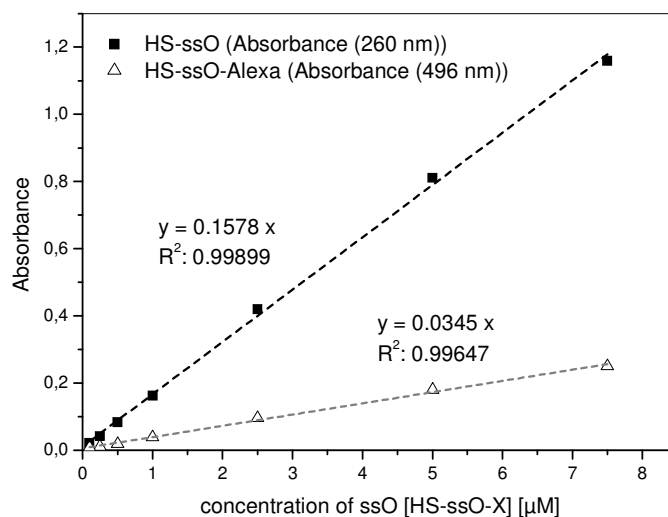
Figure S5.: Standard calibration line of the unlabeled oligonucleotide (HS-ssO) and the Alexa labeled oligonucleotide (HS-ssO-Alexa) at 260 and 496 nm respectively.
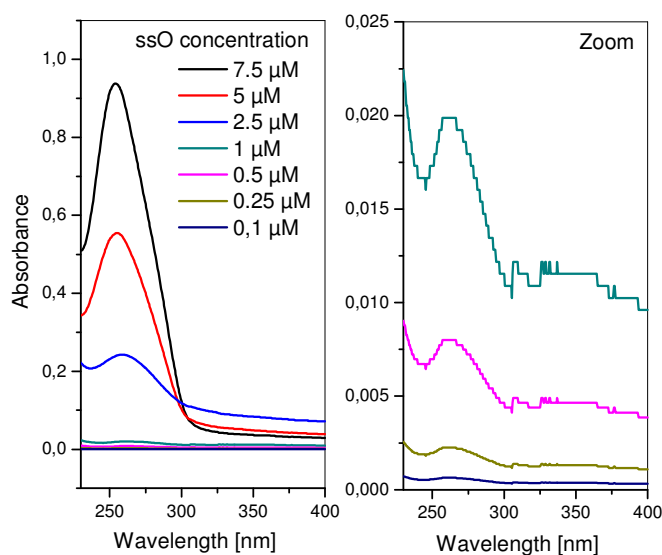
Figure S6.: UV spectra of remaining unlabeled ssO in the supernatant 1 after *in situ* conjugation at various HS-ssO concentrations.
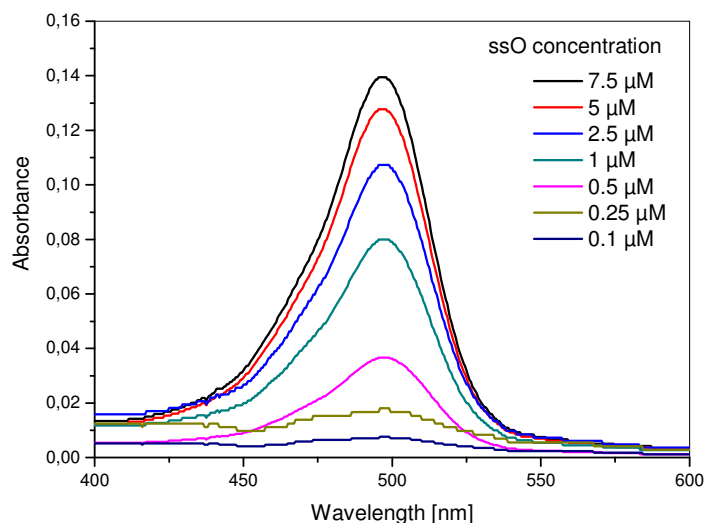
Figure S7.: Vis spectra of conjugated HS-ssO-Alexa in the supernatant 2 after ligand exchange with dithiothreitol and previous *in situ* conjugation at various HS-ssO-Alexa concentrations.

Quantification of recoverage or degradation of ssO after ligand exchange

25 µL of a 100 mM aqueous DTT solution were added to 475 µL colloid after conjugation with ssO. Following centrifugation after 18 h of co-incubation, absorbance at 496 and 648 nm was measured to estimate the concentration of displaced Alexa 488 and Cy5 respectively. Values after *ex situ* conjugation correspond to the recoverage after DTT displacement and after *in situ* conjugation to the sum of recoverage after DTT displacement and degradation due to laser irradiation.
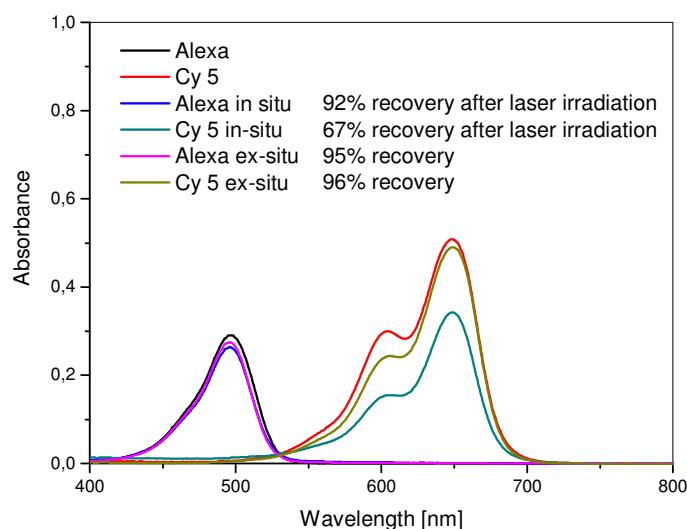
Figure S8.: Vis spectra of Alexa 488 and Cy5 labeled oligonucleotides before the conjugation process, after *ex situ* conjugation and *in situ* conjugation with 5 µM HS-ssO-X.

While recoverage of the fluorophores was checked by Vis spectroscopy (Figure S8), the analysis of oligonucleotides was performed by polyacrylamide gel electrophoresis. Quantification of DNA with its characteric absorbance band at 260 nm was not possible due to a coabsorbance of the ligand exchange agent dithiothreitol. For 20 % gels, 20 mL of an acrylamide/bis-acrylamide (37.5:1) solution was mixed with 14.4 g urea and 2.5 mL 10xTBE buffer. The mixture was heated above 37 °C to dissolve the urea. 7.5 ml water, 150 µL 10 % ammonium persulfate and 75 µL tetramethylethylendiamin were added. The mixture was swirled and then immediately poured in a gel tray (Maxi (20x20 cm) CTV400, VWR) and let to polymerize for 2 hours. To denature the oligonucleotides, 10 µL of formamide was added to 50 µL of each supernatant and the mixture was heated 2 min at 95 °C. 20 µL of a loading buffer containing 75 % glycerol, 0.125 % bromphenol blue and 0.125 % xylene cyanole was added. The references, containing the initial concentration of oligonucleotide, omitted the laser irradiation and were treated equally before gel electrophoresis and run with the samples on each gel. 10 µl of sample was loaded in each well. Gels were run 3 hours at 300 V in 1xTBE buffer (pH around 8.3 - 8.5). To visualize the bands on the gel after gel electrophoresis, gels were fixed in 30 % EtOH, 10 % glacial acid for 30 min. After thoroughly rinsing, the gels were stained and developed using Fast*Silver*[TM] (G Biosciences, USA). Scans of resulting stained gels were analyzed with Image J. The intensity of the bands I(x) was compared to the references I(0) in order to deduce the degree of recovered oligonucleotide after conjugation and/or laser ablation by equation 3.

Deg(x) = 1- I(x)/ I(0)   (Egn S1.)

Conjugation Efficiency during *ex situ* conjugation
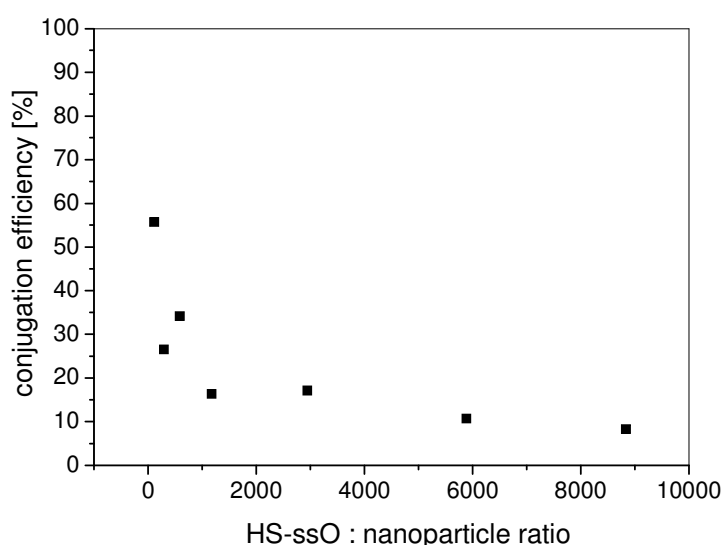
Figure S9.: Conjugation efficiency of the *ex situ* conjugation.

Bioconjugate size during ex situ conjugation

While the size quenching during *in situ* conjugation has been already discussed, after *ex situ* conjugation no difference was observed in the Feret diameter distribution of the gold nanoparticles. A look at the hydrodynamic size distribution revealed a slight increase of 2 nm due to the increased solvatisation shell of charged HS-ssO (Figure S10). The hydrodynamic size was determined by Dynamic Light Scattering with the Zetasizer ZS (Malvern). Three consecutive measurements are carried out and mean values are presented.
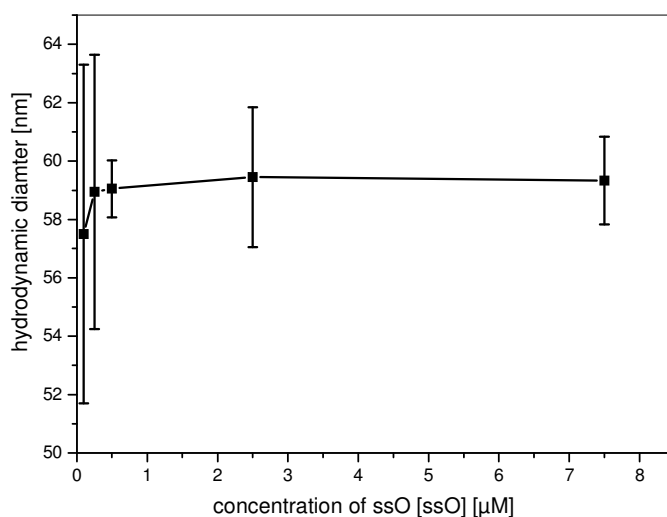
Figure S10.: Average hydrodynamic diameter of *ex-situ* conjugated gold nanoparticles with increasing ssO concentrations.

Comparison of surface coverage values by bioconjugation of laser-generated and chemically derived gold nanoparticles

Table S2.: Surface coverage values for chemically synthesized gold nanoparticles conjugated by ligand exchange reactions reported in literature.

Base length	Anchoring group	surface coverage [pmol cm^{-2}]	Ref
12	3' R-S-S-R	7.5	26
22	3' R-S-S-R	12.0	26
22	3' R-S-S-R	21.0	26
12	3'HS-R	12.6	26
22	3'HS-R	21.1	26
22	3'HS-R	12.2	26
12	5' HS-R	34	22
32	5' HS-R	15	22
32	3' HS-R	24	22
32	3' HS-R	35	22
23	5' HS-R	146	this paper

A.3. Laser ablation-based generation of bio-targeting gold nano-particles conjugated with aptamers.

Additional figures
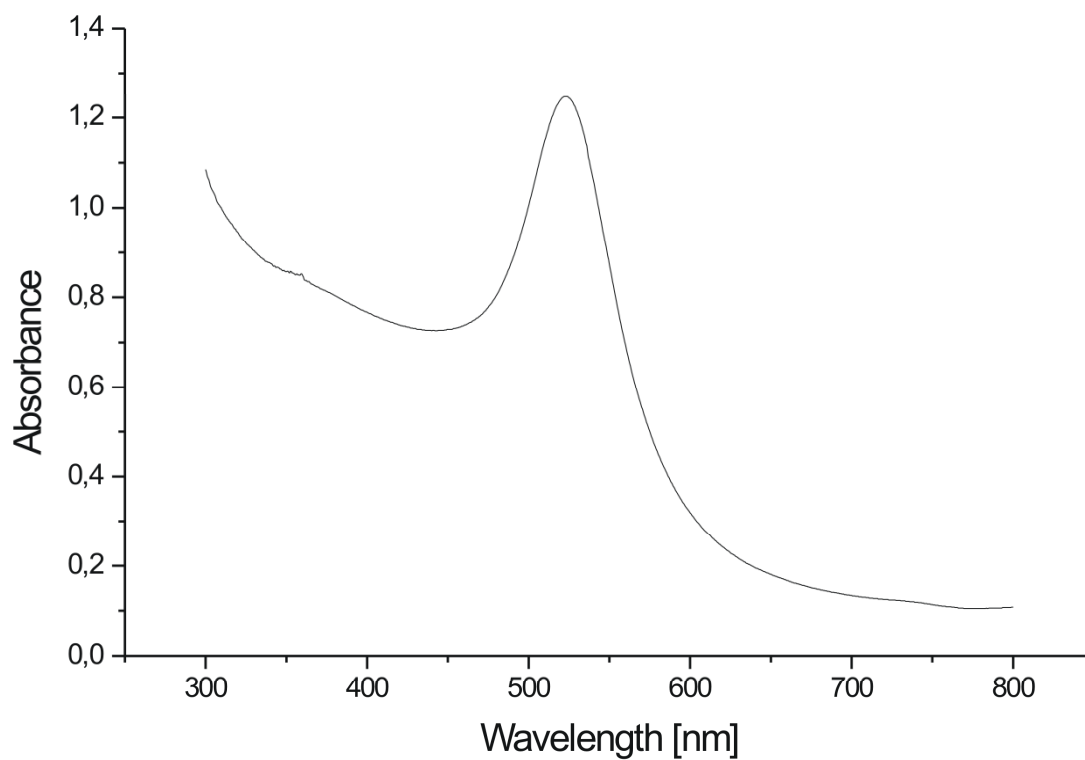
Figure S1.: UV-Vis spectrum of the as prepared AuNP solution after in situ conjugation with 5 µM anti streptavidin aptamer.
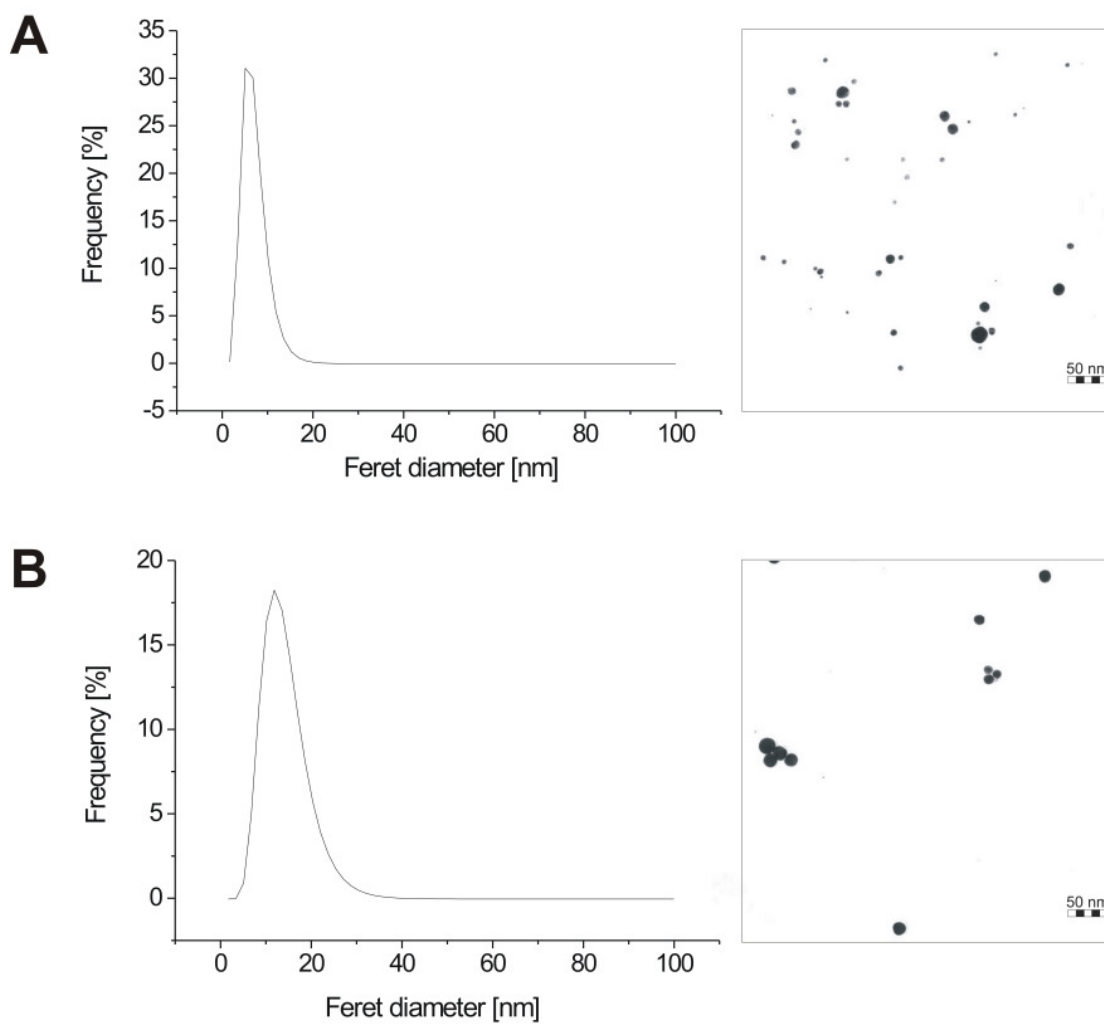
Figure S2.: TEM micrographs and AuNP size distributions (lognormal fit) of AuNPs produced by laser ablation in 5 µM miniStrep solution (A) before and (B) after removal of free aptamer by centrifugation.

A.4. Penetratin-conjugated gold nanoparticles – Design of cell penetrating nanomarkers by femtosecond laser ablation

Additional figures
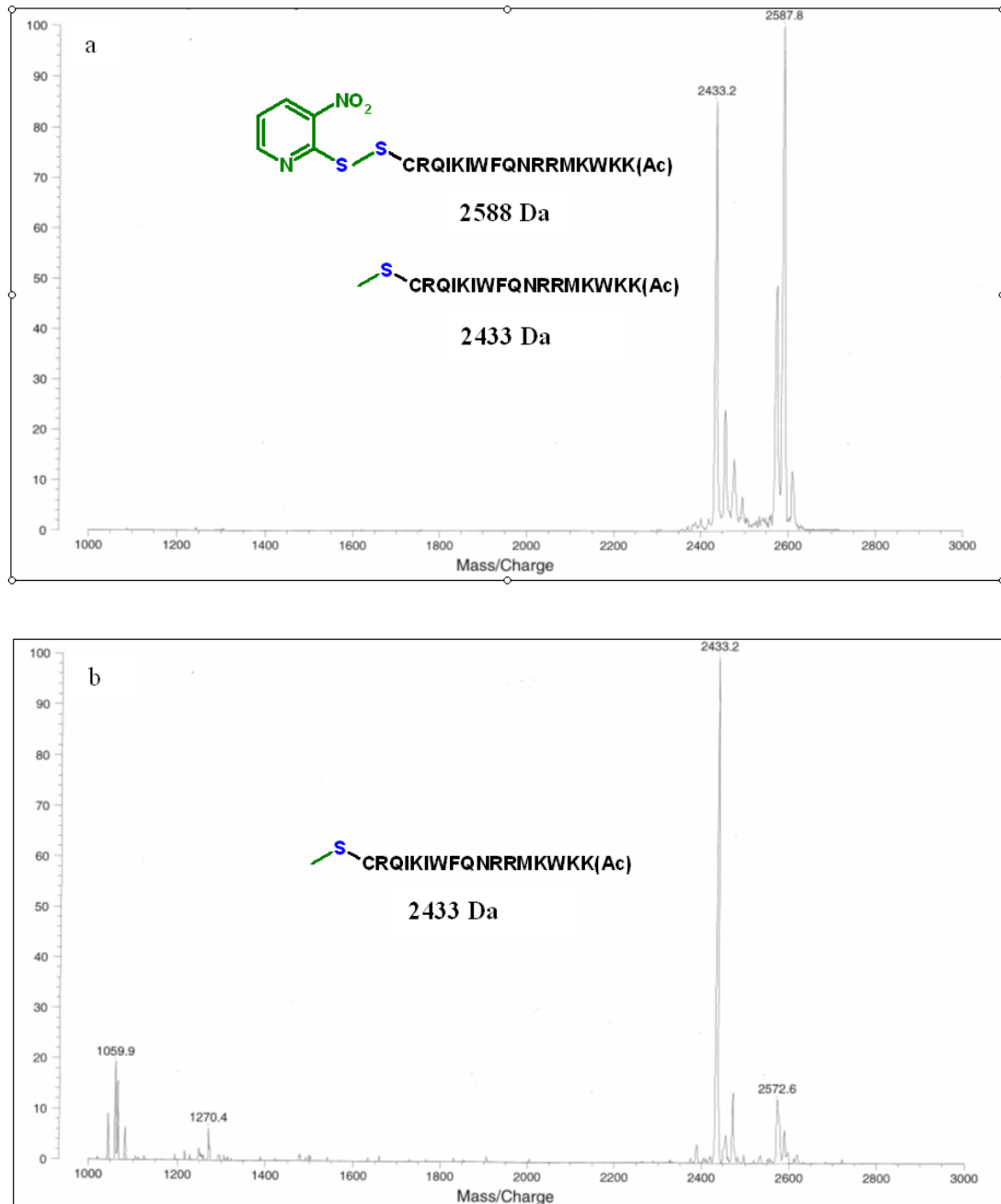
Figure S1.: Maldi-TOF spectra of penetratin after conjugation to AuNPs at (A) pH 6 and (B) pH 9.
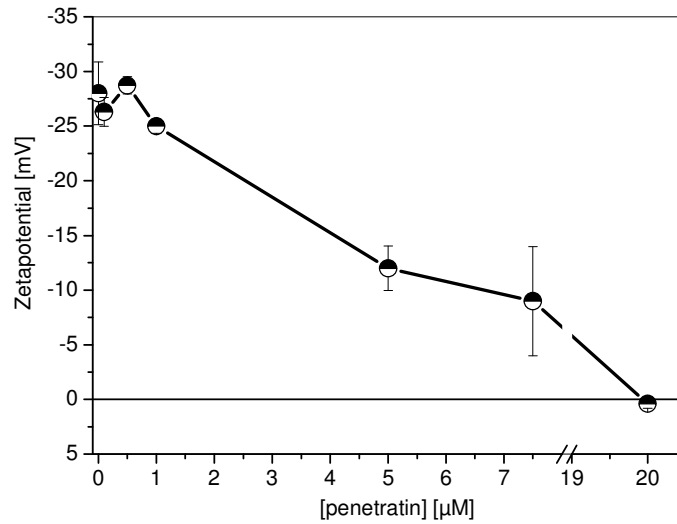
Figure S2.: Zetapotential of bioconjugates decreases in value with increasing penetratin concentrations in the ablation medium.
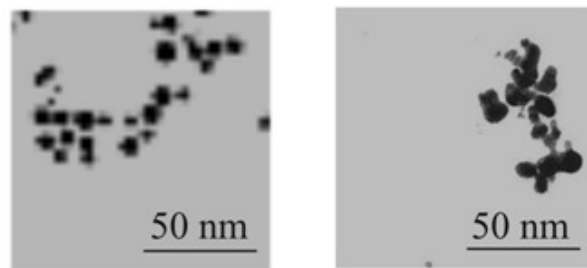
Figure S3.: TEM images of clusters generated in 5µM (left) and in 20 µM (right) penetratin. The interparticle spacing seems to decrease with higher peptide concentrations.
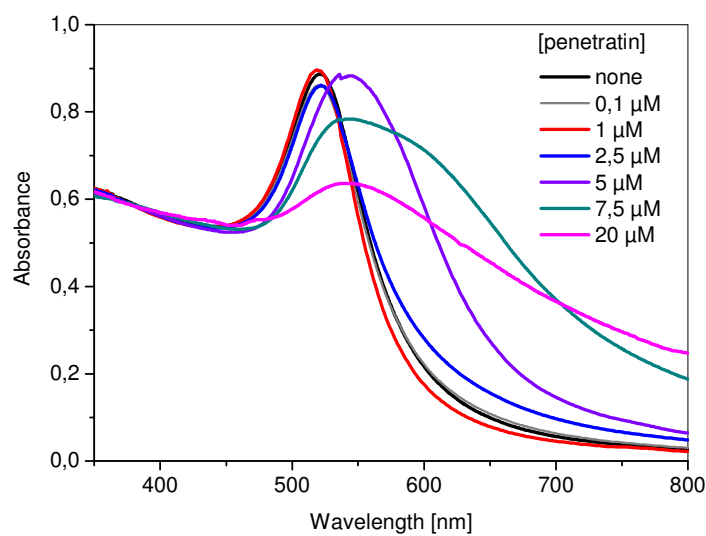
Figure S4.: UV-Vis spectra of ligand free and penetratin-conjugated AuNP generated by laser ablation in water and in solutions containing various amounts of penetratin at pH 9.

List of abbreviations

AuNP	gold nanoparticles
B_2H_6	diborane
BSA	bovine serum albumin
CPP	cell penetrating peptide
CRM	chemical reduction method
DDT	dodecanethiol
DLS	dynamic light scattering
DNA	deoxyribonucleic acid
DTT	dithiothreitol
eGFP	enhanced green fluorescent protein
fs LAL	femtosecond laser ablation in liquids
HMGB1	high-mobility-group-protein B1
LAL	laser ablation in liquids
LSCM	laser scanning confocal microscopy
Me	methyl
NA	nucleic acid
$NaBH_4$	sodium borohydride
NP	nanoparticle
PAMAM	poly(amido amine) dendrimer
PBAE	polyamino ester
PEG	polyethylene glycol
PEI	polyethylenimine
PPh_3	triphenylphosphine
PSMA	prostate specific membrane antigen
RSH	alkanethiol
SAM	self assembled monolayer
SDS	sodium dodecylsulfate
SEM	scanning electron microscopy
SH	thiol
siRNA	silencing ribonucleic acid
SPR	surface plasmon resonance
ssO	single stranded oligonucleotide
TEM	transmission electron microscopy

List of figures

(except figures included in papers)

List of tables

(except tables included in papers)

Curriculum vitae

PERSÖNLICHE DATEN

Name	Svea Petersen
Geburtsdatum	23.07.1981 in Lübeck

WISSENSCHAFTLICHE ARBEIT

seit Februar 2010	BMBF-Verbundprojekt „REMEDIS" Institut für Biomedizinische Technik Universität Rostock
Juli 2007 - Januar 2010	Junior Research Group „Nanoparticles" des DFG-Exzellenz Clusters REBIRTH Arbeitsgruppe Nanomaterialien Laser Zentrum Hannover e.V.
Juni 2005 – Juni 2007	Arbeitsgruppe „Chemistry and Patterning of Functional Surfaces" Abteilung Arzt Max Planck Institut für Metallforschung Stuttgart

AUSBILDUNG

2010	Vorlage der Dissertation „*In situ* bioconjugation of laser-generated gold nanoparticles for the rapid design of nanomarkers" Institut für Technische Chemie Gottfried Wilhelm Leibniz Universität Hannover
Juni 2007	Master of Science „Novel biosensors containing photosensitive cell adhesion RGD motifs on silica surfaces" Institut Bioorganique, Université Louis Pasteur Strasbourg
Oktober 2005 – Juni 2007	Masterstudium „Sciences Analytiques" Université Louis Pasteur Strasbourg
Juli 2005	Bachelor of Engineering „Feasibilty study concerning the use of recovered solvents for the washing of devices after production" Fachhochschule Reutlingen
Oktober 2002-Juli 2005	Bachelorstudium „Chemistry with Marketing" Fachhochschule Reutlingen

SCHULBILDUNG

1992 - 2001	Ostsee Gymnasium Timmendorfer Strand
1988 - 1992	Grund- und Hauptschule Pansdorf

Publications and conferences

Publications included in the thesis

(order as presented in the thesis)

[1] **S. Petersen**, J. T. Soller, S. Wagner, A. Richter, J. Bullerdiek, I. Nolte, S. Barcikowski, and H. Murua Escobar. Co-transfection of plasmid DNA and laser-generated gold nanoparticles does not disturb the bioactivity of GFP-HMGB fusion protein. *Journal of Nanobiotechnology*, 7:6, 2009.

[2] U. Taylor, S. Klein, **S. Petersen**, W. Kues, S. Barcikowski, and D. Rath. Nonendosomal cellular uptake of ligand-free, positively charged gold nanoparticles. *Cytometry Part A*, 77A:439-446, 2010.

[3] **S. Petersen** and S. Barcikowski. In-situ bioconjugation-Single Step Approach to tailored nanoparticle bioconjugates by ultrashort pulsed laser ablation. *Advanced Functional Materials*, 19:1167–1172, 2009.

[4] **S. Petersen** and S. Barcikowski. Conjugation Efficiency of laser-based bioconjugation of gold nanoparticles with nucleic acids. *Journal of Physical Chemistry*, 113:19830–19835, 2009.

[5] J.-G. Walter, **S. Petersen**, F. Stahl, T. Scheper, and S. Barcikowski. Laser ablation-based generation of bio-targeting gold nanoparticles conjugated with aptamers. Submitted to *Journal of Nanobiotechnology* 30.03.2010, ID 1661482437390205.

[6] **S. Petersen**, A. Barchanski, U. Taylor, S. Klein, D. Rath, and S. Barcikowski. Penetratin-conjugated gold nanoparticles - Design of cell penetrating nanomarkers by femtosecond laser ablation. Submitted to *Bioconjugate Chemistry* 27.02.2010, ID bc-2010-00104h.

[7] L. Sajti, **S. Petersen**, A. Menendez-Manjon, and S. Barcikowski. In situ bioconjugation in stationary liquid and in liquid flow. Submitted to *Applied Physics A* 14.11.2009, revised 22.03.2010, ID 168 COLA/APA.

Publications not included in the thesis

(reversed chronological order)

[1]   S. Klein, **S. Petersen**, U. Taylor, D. Rath, and S. Barcikowski. Quantitative visualization of colloidal and intracellular gold nanoparticles by confocal microscopy. Accepted for publication in *Journal of Biomedical Optics* 15.04.2010, ID 09563.

[2]   J. Jakobi, **S. Petersen**, A. Menéndez-Manjón, P. Wagener, and S. Barcikowski. Magnetic alloy nanoparticles form laser ablation in cyclopentanone and their embedding into a photoresist. *Langmuir*, doi: 10.1021/la101014g, 2010.

[3]   A. Schnoor, **S. Petersen,** and S. Barcikowski. Laserfragmentierung von anorganischen und organischen Mikropartikel-Suspensionen zu Nanopartikel-Kolloiden. *Chemie Ingenieur Technik*, 82:317-326, 2010.

[4]   **S. Petersen**, J. Jakobi, and S. Barcikowski. In situ bioconjugation—Novel laser based approach to pure nanoparticleconjugates. *Applied Surface Science*, 255:5435–5438, 2009.

[5]   **S. Petersen**, J. Jakobi, A. Hörtinger, and S. Barcikowski. In-Situ Conjugation - Tailored Nanoparticle conjugates by Laser Ablation in Liquids. *Journal of Laser Micro/Nanoengineering*, 4:71–74, 2009.

Conferences

(reversed chronological order)

[1]   S. Klein, **S. Petersen**, U. Taylor, D. Rath, and S. Barcikowski. Quantification of colloidal and intracellular gold nanomarkers down to the single particle level using confocal microscopy. Photonics West: Biomedical Optics, San Francisco, USA, 23.01.2010, SPIE Proceedings **7573**, 75730L, 2010.

[2]   **S. Petersen** and S. Barcikowski. Optimizing parameters for the in-situ bioconjugation of laser generated gold nanoparticles. International Congress on Laser Advanced Material Processing, Kobe, Japan, 29.06-02.07.2009.

[3]   **S. Petersen** and S. Barcikowski. Nanoparticle bioconjugates by laser ablation - a novel method aiming at pure drug and gene delivery. VDI-conference "7th International Nanotechnology Symposium - New Ideas for Industry", Dresden, Germany, 26.-27.05.2009.

[4]   **S. Petersen** and S. Barcikowski. Nanoparticle bioconjugates by laser ablation - a novel method aiming at pure drug and gene delivery. 10th International Conference on Biomedical Applications of Nanotechnology, Berlin, Germany, 04.-06.03.2009.

[5]   **S. Petersen**, J. Jakobi, and S. Barcikowski. In-Situ Bioconjugation - Tailored Nanoparticle Bioconjugates by Laser Ablation in Bioactive Media. 9th International Symposium on Laser Precision Microfabrication, Quebec, Canada, 16.-20.06.2008.

[6]   **S. Petersen**, J. Jakobi, and S. Barcikowski. In-situ bioconjugation of nanoparticles - Novel laser based approach to pure nanoparticle conjugates. EMRS Spring Meeting, Strasbourg, France, 26.-30.05.2008.

[7]   **S. Petersen**, A. Hahn, and S. Barcikowski. Design of bioactive nanomaterials with ultrapure nanoparticles generated by femtosecond laser ablation in solution. Nanotransfer, Paris, France, 2007, 03.-04.12.2007, Proceedings 6-11.

[8]   S. Barcikowski, J. Jakobi, **S. Petersen**, A. Hahn, N. Bärsch, and B. Chichkov. Adding functionality to metal nanoparticles during femtosecond laser ablation in liquids. 24th International Conference on Applications of Lasers and Electro-Optics ICALEO, Orlando, USA, 29.10.-01.11.2007, Proceedings 108-113.

[9]   **S. Petersen**, J. Jakobi, and S. Barcikowski. Coating of metal nanoparticles using in-situ functionalization during femtosecond laser ablation in solution - a novel method aiming at ultra-pure drug and gene delivery. Jahrestagung Deutsche Gemeinschaft für Biomaterialien, Hannover, Germany, 22.-24.11.2007, Biomaterialien 8: 155-156.

Erklärung

Diese Arbeit wurde am Laser Zentrum Hannover e.V. in der Zeit von Juli 2007 bis Januar 2010 in der Arbeitsgruppe Nanomaterialien von Herrn Dr. Stephan Barcikowski durchgeführt. Die Verfasserin versichert, die vorliegende Arbeit eigenständig durchgeführt und alle verwendeten Hilfsmittel angegeben zu haben. Fremde Gedanken sind als solche kenntlich gemacht worden.